Linear and Nonlinear Optical Characterisation of Self Assembled Nanostructures

Lina Persechini

School of Physics

Trinity College Dublin, Ireland

A thesis submitted for the degree of

Philosophiæ Doctor (PhD)

October 2012

Declaration

This thesis has been submitted to the University of Dublin for examination for the degree of Doctor in Philosophy by the undersigned.
This thesis has not been submitted as an exercise for a degree to any other university.
With the exception of the assistance noted in the acknowledgments, this thesis is entirely my own work.
I agree that the Library of the University of Dublin may lend or copy this thesis upon request.

Lina Persechini October 2012
School of Physics,
University of Dublin,
Trinity College,
Dublin

Abstract

The use of optical techniques for material characterisation offer several advantages: it is non–destructive, useful in all pressure ranges, and a wide range of material systems can be probed. However, it is not always possible to isolate the surface or interface contribution. Epioptics refers to a special branch of optics devoted to the measurement of the surface and interface responses. Reflection anisotropy spectroscopy (RAS) and Second–harmonic generation (SHG) studies were carried out on various self–assembled systems including: self–assembled plasmonic nanostructures and ultra–thin chiral films. These very different systems will show how useful these techniques are for material growth and charcterisation.

RAS is very useful to grow and tune plasmonic nanostructures for a wide range of applications. SHG is a nonlinear technique which is sensitive to localised surface plasmon resonances (LSPRs), and consequently weak nonlinear signals are amplified. SHG was used to charcterise silver on rippled silicon templates, where interesting information can be extracted on the symmetry and morphology of the nanoparticle (NP) layer.

Modelling these plasmonic resonances is often challenging and complex especially when dealing with arbitrary shapes. The linear optical response of these structures was modelled with a view to enable the responses of any plasmonic structure using any template to be predicted.

Chiral molecules are by nature asymmetric. SHG is highly symmetry dependent, and so was used to detect ultra–thin films of a chiral molecule (cysteine) in UHV conditions.

Contents

List of publications

Persechini, L. & McGilp, J. F. Chiral second-harmonic generation from small organic molecules at surfaces. *Physica status solidi (b)*, 2012.

Persechini, L. and Ranjan, M. and Grossmann, F. and Facsko, S. and McGilp, J. F. The linear and nonlinear optical response of native-oxide covered rippled Si templates with nanoscale periodicity. *Physica status solidi (b)*, 2012.

List of Figures

List of Tables

List of abbreviations

AES	Auger electron spectroscopy
AFM	Atomic force microscopy
aSi	Amorphous silicon
BBO	Beta barium borate
CD	Circular dichroism
Binol	1,1'–binaphthalene–2,2'– diol
D	Dextrorotatory
IR	Infrared
L	Levorotatory
LDA	Local density approximation
LEED	Low energy electron diffraction
LN	Liquid nitrogen
LPR	Localised surface plasmon resonance
ML	Monolayer
MOKE	Magentic optical Kerr effect
NP	Nanoparticle
PEM	Photo-elastic modulator
PMT	Photo muliplier tube
RAS	Reflection anisotropy spectroscopy
RFA	Retarding field analyser
SE	Spectroscopic ellipsometry

SEM	Scanning electron microscopy
SHG	Second harmonic generation
SP	Surface plasmon
STM	Scanning tunneling microscopy
UHV	Ultra high vacuum
UV	Ultraviolet

Chapter 1

Introduction

> "Begin at the beginning," the King said, gravely, "and go on till you come to the end; then stop."
>
> –*Lewis Carroll, Alice in Wonderland*

This chapter introduces the field of epioptics, which is a specialised area of optical techniques devoted to surface and interface characterisation. The material systems studied in this thesis, including plasmonic structures and thin film chiral systems, will be introduced. An overview of the literature is also provided, highlighting the advantage of using epioptic techniques to characterise these systems.

1.1 Surface and interface optics

When optical radiation is used to probe a material, it has the ability to penetrate past the surface into the bulk material, making discrimination between bulk and

surface contribution difficult. However, the surface or interface structure differs significantly from that of the bulk. The optical techniques have been developed which exploit these differences, and measure the optical response of the surface or interface with sub–ML resolution. Figure 1.1 compares sampling depths for electrons to those of photon–based techniques. For metals optical radiation penetrates ∼10 nm, which allows buried interfaces to be probed. Since the first optics experiment by Chiarotti *et al* in 1968 [1], which identified the presence of surface states on the cleaved (111) surface of Ge, many more experimental techniques have been developed [2] in order to understand condensed matter surfaces and interfaces. In particular, the exploitation of symmetry differences between the bulk and the surface has led to the development of a unique area of optics for surface and interface characterisation termed "epioptics" (from the Greek "epi" meaning upon) [3].

In general, optical techniques offer significant advantages over traditional electron based techniques. Optical techniques are non–invasive and non–destructive, all pressure ranges are accessible allowing *in situ* monitoring of monolayer growth. The characterisation of a wide range of material systems (such as liquid–solid, liquid–liquid and solid–solid interfaces) is possible due to the penetration depth of the radiation.

The interaction of an electromagnetic (EM) field of frequency ω with matter induces a polarisation which can be described as an expansion.

$$P(\omega, 2\omega) = \epsilon_0[\chi^{(1)}(\omega)E(\omega) + \chi^{(2)}(\omega, 2\omega)E^2(\omega) + ...] \tag{1.1}$$

where $\chi^{(i)}$ is the ith–order susceptibility tensor of rank $i + 1$ describing the ma-

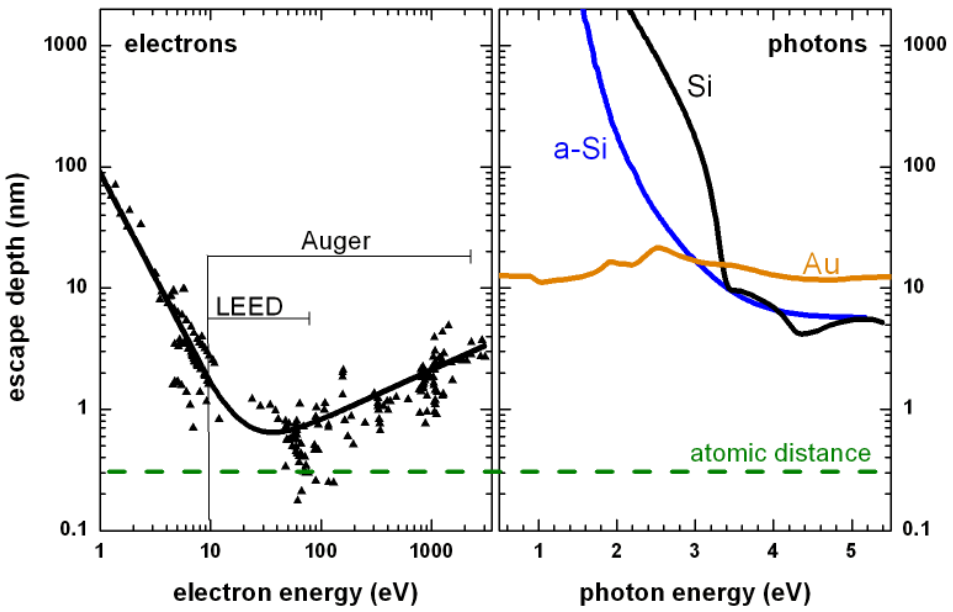

Figure 1.1: A comparison of escape depth between optical and electron based techniques

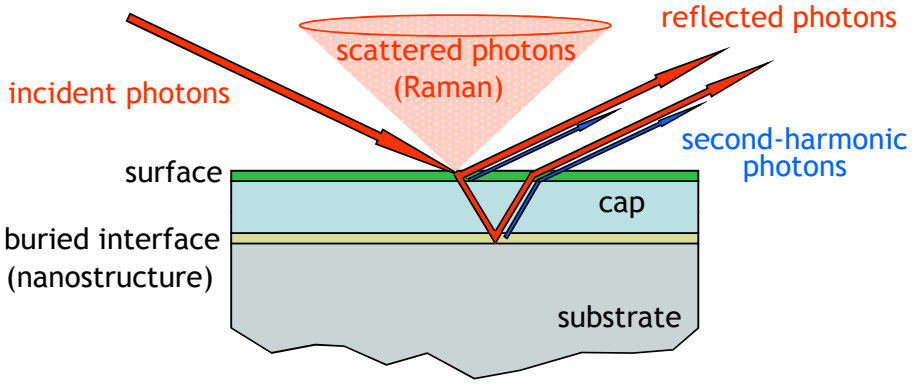

Figure 1.2: The field of epioptics covers a range of different techniques including RAS, Ramen and SHG, see [2] for details.

terial response. The first term on the right–hand side of Equation 1.1 describes the linear optical response, which is exploited in techniques such as spectroscopic ellipsometry (SE) and reflection anisotropy spectroscopy (RAS). In linear optics the dielectric tensor, $\epsilon(\omega)$, is related to the linear susceptibility by $\epsilon(\omega) = 1 + \chi^{(1)}(\omega)$. However, the nonlinear term in Equation 1.1, which depends on $\chi^{(2)}(\omega, 2\omega)$, becomes significant at high EM field strengths and has a polarisation quadratic in the EM field. $\chi^{(2)}(\omega)$ describes the lowest–order nonlinear optical response responsible for second–harmonic generation (SHG). Higher order terms are also possible within the electric dipole approximation: in the absence of any resonantly enhanced surface electric dipole effects, the third–order response $\chi^{(2)}(\omega, 2\omega, 3\omega)$ probes the bulk, while fourth–order terms are surface sensitive but require compressed pulses of high peak power in order to observe them. Symmetry arguements have been used to show that the rank of the tensor and the order of the multipole expansion of the EM field determine the degree of the surface and interface rotational anisotropy that can be probed [4]. Within the electric dipole approximation, an nth rank tensor can exhibit up to n–fold rotational anisotropies. Therefore experimental techniques based on different rank tensors will provide complementary information. RAS, for example, can detect two–fold in plane rotational anisotropy, while SHG can detect up to three–fold anisotropy and in principle fourth–harmonic generation (FHG) can detect up to five–fold anisotropy [5]. The generation of the types of pulses required for FHG is becoming more straightforward, so it is likely that quasicrystal surfaces (5–fold rotation) will be probed using FHG in the future.

A surface or interface may possess in–plane rotational anisotropy, while the bulk may be isotropic. Linear epioptic techniques will be sensitive to two–fold

anisotropy, however, the presence of surface domains rotated with respect to each other may restore the overall symmetry of the bulk. It has been found that domain formation can be suppressed by using vicinal substrates. With suitable heat treatments a single domain ordered step and terrace structure can be obtained. The surface has a single mirror plane of symmetry which runs perpendicular to the steps, while the terrace retains its two–fold or higher axis of rotation. These vicinal surfaces may also be used as templates for the growth of aligned nanostructures by self–assembly or glancing angle deposition (GLAD) [6]. Epioptic techniques are particularly useful for the *in situ* characterisation of the growth of aligned nanostructures on vicinal surfaces, and probing buried interfaces and aligned structures which are capped to prevent corrosion and contamination [7]. Epioptic techniques are becoming increasingly important in the area of advanced materials fabrication.

1.1.1 Reflection anisotropy spectroscopy

RAS, is a surface sensitive probe which measures the difference in reflectivity of light polarised at orthogonal angles on the sample surface near normal incidence, thus measuring in–plane optical anisotropy. RAS was first described by Aspnes [8] and Berkovits [9], and a detailed review of this technique has been published by Weightman *et al* [10]. In cubic systems where the bulk is isotropic, the surface reconstructs to break symmetry and a RAS signal can only arise from anisotropy in the surface (see Section 2.1.1 and 3.3 for more details). RAS was first used for the study of III–V semiconductors [9, 11], due to its ability to characterise material systems in all pressure ranges. The technique has been used for

the characterisation of a wide range of semiconductor [12–14] and metal [15–18] systems successfully and, more recently, for the study of aligned nanostructures on vicinal surfaces [19, 20]. In material systems that are subject to damage or contamination by the ambient, it is useful to deposit a capping layer, the effect of which can be studied due to the sensitivity of RAS to interface structure [21]. RAS has been useful as a qualitative technique for *in situ* monitoring during the growth of nanostructures in real time. Of particular interest in the rapidly growing area of plasmonics is the ability of RAS to monitor the growth of plasmonic, self assembled island arrays [22].

1.1.2 Second–harmonic generation

Second–harmonic generation (SHG), is a nonlinear optical technique which, due to symmetry considerations, is sensitive to surface and interface structure. The process is an example of three–wave mixing, where two incident photons interact with the material to create a photon at the sum or difference of the frequencies of the input photons (see Section 2.2.1 and 3.4). After the advent of the laser, SHG was first observed by Franken and co–workers in 1961 [23]. One of the first *in situ* studies by Tom *et al* [24] showed how different adsorbates on Rh(111) can reduce and enhance the second–harmonic (SH) signal, demonstrating its surface sensitivity. Later, Heinz and co–workers [25–27] investigated the dependence of the SH signal on surface symmetry by studying the (2×1) and (7×7) reconstructions of Si(111). The work of McGilp and Yeh [28] showed that SHG can provide information even on the buried metal–semiconductor interface, using the Si(111)–Au system as an example. Since then a wide range of material systems including

semiconductor, metallic surfaces [29, 30] and metal on semiconductor interfaces [31–33] have been studied successfully. SHG from semiconductor interfaces has been reviewed recently by Luepke [34].

The development of femtosecond laser systems made the use of nonlinear optics to study ultra–thin magnetic film feasible. Magnetic second–harmonic generation (MSHG) has been reviewed recently by Kirilyuk and Rasing [35], contributions from various magnetic regions of sub–ML nanostructures, due to magnetic terrace or edge atoms on vicinal surfaces, have been identified and hysteresis loops are extracted using this technique [36, 37]. Other developments in this field include electric–field–induced SHG or EFISH, which has been used to study defects or traps at the dielectric/Si interface of gate dielectrics in advanced CMOS devices [38, 39].

Observation of surface optical effects from plasmonic structures can be dated back to the work of Wokaun *et al* [40], where surface–enhanced SHG was observed in silver island films. Since then, very little work has been published on the use of SHG as a characterisation technique for plasmonic material systems.

The investigation of chiral films using SHG has also attracted interest, as chiral molecules do not possess inversion symmetry. Linear circular dichroism (CD) does not have sufficient sensitivity to probe chiral films of only a few MLs thickness adsorbed on surfaces,and cannot be used in a reflection geometry. Monolayers of larger molecules, with a significant chiral nonlienar response, have been shown to generate a measurable SH response in reflection, when adsorbed on centrosymmetric substrates [41, 42].

1.2 Plasmonic nanostructures

It has been shown by Mie in 1908 [43], that when light interacts with a metal particle, collective ocillations of the free electrons known as plasmons are produced (see Figure 1.3). The oscillating EM field induces a shift in the electrons, causing charges to accumulate on opposite surfaces of the nanoparticle, hence polarising it. The area of research involved in exploring the applications of this response is known as plasmonics. This type of plasmon is often referred to as a localised surface plasmon polariton (LSP), to distinguish it from the surface plasmon of extended flat metal surfaces. This interaction results in interesting optical absorption features associated with LSP resonances (LSPR), which depend on size and shape of the metallic structures [44], as well as an enhancement of the local electromagnetic field. For nanoparticles (NPs) of the metals, with dimensions between 2 nm and 200 nm these absorptions are typically found in the visible range (Ag [45, 46], Au [47] and Cu [48]), other metals like Pb and Al exhibit resonances in the IR and deep UV [49, 50] respectively. These subwavelength structures are attracting attention because of their potential as optical sensors, in waveguiding [51], biosensors [52], and even solar cells [53, 54].

1.2.1 Overview of the literature

The area of plasmonics is being intensively researched at present, and a number of recent reviews have been published [55–57]. The field has progressed through the advances of NP preparation by colloidal synthesis. The process involves the reduction of an acidic solution: as more atoms are formed the solution becomes supersaturated, and precipitation of the noble atoms to form sub–nm particles

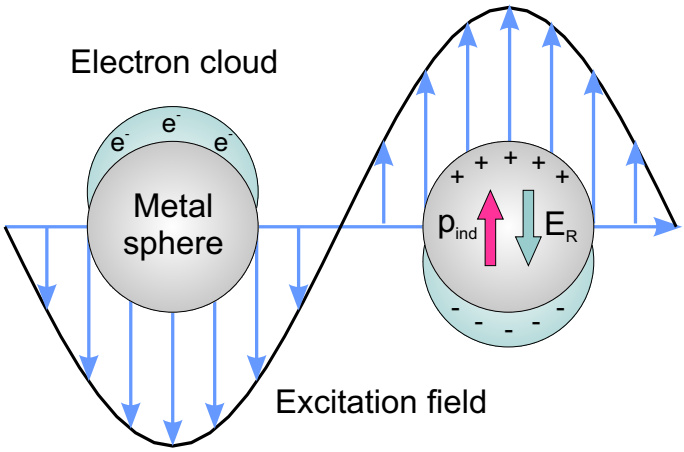

Figure 1.3: The response of a homogeneous metallic sphere placed in an oscillating EM field. The conduction electrons are displaced, polarising the sphere (p_{ind})

.

follows. these act as nucleation centres for the growth of the NPs [58]. Although successful, this cannot produce the ordered arrays of NPs on surfaces required for some of the applications. Nanoscale templates produced by non–lithographic processes can provide a stable surface upon which to grow NPs of various sizes, by self–assembly. This appears to be a promising approach, as the fabrication of templates by electron beam lithography, followed by deposition of the metal, is a specialised and time–consuming process.

The positions of the localised surface plasmon resonances (LSPR) are of critical importance for many applications. This has been shown to depend on the dielectric function of the nanoparticle (NP), its size and shape, the inter–particle separation and the dielectric function of the surrounding medium [44].

Analytic theories of the LSPR lineshapes for NPs within a surrounding medium, either immersed in a liquid or embedded in a solid matix have been developed [44] successfully. However, for NPs of arbitrary shape in a complex dielectric

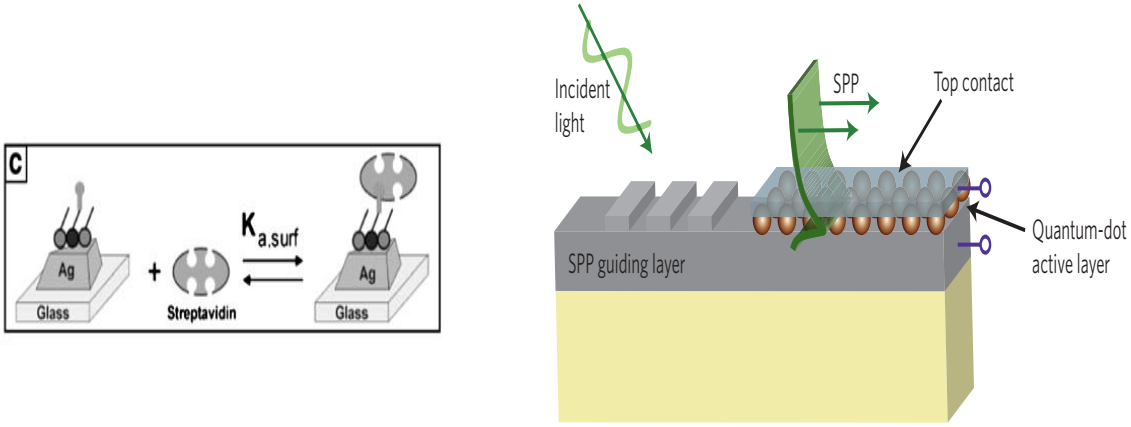

(a) A nanoscale biosensor based on LSPR sensitivity to local medium dielectric changes. The diagram shows the binding of strepvidin molecules to the biotinylated nanotriangles on the substrate, after [52]

(b) NPs can be incorporated in solar cells, acting as scatterers, they increase the optical path of light inside the absorbing material, thus increasing the overall efficiency of the solar cell. The image is a plasmonic quantum–dot solar cell designed for enhanced photoabsorption, after [53].

Figure 1.4: The various applications of plasmonic structures are being heavily researched. Biosensors and solar cells some of the many applications.

environment, analytic solutions are not available and Maxwell's equations are solved directly using techniques such as the discrete dople approximation and finite difference time domain methods [60]. Analytic theories of NPs supported on planar surfaces have been developed, but only for spheroids and ellipsoids where the NPs are axially symmetric with respect to the surface normal [61]. Numerical approaches have been used for isolated NPs and NP arrays with dimensions accesible by conventional lithographic techniques [62], but smaller less ordered

Figure 1.5: Colloidal solutions of Ag, Au and Ag-Au bimetallic nanoparticles (after [58]). The colloidal solutions are strongly coloured because of the LSPR in the UV/visible spectral region.

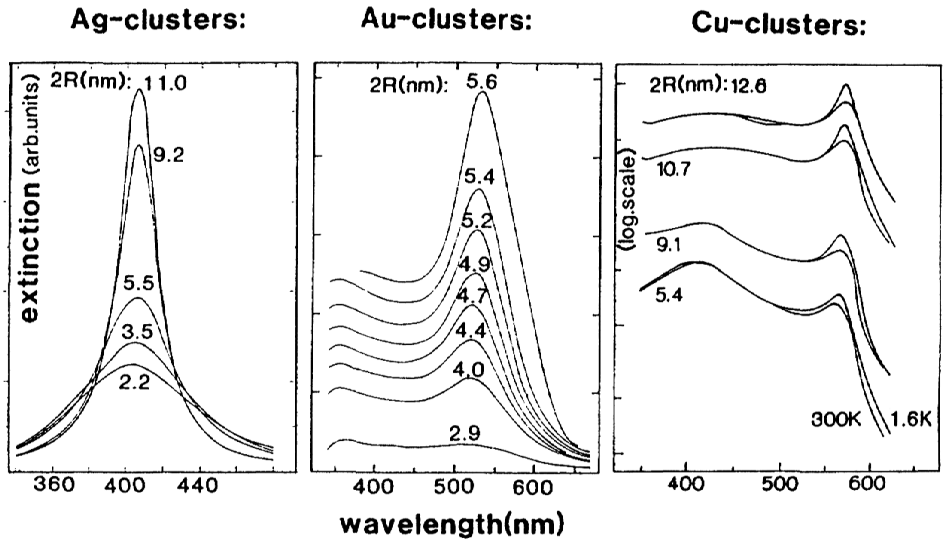

Figure 1.6: Measured extinction spectra of Ag, Cu and Au clusters of various sizes in a glass matrix, after [59]

structures are currently too computationally intensive for this approach to be useful. An apporximate analytic theory of the optical response of these systems

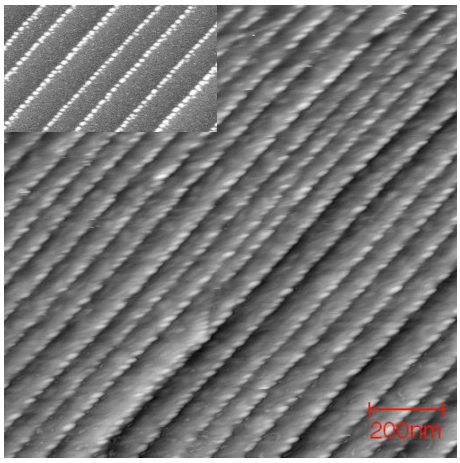

(a) AFM image of faceted Al_2O_3 substrate. Inset: SEM image of Ag NPs grown at glancing angle of 6° on the faceted template.

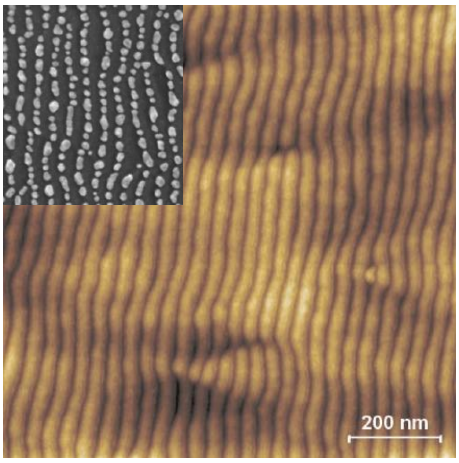

(b) AFM of a native–oxide–covered rippled Si(001) surface with ∼30 nm periodicity. Inset: SEM of Ag NPs deposited on the rippled surface.

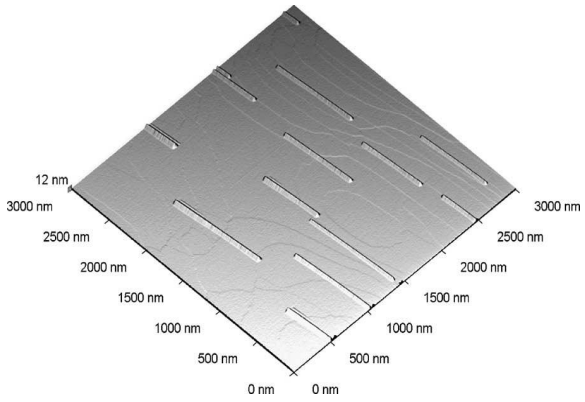

(c) 3μm×3μm STM topographic image of the Si(335) substrate with Pb nanowires, after [63].

Figure 1.7: Examples of nanoscale templates: faceted Al_2O_3, Si(001) and Si(335) for the production of aligned nanoscale arrays.

is developed in Chapter 4.

Recent experimental approaches aim to produce aligned nanoscale arrays in

a controllable and reproducible fashion. For example, the annealing procedure for vicinal single crystal Al_2O_3 substrates can be adjusted to control nanoscale terrace width and periodicity associated with facetting (Figure 1.7a) [22, 64, 65]. Similarly, Pb deposited on vicinal Si(111) forms aligned, elongated islands with length to width ratios greater than 100 (Figure 1.7c) [63]. Low energy ion beam irradiation is another established method for forming nanoscale periodic patterns on flat substrates [66, 67]. Using these rippled templates NP arrays with short range order and adjustable periodicity can be made on various substrates, including native-oxide-covered Si(001) (Figure 1.7b) [68, 69]. Local damage and disorder is caused by irradiation of the surface, but it has been shown recently that the quality of these rippled structures can be improved significantly by sequential sputtering at lower fluences, with the sample rotated 90° so that the ion beam is aligned along the ripples at grazing incidence [70].

1.2.1.1 Optical techniques

Although absorption spectroscopy is routinely used to characterise the plasmonic, epioptic techniques remain largely unexplored for growth monitoring and characterisation of plasmonic nanostructures. The in–plane LSPRs of anisotropic Nps are accessible to RAS, while the out–of–plane LSPR requires SE. Historically, the RAS response of plasmonic nanostructures was seldom reported, due to limitations in colloidal preparation techniques in the past. It was Witkowski *et al* who first used RAS to study self-organised, anisotropic cobalt nanodots on vicinal Au(111) [71], demonstrating that with improved methods of sample fabrication, the plasmonic response can be monitored directly. Recent studies have shown that isotropic Ag NPs grown on an anisotropic sustrate also produce a

measurable RAS response [72]. Chapter 5 describes the use of RAS and SE to characterise LSP systems.

Real–time monitoring of the growth of these anisotropic rippled templates, during Ar^+ ion irradiation, which is used at pressures typically in the range of 10^{-4} mbar, is challenging. Epioptic techniques offer significant advantages over conventional surface techniques in characterising the formation of these surface structures, as they are insensitive to charged particles and surface potentials. Our group, in collaboration with colleagues, have shown recently that RAS is a useful *in situ* probe of Ag NP growth on facetted Al_2O_3 [22], raising the possibility that such optical techniques may be able to monitor the growth of both the template and the NP array, in real time.

Upon excitation LSP excitation produces a very strong amplification of the electric field, which is dependent on size, shape and environment of the NP. This has led to the development of LSP–enhanced spectroscopy , for example Surface Enhanced Raman Scattering (SERS) [73]. This technique developed originally using rough Ag surfaces, but the use of LSPRs, particularly localised at the tip of a scanning probe system, has led to Raman spectra from single molecules being detected at surfaces [3]. Similarly, this field enhancement can also be used to amplify the weak signals from nonlinear optical techniques like SHG. SHG from metal surfaces has been widely studied both theoretically and experimentally [74–76], since their response is much stronger due to loosely bound electrons which are more polarisable. However, SHG from self–organised metallic NPs is seldom reported. SHG is a potential optical technique for monitoring the growth of these plasmonic structures in real time, particularly when working at the plasmon resonance, where the signal is amplified substantially. Belardini *et al* [77], have

conducted spectroscopic SHG on Au nano–wire arrays on ion beam irradiated glass at normal incidence, in order to tune the metal plasmon resonance close to the pump frequency, and also investigated the effect of local tilt of the nanowires. The conversion efficiency was found to increase as the plasmon resonance was shifted closer to the pump wavelength, and highly dependent on the tilt and hence shape of the nanowire in cross-section, indicating the sensitivity of this technique. Furthermore Kim *et al* have studied third harmonic generation (THG) in silver island films [78]. SHG is useful even when spectroscopic studies may not be possible. Polarisation dependent studies of these structures can provide in– and out–of plane information on symmetry of the NP, as dicussed in detail in Chapter 5.

1.3 Thin film chiral systems

A chiral molecule is defined as one which has a non-superimposable mirror image. The term chirality comes from the Greek word *kheir*, meaning handedness, and was coined by the Irish physicist William Thomson (Lord Kelvin) in his 1884 Baltimore lectures. Perhaps the most universally recognised image of chirality is a pair of hands: the left hand cannot be superimposed on the right one (Figure 1.8). Simple chiral molecules exist in two enantiomeric forms, which differ in their interaction with other chiral systems, but otherwise have the same physical and chemical behaviour. Most of the molecules which are important to living systems are chiral, e.g. amino acids, proteins, sugars and nucleic acids. Chiral drugs have become a dominant feature in today's pharmaceutical industry, with single enantiomer drug production increasing dramatically. It is estimated that

80% of todays developmental drugs are now chirally pure [79], and improvements in chiral synthesis, purification and characterisation are being sought.

1.3.1 Overview of the literature

The invention of scanning tunneling microscopy (STM) has opened up ways to study interactions on a molecular level at well–characterised surfaces. Further advancements in the field have led to probing chiral phenomena, e.g. adsorption and reaction on crystalline surfaces, where absolute chiral recognition can be attained [80]. For example, chirality and conformation of terephthalic acid monolayers on graphite [81] has been studied, while Fang *et al* [82] have used Br atoms as an STM marker on the stereogenic centre to determine the chirality of 2-bromohexadecanoic acid adsorbed on a graphite surface. Chiral discrimination by chemical force microscopy has also been successful [83]: by attaching chiral molecules to the probe tip, the two enantiomers of mandelic acid (2-hydroxy-2-phenylacetic acid) were differenciated through differences in adhesion and frictional forces measured by the probe. The most relavent example, however, for this thesis, is the adsorption of cysteine on Au(110) surfaces in UHV [84, 85]. Figure shows chiral recognition in the dimerisation of adsorbed cysteine observed by STM (Figure 1.9) [84]. Such STM studies have provided important new information but, in general, alternative methods of detection of chirality at surfaces are needed in order to perform these experiments under realistic synthesis conditions, and this is not possible with conventional surface science techniques.

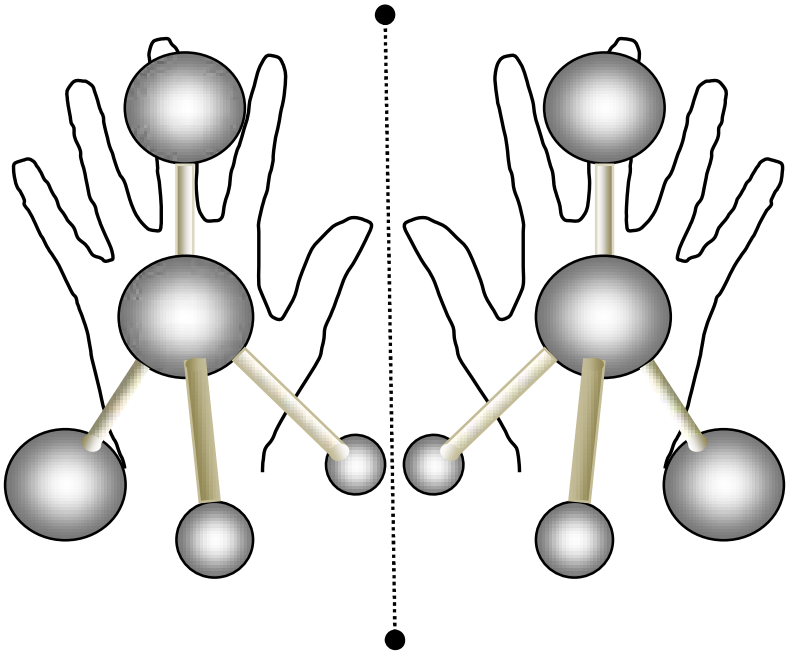

Figure 1.8: Schematic showing the effect of chirality with an enantiomer pair. The enantiomers, like a pair of hands, are identical but non-superimposable mirror images of each other.

1.3.1.1 Optical techniques

The most popular method of distinguishing between enantiomers is using optical circular dichroism (CD) around the visible of the spectrum. A chiral molecules will absorb left– and right–circularly polarised light in different amounts, and CD involves measuring this difference as a function of wavelength. When circularly polarised light interacts with a chiral molecule in solution, the CD can be expressed as,

$$\frac{A_l - A_r}{A_{Tot}} \tag{1.2}$$

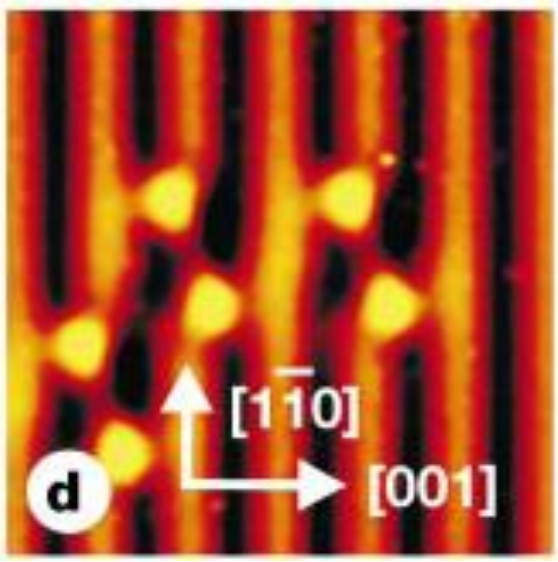

Figure 1.9: (S)–(−)–cysteine pairs fromed on the Au(110) observed by STM, after [84].

where A_l and A_r are absorbances for left– and right–circularly polarised light, respectively, and A_{Tot} is the total absorbance. The responses from CD are extremely weak, typically of the order of 10^{-3} of the total absorbance. Other limitations of this technique include the inability to measure samples in reflection, as the effect is annulled. CD cannot be used to characterise thin films of chiral molecules on planar surfaces.

Chiral detection at the very early stages of a reaction would be a breakthrough, as chiral organic synthesis is complicated and expensive. The key would be to achieve chiral discrimination at the monolayer level, which is difficult on surfaces. Nonlinear optics has the sensitivity to do this. The fact that chiral molecules are, by definition acentric, means SHG is capable, in principle, of detecting enantiomeric excess at surfaces, if it has sufficient sensitivity.

It was the pioneering work by Hicks and co–workers in the 1990s, on thin

films of 1,1'–binaphthalene–2,2'–diol (binol) at fused silica and liquid interfaces, that initiated the use of nonlinear optics, specifically SHG, to reveal chirality from monolayers [41, 42]. They used SHG–CD, which is the nonlinear optical technique analogous to CD which measures the difference in SH efficiency of the sample for left– and right–circularly polarised light as a function of wavelength. Chiral–SHG was observed on thin films of binol on quartz. Using a quarter wave plate the SH efficiency was measured as a function of frequency of the laser, as was tuned towards the resonance energy of binol. A racemic surface, (i.e, a 50:50 mixture of the two enantiomers), yielded no difference in SHG efficiency for the left– or right–circularly polarised light. In bulk binol solutions measured using CD, the effect was found to be small, with absorption coefficients for left– versus right–circularly polarised light varying by a factor of $\Delta\epsilon/\epsilon \approx 0.1\%$, whereas the asymmetry in SHG can reach values up to 100% on resonance. This work was extended to larger molecules, such as cytochrome c, and combined with surface enhanced Raman spectroscopy [86]. More recently, the work by Schanne–Klein *et al* on an acridine substituted Tröger base was shown to have an excitonically enhanced chiral response, that produced a rotation of 66° in the SH polarisation, which was estimated as being six orders of magnitude larger than the linear response (Figure 1.10) [87]. No work has been published on small chiral molecules adsorbed on well–characterised single crystal surfaces, which is an essential first step in probing chiral catalysis at solid surfaces. Small molecules are less polarisable than large ones and it is not clear whether SHG will have sufficient sensitivity to detect the chiral response of a ML of small molecule adsorbed on a single crystal surface.

Two chiral molecules have been studied during the course of this work: cysteine and binol. Cysteine is a small amino acid of considerable biophysical in-

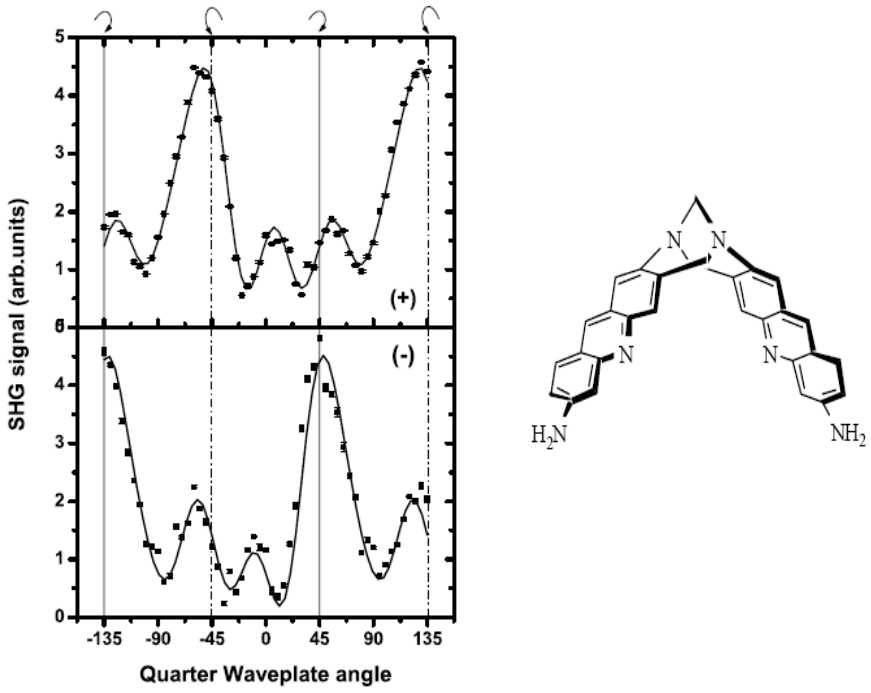

Figure 1.10: α–p response of the acridine substituted Tröger base, as a function of quarter–wave plate angle, showing a 66° rotation between enantiomers. Top: (+) enantiomer, bottom: (−) enantiomer. Arrows at +45° and −135° indicate that the polarisation of the fundamental laser beam is right–circular. The lines indicate the fitted data. Diagram on the right hand side shows the (+)–7S,17S enantiomer of the acridine substituted Tröger base.

terest. Of the 20 natually occurring amino acids, only cysteine contains a thiol group which allows a disulfide bond to be formed with other cysteines, which is important in the formation of active structural domains. In addition, the thiol group, –SH, enables excellent binding to gold surfaces. As mentioned above, it has been shown recently by STM that a racemic mixture of cysteine adsorbed on the Au(110) surface, under UHV conditions, forms homochiral molecular pairs [84], giving compelling evidence for chiral discrimination in molecular interactions at crystalline surfaces. Isted *et al*, used RAS to monitor the deposition

of (R)–(+)–cysteine on Au(110) in both UHV and electrochemical environments [88] and, due to the self–limiting growth of the molecule, a fingerprint spectrum for a cysteine ML adsorbed on Au(110) was obtained. No chiral studies were undertaken and, as RAS is based on reflection, no direct chiral optical response is expected. Indirect effects associated with different adsorption sites at the surface at the surface cannot be ruled out, however.

In conclusion, the potential for RAS and SHG to compliment well established techniques, for the investigation of surfaces, interfaces, ultrathin films and nanostructures is gathering momentum, which makes epioptics an exciting field to study. The research described in this thesis demonstrates how surface sensitive optical techniques of this kind can be used to characterise plasmonic nanostructures and ultrathin chiral films of small molecules. It is important that these techniques continue to be developed and applied in order to enhance our understanding of the physics and chemistry of these material systems.

Chapter 2

Theory and phenomenology of experimental techniques

> "A painter should begin every canvas with a wash of black, because all things in nature are dark except where exposed by the light."
>
> –*Leonardo da Vinci*

The propagation of electromagnetic waves through a material gives rise to a number of optical processes, including reflection, refraction, absorption and transmission. By measuring the variation of these processes it is possible to define the optical properties of the material. When the intensity of the incoming radiation is low, the resulting optical processes are linear in nature and are described using linear optics (section 2.1). However, if the intensity of the incoming light is very high (such as that produced by lasers), a number of different phenomena can be

observed; these effects are described by nonlinear optics (Section 2.2).

2.1 Linear optical response of materials

Under low incident light intensities, the forces exerted on electrons are small compared to their binding energy. As a result, the electric polarisation induced in the material P depends linearly on the electric field of the light wave,

$$P = \epsilon_0 \chi^{(1)} E \tag{2.1}$$

where ϵ_0 and $\chi^{(1)}$ are the dielectric permittivity and the first order susceptibility respectively. $\chi^{(1)}$ is a measure of the extent to which the incoming electric field causes polarisation and can be seen in the form,

$$\epsilon = 1 + \chi^{(1)} \tag{2.2}$$

where ϵ is the complex dielectric function, and is described as,

$$\epsilon = \epsilon_1 + i\epsilon_2 \tag{2.3}$$

This can be related to the complex refractive index N by taking the square root of the dielectric function,

$$N = n + ik = \sqrt{\epsilon_1 + i\epsilon_2} \tag{2.4}$$

where n is the real part of the complex refractive index and k is the extinction coeffient. The complex refractive index is a frequency dependent quantity accounting for the absorption of light with increasing distance into the material. Equation 2.4 can then be solved to obtain,

$$\epsilon_1 = n^2 - k^2 \tag{2.5}$$

$$\epsilon_2 = 2nk \tag{2.6}$$

leading to,

$$n = \frac{1}{\sqrt{2}}(\epsilon_1 + (\epsilon_1^2 + \epsilon_2^2)^{\frac{1}{2}})^{\frac{1}{2}} \tag{2.7}$$

$$k = \frac{1}{\sqrt{2}}(-\epsilon_1 + (\epsilon_1^2 + \epsilon_2^2)^{\frac{1}{2}})^{\frac{1}{2}} \tag{2.8}$$

If the medium is only weakly absorbing from Equation 2.6, ϵ_2 is very small and $n \approx \sqrt{\epsilon_1}$ is thus determined by the real part of the dielectric constant. The reflectivity, R, also depends on both n and k, and at normal incidence we have:

$$R = \left|\frac{N-1}{N+1}\right|^2 = \frac{(n-1)^2 + k^2}{(n+1)^2 + k^2} \tag{2.9}$$

2.1.1 Reflection anisotropy spectroscopy

RAS is a linear optical technique which measures the difference in reflectance Δr, normalised to its total reflectance r, between orthogonal symmetry directions in the surface plane at near normal incidence. Reconstructions of the surface layer or adsorbates cause slight differences in reflectance from the x and y axis in the surface plane, which lead to a RAS signal. The quantity measured is known as

the reflectance anisotropy and is defined as,

$$\frac{\Delta r}{r} = \frac{2(r_x - r_y)}{r_x + r_y} \tag{2.10}$$

where r is the mean reflectance, and r_x and r_y denote reflection coefficients along the orthogonal polarisation axes in the x and y direction respectively. RAS is very useful for monitoring *in situ* growth and layer completion because anisotropic surface reconstructions can vary from layer to layer. A comprehensive review of RAS has been published by Weightman *et al* [10].

Figure 2.1 illustrates the measured polarisation state and the sample orientation of a Au(110) surface. The two main symmetry directions of Au(110) are $[1\bar{1}0]$ and [001]. An anisotropy of the surface will result in a slightly different amplitude and phase component being reflected, converting the incident plane–polarised light into elliptically polarised light. For Au(110) the resulting reflectance anisotropy becomes,

$$\frac{\Delta r}{r} = \frac{2(r_{1\bar{1}0} - r_{001})}{r_{1\bar{1}0} + r_{001}} \tag{2.11}$$

The amplitude of the ellipse is related to the real part of the RAS signal, while the phase of the ellipse represents the imaginary part of the signal. The RAS signal is generally measured using a photoelastic modulator (PEM) (see Section 3.3). An alternative approach is to use a rotating sample setup. However, this can be difficult to implement for *in situ* studies and is less sensitive [89]. The PEM and analyser polariser combination converts a polarisation modulated signal into an intensity modulated signal, which is measured using a detector.

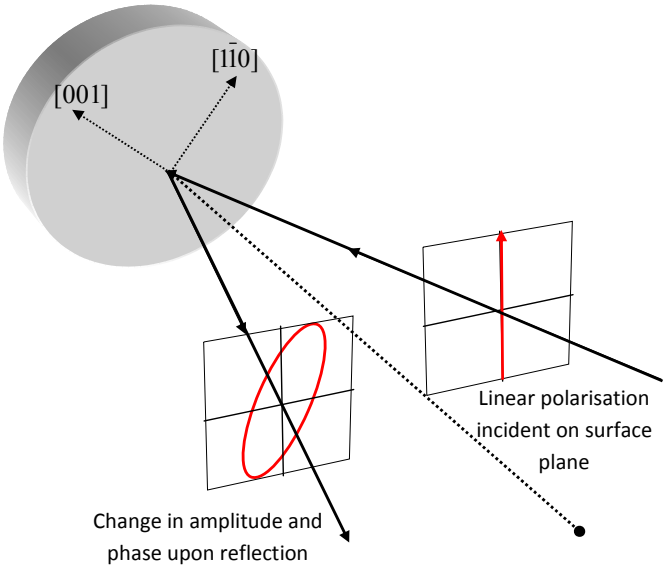

Figure 2.1: Principle of RAS demonstrated on Au(110). Normally–incident light is linearly polarised and upon reflection becomes elliptically polarised due to a phase and amplitude change which is related to the in–plane anisotropy. Note that the angle of incidence has been exaggerated for clarity.

2.1.1.1 Origin of a RAS signal

RAS is sensitive to surface structure by symmetry considerations. The bulk structure of cubic materials will yield no RAS response i.e. $\epsilon_{xx} = \epsilon_{yy}$, while the surface will often reconstruct to break cubic symmetry, so any sizeable RAS response from cubic materials will be due to the surface or interface region. Non–vicinal anisotropically reconstructed (100) or (111) surfaces of cubic materials should give a response, but two or three equivalent domains, respectively, often form at the surface which prevents a RAS signal from being observed, as the beam samples a macroscopic area, over which the cubic symmetry is restored, and the signal averages to zero. The (110) surfaces of cubic materials are anisotropic

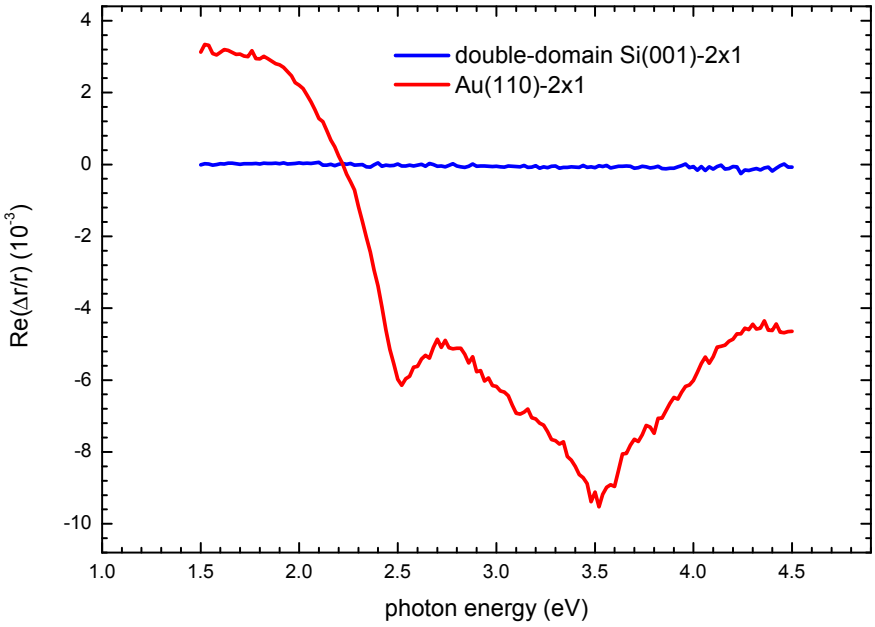

Figure 2.2: Comparison of the RAS response of Au(110)–2×1 and double–domain Si(100)–2×1.

and tend to form single domain surfaces. The RAS response from reconstructed Au(110)–2×1 and double domain Si(100)–2×1 are compared in Figure 2.2. The clean Au(110) surface reconstructs at room temperature to produce a 2×1 'missing row' reconstruction [90], which was confirmed with LEED (see Figure 3.12). The RAS features above 3 eV are thought to arise from surface modified bulk transitions, while the RAS response in the region 1.5–2.5 eV is sensitive to surface reconstruction [91, 92]. Studies of various semiconductors have found that the electronic bands of the bulk crystal are modified by the presence of a surface layer, which in turn contributes to the RAS profile [93], and it is thought that similar contributions occur in metals.

Several phenomenological models have been developed in order to relate the optical anisotropy to the surface dielectric function, the most widely used of which

is the three phase model of McIntyre and Aspnes [94]. In this approach, a thin anisotropic layer of thickness d, is located between a semi–infinite isotropic bulk, of dielectric function ϵ_b, and a semi-infinite ambient layer of dielectric function ϵ_m. The surface anisotropy ϵ^s is then expressed by the two different diagonal tensor components in the x and y direction, ϵ_{ii}. The RAS signal for a detector in the ambient region is given by,

$$\frac{\Delta r}{r} = \frac{4\pi d\sqrt{\epsilon_m}}{\lambda} \frac{i(\epsilon^s_{xx} - \epsilon^s_{yy})}{\epsilon_b - \epsilon_m} \tag{2.12}$$

where λ is the wavelength of the light ($d \gg \lambda$). Equation 2.12 can be used to calculate the RAS response when $\Delta\epsilon^s$ is determined using *ab initio* electronic structure theories [10].

2.1.2 Spectroscopic ellipsometry

Spectroscopic ellipsometry (SE) is a linear optical technique widely used for the characterisation of thin films [95]. This well established method that, in its general form, is useful for analysing a number of parameters including layer thickness, dielectric function and surface and interfacial roughness (and thus constituent and void fractions). However, in order to extract this information, modelling is required to allow full optical characterisation of thin films [96].

Ellipsometry works on the principle that linearly polarised light reflected from the surface of the thin film becomes elliptically polarised as shown in Figure 2.3. The change in polarisation is measured by analysing the light upon reflection from a sample. This technique directly measures two values: Ψ and Δ, where Ψ is the azimuth of the ellipse of the reflected light, i.e. the angle between the

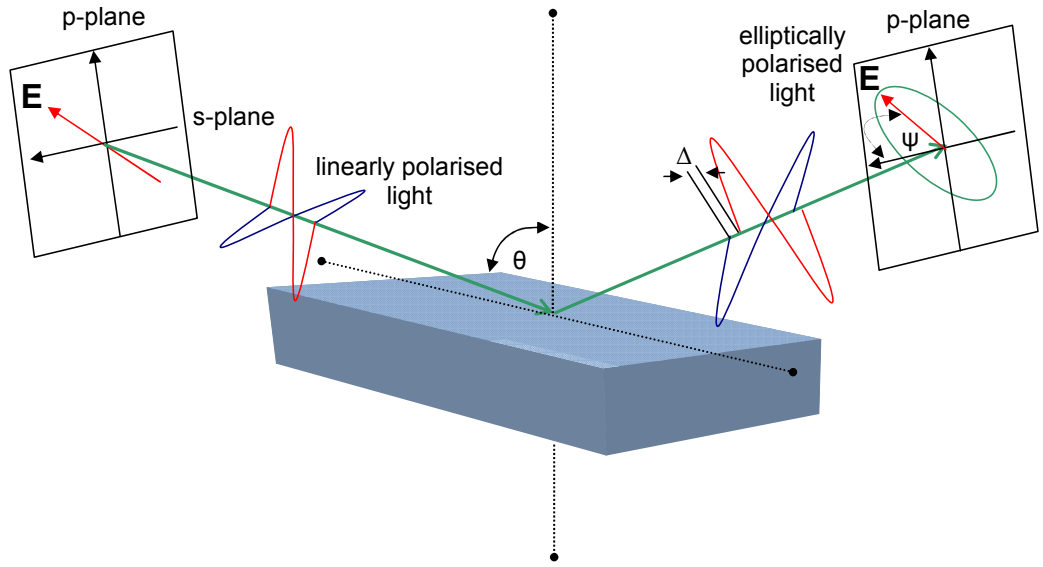

Figure 2.3: The principle of ellipsometry. When linearly polarised light is incident on the sample, the reflected light is elliptically polarised. The ellipticity of the reflected light depends on the optical constants of the sample.

major axis of the ellipse and the positive direction of the x axis [97], while Δ is the phase difference between the s and p components (Figure 2.4). Attenuation of the s and p components of light determines the tilt of the ellipse, while the phase shift of the s and p polarised light is related to the ellipticity of the ellipse. The amount of induced ellipticity depends on the optical constants of the material. Ψ and Δ are related to the Fresnel reflection coefficients, r_s and r_p for s and p polarised light respectively, where r is defined as the ratio of reflected to incident electric field amplitude. The complex ratio of the reflection coefficients of light polarised parallel and perpendicular to the plane of incidence is defined by;

$$\rho = \frac{r_p}{r_s} = \tan(\Psi)e^{i\Delta} \tag{2.13}$$

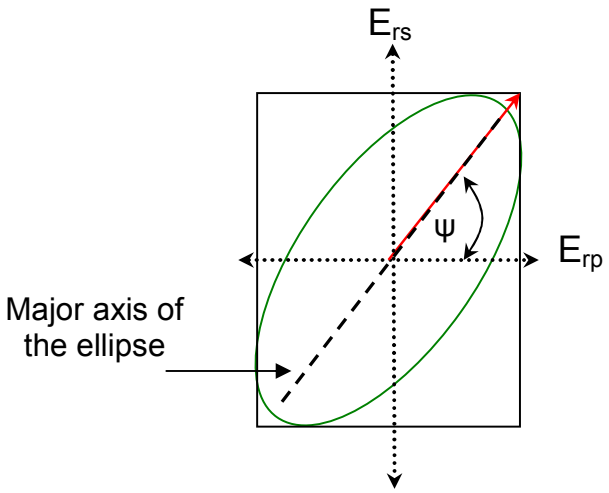

Figure 2.4: When s and p waves are reflected, they experience a phase shift and amplitude reduction (not necessarily the same for both waves) defined by the ellipsometric parameters Ψ and Δ. These parameters determine the ellipticity.

The value of ρ is complex and frequency dependent and contains both the amplitude ratio and phase difference Δ. The quantities in Equation 2.13 are defined as:

$$\tan(\Psi) = \left|\frac{r_p}{r_s}\right| \tag{2.14}$$

$$\cos\Delta = \delta_p - \delta_s \tag{2.15}$$

and are related to the intensity ratio and phase difference δ in the s– and p–polarised reflected beams. The overall response of the volume sampled by the beam is described by the pseudo dielectric function of the sample, which is given by

$$< \epsilon(\omega) >= \sin^2\theta + \sin^2\theta\tan^2\theta\frac{(1-\rho(\omega))^2}{(1+\rho(\omega))^2} \tag{2.16}$$

where θ is the angle of incidence and ρ is given by Equation 2.13. For a general, multi–component system, modelling is required to relate the dielectric function and thickness of the layers to $< \epsilon(\omega) >$ [97].

2.2 Nonlinear optical response of materials

While the interaction of radiation of low intensity with matter is much more common, high intensity, coherent radiation of the order of MW/cm^2, from a laser, causes electrons in a solid to behave nonlinearly as a result of the high electric fields driving them. These nonlinearities contribute to the induced polarisation of the material and can produce complex effects such as sum frequency generation (SFG) and second–harmonic generation (SHG), where a response at twice the exciting frequency can be produced. The electric polarisation P, induced in a material by an electromagnetic field $E(\omega)$ is given by:

$$P(k,\omega) = \epsilon_0[\chi^{(1)}E(k,\omega) + \chi^{(2)}E^2(k,\omega) + \chi^{(3)}E^3(k,\omega) + ...] \tag{2.17}$$

where $\chi^{(i)}$ is the ith order susceptibility tensor of rank $i+1$ describing the material response.

2.2.1 Second–harmonic generation

The advent of the laser led to the first observation of SHG, in 1961 by Franken et al [23], and SHG has been intensively studied since, as described in the book by Shen [98]. The first term on the right hand side of Equation 2.17 describes the linear optical response of the material, exploited in techniques like RAS and

SE where the linear response is the most dominant term. The second term of the expansion describes SFG and SHG.

The SH contribution to the polarisation can come from electric dipole, magnetic dipole and electric quadrupole terms. For centrosymmetric materials with inversion symmetry there can be no bulk electric dipole contribution. At the surface or interface the inversion symmetry is necessarily broken and $\chi^{(2)}$ is no longer forbidden within the electric dipole approximation. In addition to the surface and interface sensitivity that this produces, SHG has the normal advantages of linear optical techniques. The development of fs lasers has made SHG a non–destructive technique since the lasers have low average power, which minimises sample heating. The nonlinear polarisation describing SFG and SHG is given by

$$P_i(2\omega) = \epsilon_0[\chi^{(2)}_{ijk} E_j(\omega) E_k(\omega)] \tag{2.18}$$

where $\chi^{(2)}_{ijk}$ is the non linear susceptibility tensor. $\chi^{(2)}_{ijk}$ describes the nonlinear polarisation field generated along i, when an optical field is applied along j and k. The second order susceptibility tensor, $\chi^{(2)}$, is a third rank tensor of 27 elements, which depend on the structure and symmetry of the surface or interface. SHG is a special case of three wave mixing, with the number of components reducing from 27 to 18 through the relations [99],

$$E_j(\omega) E_k(\omega) = E_k(\omega) E_j(\omega) \tag{2.19}$$

$$\chi^{(2)}_{ijk} = \chi^{(2)}_{ikj} \tag{2.20}$$

Table 2.1: Non zero $\chi^{(2)}$ components for various symmetry classes.

Symmetry Class	Independent non-zero Elements
1m	xxx, xyy, xzz
	xxz=xzx, yyx = yxy, yyz=yzy
	zxz=zzx, zxx, zyy, zzz
2mm	xzx, yzy, zxx, zyy, zzz
3m	xxx=-xyy=-yyx=-yxy
	zxx=zyy
	xxz=xzx=yyz=yzy
	zzz
4mm, 6mm	xxz=xzx=yyz=yzy
	zxx=zyy
	zzz

The induced nonlinear polarisation therefore becomes,

$$\begin{pmatrix} P_x(2\omega) \\ P_y(2\omega) \\ P_z(2\omega) \end{pmatrix} = \epsilon_0 \begin{pmatrix} \chi^{(2)}_{xxx} & \chi^{(2)}_{xyy} & \chi^{(2)}_{xzz} & \chi^{(2)}_{xzy} & \chi^{(2)}_{xzx} & \chi^{(2)}_{xxy} \\ \chi^{(2)}_{yxx} & \chi^{(2)}_{yyy} & \chi^{(2)}_{yzz} & \chi^{(2)}_{yzy} & \chi^{(2)}_{yzx} & \chi^{(2)}_{yxy} \\ \chi^{(2)}_{zxx} & \chi^{(2)}_{zyy} & \chi^{(2)}_{zzz} & \chi^{(2)}_{zzy} & \chi^{(2)}_{zzx} & \chi^{(2)}_{zxy} \end{pmatrix} \begin{pmatrix} E_x(\omega))E_x(\omega) \\ E_y(\omega)E_y(\omega) \\ E_z(\omega)E_z(\omega) \\ 2E_z(\omega)E_y(\omega) \\ 2E_z(\omega)E_x(\omega) \\ 2E_x(\omega)E_y(\omega) \end{pmatrix} \tag{2.21}$$

The number of components in Equation 2.21 is significantly reduced where the surface contains symmetry elements. Table 2.1 displays the non–vanishing tensor elements for SHG from surfaces and interfaces of different symmetries. Choice of sample geometry and input and output polarisations can be used to simplify the response.

As previously described, SHG is electric dipole forbidden in the bulk of centrosymmetric materials. However, higher order bulk electric quadrupolar and

magnetic dipole terms may contribute [98, 100], and although orders of magnitude smaller, may make a significant contribution due to the excitation volume of the technique.

2.2.1.1 Phenomenological model

In order to use nonlinear techniques as surface or interface probe, a phenomenological model is necessary to relate the SHG efficiency to the linear and nonlinear response of the material. A number of theories for the SH response from surfaces have been developed. Sipe *et al* [101, 102], have provided a detailed phenomenological model of the SH response from the cubic faces of (001), (111) and (110), which include electric dipole and quadrupolar contributions from both surface and bulk. These expressions can be adapted for the measurement approach used thoughout this thesis. This involves rotating the plane of polarisation of the excitation beam by an angle α, while keeping the sample at a fixed azimuthal position aligned along high symmetry directions [103], SH s– or p–polarised output is detected.

For a linearly polarised incident electric field polarised at an angle α to the plane of incidence (see Figure 2.5), field components E_x, E_y, and E_z, can be expressed in terms of α,

$$\begin{pmatrix} E_x(\omega) \\ E_y(\omega) \\ E_z(\omega) \end{pmatrix} = \begin{pmatrix} a\cos\alpha \\ b\sin\alpha \\ c\cos\alpha \end{pmatrix} E(\omega) \tag{2.22}$$

where a, b and c are Fresnel coefficients. Substituting this into Equation 2.21 the

p– and s– components of the reflected SH intensity can be written as:

$$I_p^\alpha \propto [A\cos^2\alpha + B\sin^2\alpha + C\sin 2\alpha]^2 \tag{2.23}$$

$$I_s^\alpha \propto [F\cos^2\alpha + G\sin^2\alpha + H\sin 2\alpha]^2 \tag{2.24}$$

where α is the polarisation vector angle with respect to the x axis. The SH response is fitted to Equations 2.23 and 2.24 where the coefficients A, B, C, F, G and H are a function of the Fresnel coefficients, dipolar second order susceptibility χ_{ijk}, bulk quadrupolar terms and possible third order terms that may arise from electric fields or strain [104]. For a Si(001) interface with 4mm symmetry, the non–zero electric dipole terms, as shown in Table 2.1, are zzz, $zxx{=}zyy$, $xxz{=}yyz$. All of these terms are isotropic for rotation about the sample normal and thus are the same for measurements in the xz or yz plane of incidence. For the s–polarised output, which eliminates all terms of form zjk, only H with the dipole term $xxz{=}yyz$, is non–zero, which results in an overall $\sin^2 2\alpha$ behaviour. For 1m vicinal samples, this result also holds when the plane of incidence is the mirror plane of the system [105]. Many more terms contribute to the p–polarised output, which produces a stronger SH response, but often making interpretation difficult.

Experiments at near normal incidence are a special case: the electromagnetic field vectors lie in the plane of the surface, thus eliminating all z–dependent components and providing in–plane information about the surface or interface. This configuration further reduces the number of elements needed for consideration, which is advantageous for samples of low symmetry. The SHG intensity, at

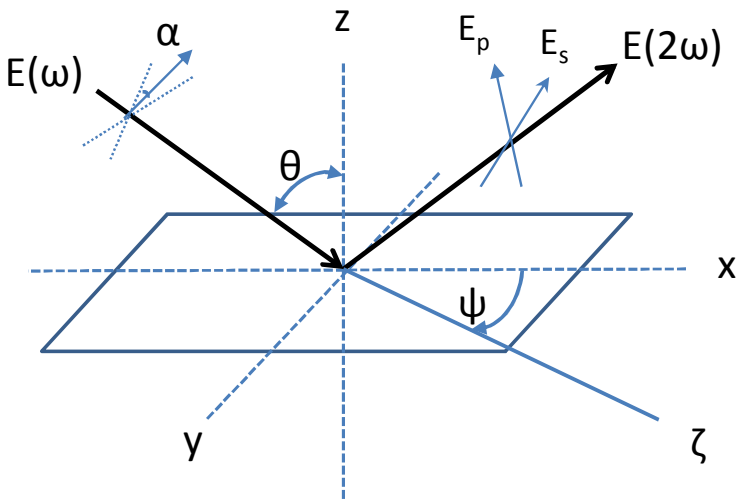

Figure 2.5: SHG geometry in reflection from a surface. The incoming linear field at incidence angle α, to the plane of incidence (xz plane), which lies at an azimuthal angle ψ, to the ζ-axis of the sample. p–polarisation has α=0°, s–polarisation has α=90°. The s– and p–polarised components of the outgoing fields are detected.

normal incidence, in the absence of symmetry is given by,

$$I_x^{2\alpha} \propto \left|\chi_{xxx}\cos^2\alpha + \chi_{xyy}\sin^2\alpha + \chi_{xyx}\sin 2\alpha\right|^2 \tag{2.25}$$

$$I_y^{2\alpha} \propto \left|\chi_{yxx}\cos^2\alpha + \chi_{yyy}\sin^2\alpha + \chi_{yxy}\sin 2\alpha\right|^2 \tag{2.26}$$

Table 2.1 shows that xyx, yxx and yyy are zero for 1m symmetry, and all in-plane components are zero for 2mm and 4mm symmetries. This shows how individual $\chi^{(2)}$ tensor elements can be isolated. No SHG will be detected using this experimental geometry from surfaces and interfaces of 2mm and 4mm symmetries.

2.2.2 Investigation of chirality using SHG

Circular Dichroism (CD) is a measure of the difference in the spectral absorption between left– and right–circularly polarised light. CD is the main technique for probing chiral molcules in solution, but cannot detect chirality in ultrathin films of small molecules at surfaces, as the response is too weak. The theory of chiral SHG expresses the optical activity in terms of the rotational strength R, which results from the interaction between the electric and magnetic dipole transitions, and is defined as:

$$R = \mathrm{Im}(\mu \cdot \mathbf{m}) \tag{2.27}$$

where μ and m are the electric dipole and the magnetic dipole transition moment respectively. If the molecule has a centre of symmetry either the sum of all induced electric and magnetic dipoles is zero, or the vectors representing the magnetic and electric dipoles are orthogonal to each other [41, 42, 106], the result being no optical activity is revealed. The dot product $\mu \cdot \mathbf{m}$ is very small compared to μ, however chiral molecules are inherently acentric, which gaurantees a dipolar SH response. Placing chiral molecules on an isotropic, centrosymmetric surface will give rise to a SH response from the interface between the two media. The nonlinear optical response offers the advantage of measurement in reflection, and macroscopic averaging does not remove the chiral dipolar SHG response, in contrast to solutions of achiral molecules where the dipolar response averages to zero.

2.2.2.1 Phenomenological model

As mentioned above, in addition to the usual electric dipole moment, chiral molecules also respond to the magnetic component of the driving field; as a result the induced polarisation for chiral molecules is,

$$P_i(2\omega) = \chi_{ijk}^{eee} E_j(\omega) E_k(\omega) + \chi_{ijk}^{eem} E_j(\omega) B_k(\omega) \tag{2.28}$$

where e and m indicate the electric and magnetic contributions to the second order susceptibility tensor components χ_{ijk}, while E and B are the fundamental electric and magnetic fields, respectively. For a magnetic dipole interaction at 2ω, the second order nonlinear surface magnetisation is;

$$M_i(2\omega) = \chi_{ijk}^{mee} E_j(\omega) E_k(\omega) \tag{2.29}$$

Instead of the usual $\chi^{(2)}$ for nonlinear susceptibility, separate dipole contributions are identified: χ^{eee}, χ^{eem} and χ^{mee}, where the last two superscripts identify the interaction of two input photons, and the first superscript is the creation of an output photon as a result of the electric dipole interaction e, or the magnetic dipole interaction m [107]. In *Lehrbuch der Optik* [108], Drude described optical activity by assuming that electrons within chiral molecules are forced to move along a helix by the incoming radiation. This can seen in Figure 2.6 where the polarisation and magnetisation induced by the incoming field forces the electrons to move in a helical path. The source of radiation contains a field parallel to the electric dipole, $E(\mu)$, as well as a field perpendicular to the magnetic dipole, $E(m)$. A rotation of the plane of polarisation is obtained by summing these

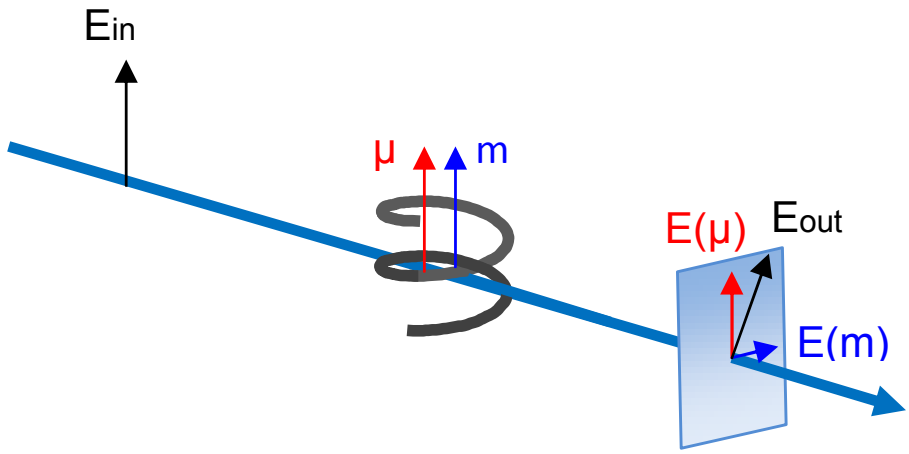

Figure 2.6: Optical activity of a helical molecule. The absorption of a photon causes an electric μ, and a magnetic transition moment m in the helical molecule. This interaction results in a rotation of the plane of polarisation, which is opposite in direction for two enantiomers.

vectors, while changing the handedness changes the sign of optical rotation. Each chiral molecule occurs in two enantiomers which are mirror images of each other, and for the two enantiomers the magnetic dipole transitions are equal but opposite in sign.

If the molecules are assumed to be distributed isotropically in the surface plane then the usual electric dipole ijk terms, zzz, $zxx{=}zyy$, $xxz{=}yyz$ are present. However chirality introduces components of the form xyz and its permutations. In Table 2.2 the nonvanishing tensor components for achiral and chiral surfaces are identified. In our experimental setup, the plane polarised input beam was passed through a quarter wave plate. Such wave plates are generally used to produce right– and left–circularly polarised light. In our case, the wave plate is rotated, which offers some advantages in terms of the tensor components that can be extracted [109]. While these experiments can be performed at a frequency

Table 2.2: Independent components of tensors χ^{eee}, χ^{eem} and χ^{mee}, for both achiral and chiral surfaces [110].

Susceptibility	Isotropic and achiral	Isotropic and chiral
χ^{eee}	zzz	zzz
	zxx=zyy	zxx=zyy
	xxz=xzx=yyz=yzy	xxz=xzx=yyz=yzy
		xyz=xzy=-yxz=-yzx
χ^{eem}		zzz
		zxx=zyy
		xxz=yyz
		xzx=yzy
	xyz=-yxz	xyz=-yxz
	xzy=-yzx	xzy=-yzx
	zxy=-zyx	zxy=-zyx
χ^{mee}		zzz
		zxx=zyy
		xxz=xzx=yyz=yzy
	xyz=xzy=-yxz=-yzx	xyz=xzy=-yxz=-yzx

which is close to a dipole allowed transition (at ω or 2ω) in order to enhance the SH signal, the work outlined in this thesis presents studies in the nonresonant regime, where the incoming laser frequency and its harmonic are far away from dipole resonances. For a rotating quarter wave plate at an angle θ between its fast axis and the p–polarised direction, the intensity of the second harmonic, is given by the equation,

$$I(2\omega) \propto (f' - g' + 4f'' \cos 2\theta - (f' - g') \cos 4\theta + 2h'' \sin 2\theta - h' \sin 4\theta)^2 + (f'' - g'' - 4f' \cos 2\theta - (f'' - g'') \cos 4\theta - 2h' \sin 2\theta - h'' \sin 4\theta)^2 \quad (2.30)$$

where the real and imaginary parts f', g', h', f'', g'' and h'' involve combinations of Fresnel coefficients and tensor components [111]. For p–polarised output, f and g depend only on achiral components, while h depends only on chiral compo-

nents, which change sign for measurements between enantiomers. For s–polarised output, this classification is reversed. For nonresonant measurements the electric dipole terms are real and the magnetic dipole terms are imaginary. Chiral effects can be detected using SHG if there is a sufficient phase difference between chiral and achiral components [112]. A simultaneous nonlinear least squares fit of Equation 2.30 to both enantiomers was used, but reversing the sign of h between the enantiomers (or f and g for s–polarised output).

Chapter 3

Experimental techniques and procedures

"Experimenters are the shock troops of science"

–*Max Planck*

This chapter discusses the techniques and procedures used during the course of this work. The experimental details of sample preparation for the two main experiments are described: the preparation of rippled silicon templates and the preparation of chiral samples. The optical techniques used to characterise the samples are dicussed in detail, while the conventional surface science techniques used are also outlined.

3.1 Ultra high vacuum (UHV)

The optical techniques used for this work are highly surface and interface sensitive, and are strongly affected by adsorbates including contaminants which change the structure and hence the properties of the surface. In order to quantify the optical properties and the effect of adsorbates on the sample, atomically clean surfaces are required. Using the kinetic theory of gases a simple calculation shows that the time taken for the adsorption of one monolayer (ML) of contaminant gas, at a pressure of 1×10^{-9} mbar and assuming a sticking coefficient of 1, is of the order of 1500 seconds (approximately half an hour). Thus a pressure of 1×10^{-10} mbar allows sufficient time to perform optical characterisation before the surface is significantly contaminated. A lower pressure is, of course, desirable as one increases the time available for an experiment.

Two vacuum systems of similar design were used during the course of this work; one for chiral studies and one for silicon studies. The systems achieve a base pressure below $1x10^{-10}$ mbar after baking to 400 K. Evacuation is achieved by the use of a rotary pump with a turbo molecular pump. After baking, UHV is maintained with an ion pump and cycles of the titanium sublimation pump (TSP). Both chambers are equipped with LEED (see section 3.5.1) and AES (see section 3.5.2) optics to determine surface quality prior to RAS and SHG experiments. The position of the strain relieved window used for *in situ* RAS and off-normal SHG measurements is shown schematically in Figure 3.1. The second UHV system is similar.

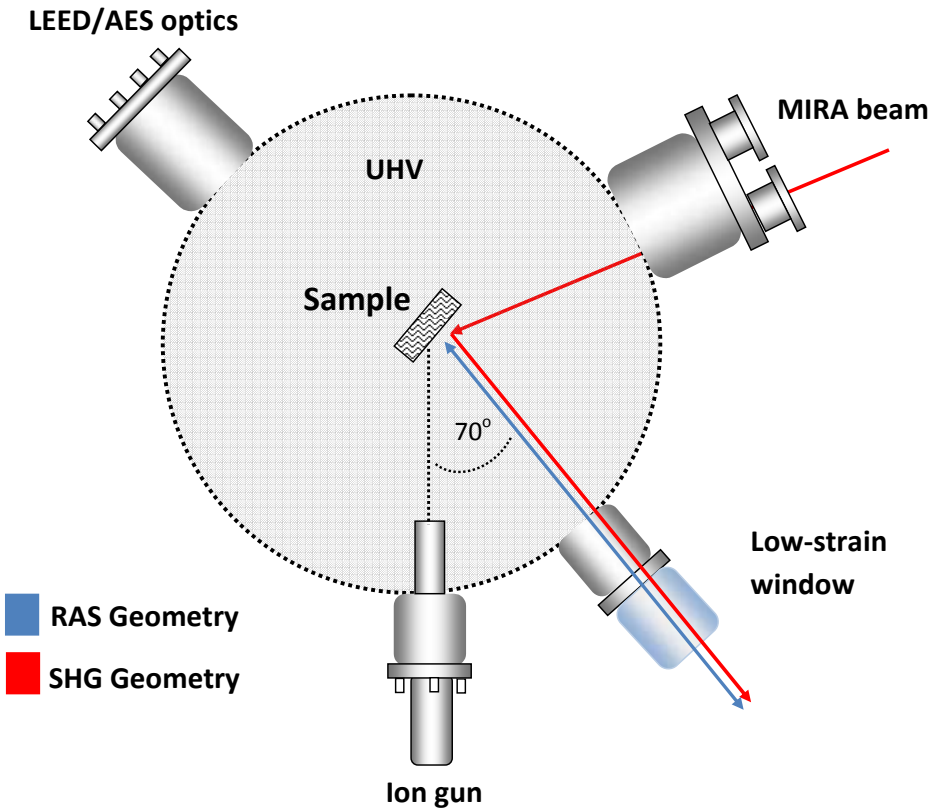

Figure 3.1: Schematic cross-section of the vacuum system, showing the typical geometry used for both RAS and SHG studies. For rippled Si samples the ion gun is directed at 70° from the surface normal to grow ripples, allowing the RAS signal to be monitored in real time. While for off-normal SHG studies the sample was re–orientated and placed at 45° to incident laser beam

3.2 Sample preparation

3.2.1 Rippled silicon templates

All the samples were made using offcuts from commercially available single crystal Si(001) wafers as the substrate. The samples were prepared in UHV conditions,

Figure 3.2: Sample holder used for preparing rippled Si in UHV. Tantalum pieces are coloured grey, white indicates ceramic pieces, and orange indicates the Si sample.

which in this context means below 10^{-10} mbar. The sample was first allowed to outgas for several hours at 870 K, until the pressure stabilised below 10^{-10} mbar. The sample is then cleaned by flash heating to approximately 1470 K. Temperatures above 800 K were measured using an optical pyrometer. The emissivity of the Si sample was set to 0.66 by using a Pt resistance thermometer at the lower end of the temperature range. The estimated error in the sample temperature readings is ± 20 K. Resistive heating was used to heat the sample; in this approach the substrate is heated directly, producing an increase in thermal charge carriers and hence conductivity. This is possible due to the negative coefficient of resistance of Si. A high voltage is first applied across the sample to break down the native oxide layer and create enough thermal carriers for conduction. Once a current has been established, the sample can then be uniformly heated below the melting point of the sample. The samples are clamped to the simple sample holder (Figure 3.2), and current is passed through the sample via the positive and negative terminals. Low energy electron diffraction (LEED; Section 3.5.1), and Auger electron spectroscopy (AES; Section 3.5.2) were used to confirm a

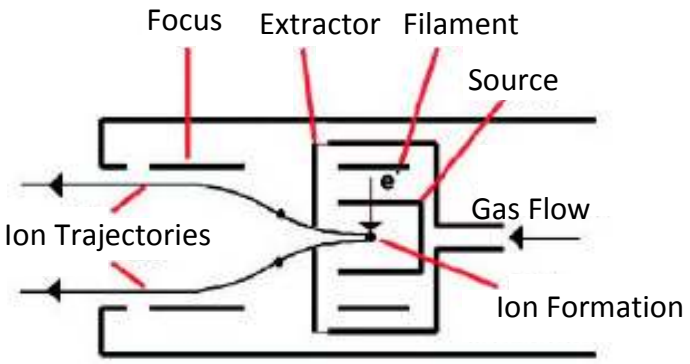

Figure 3.3: Ion gun used to make rippled samples. The ion gun ionizes Ar atoms in the source region of the gun, extracts and columnates the ions, and directs the beam at the sample.

clean and ordered surface. The ripples were created by irradiation of the sample surface using high energy Ar ions at 500 eV from an ion gun at an angle of incidence of 70°. Gas atoms in the source region of the gun are ionised, extracted and accelerated towards the sample as a beam (see Figure 3.3). The ion flux used in these experiments remained constant at 1×10^{17} $m^{-2}s^{-1}$. The greater the ion fluence (the total number of ions impinging on the sample) the longer the periodicity of the ripples [113, 114], as the process is cumulative. The projection of the ion beam was aligned along a main azimuth on the substrate e.g. the [100] direction. The evolution of the ripples was monitored *in situ* using RAS and SHG (see sections 3.3 and 3.4). The ripple morphology was confirmed using Atomic Force Microscopy (AFM), where the profiles and ampitude of the ripples could be determined (Figure 3.4).

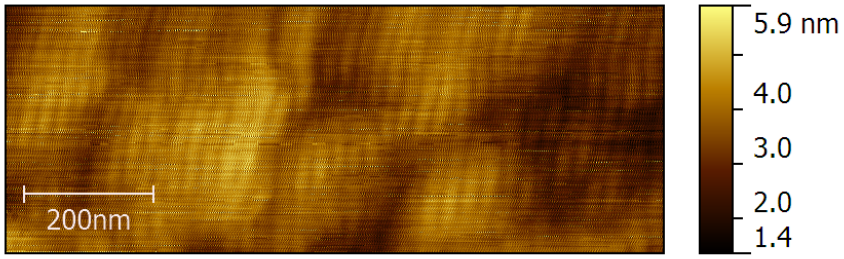

Figure 3.4: AFM of a rippled Si sample template created by ion bombardment.

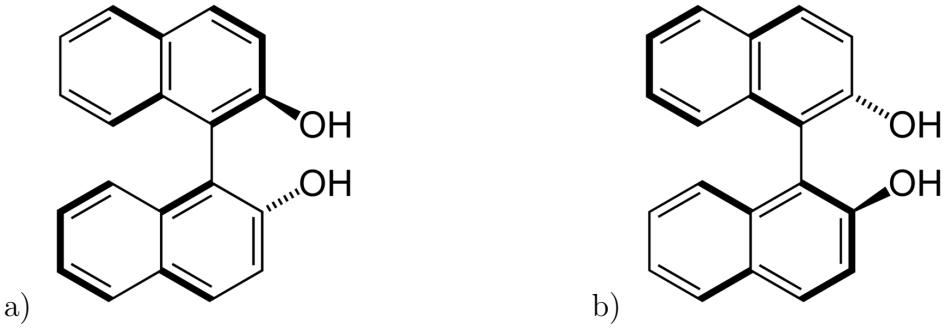

a) b)

Figure 3.5: a) 2-D skeletal image of R–binol b) 2-D skeletal image of S–binol

3.2.2 Preparation of chiral binol samples

1,1'–binaphthalene-2,2'–diol (binol), is an organic compound frequently used as a ligand for transition metal catalysed chiral synthesis, available in R– and S–forms (Figure 3.5). A 0.4 Kg/L solution of binol dissolved in dichloromethane (CH_2Cl_2) was prepared and deposited on fused silica glass and on a Si wafer using a pipette. The solvent evaporates leaving behind a thin film of binol. Assuming that the solution spreads evenly and, based on drop size, the liquid film thickness is 100 μm, an average thickness after evaporation of $\sim$40 nm is expected theoretically. The thickness of the binol films was measured using spectroscopic ellipsometry (SE; see Section 3.6) and was found to be 22 ± 3 nm.

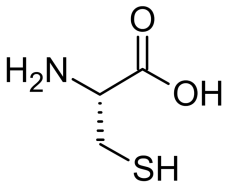

Figure 3.6: 2-D skeletal image of (R)–(+)–Cysteine molecule (L–cysteine)

3.2.3 Preparation of chiral cysteine films

Cysteine, is an amino acid, one of the building blocks of proteins that are used throughout the body. It is usually found in foods such as poultry, yogurt, egg yolks and various vegetables. Cysteine protects cells from free radical damage and helps breakdown extra mucous in the lungs.

Thin cysteine films were prepared on Si(001) was prepared by dissolving a —- solution in de–ionised water. The solution was then deposited on a Si(001) substrate. When the solvent evaporates, a thin film of cysteine is left behind.

Thin cysteine films on Au(110) were also prepared. The substrate was a Au(110) single crystal of 5N purity, cut and polished by Surface Preparation Laboratory (`www.spl.eu`), of 8 mm diameter and 1.2 mm thickness. The sample was mounted on 0.25 mm diameter tungsten wire, which was looped through the sample via two cylindrical holes spark-eroded by the manufacturer. The sample was then spot welded onto two molybdenum rods, which are part of the sample holder (Figure 3.7). The sample was heated by a tungsten filament located directly behind the sample. The temperature was measured using an R–type thermocouple located in a hole speark-eroded by the manufacturer. The sample was cleaned by repeated cycles of Ar^+ etching and annealing. The ion etching serves to remove unwanted contaminants such as C, O or S that

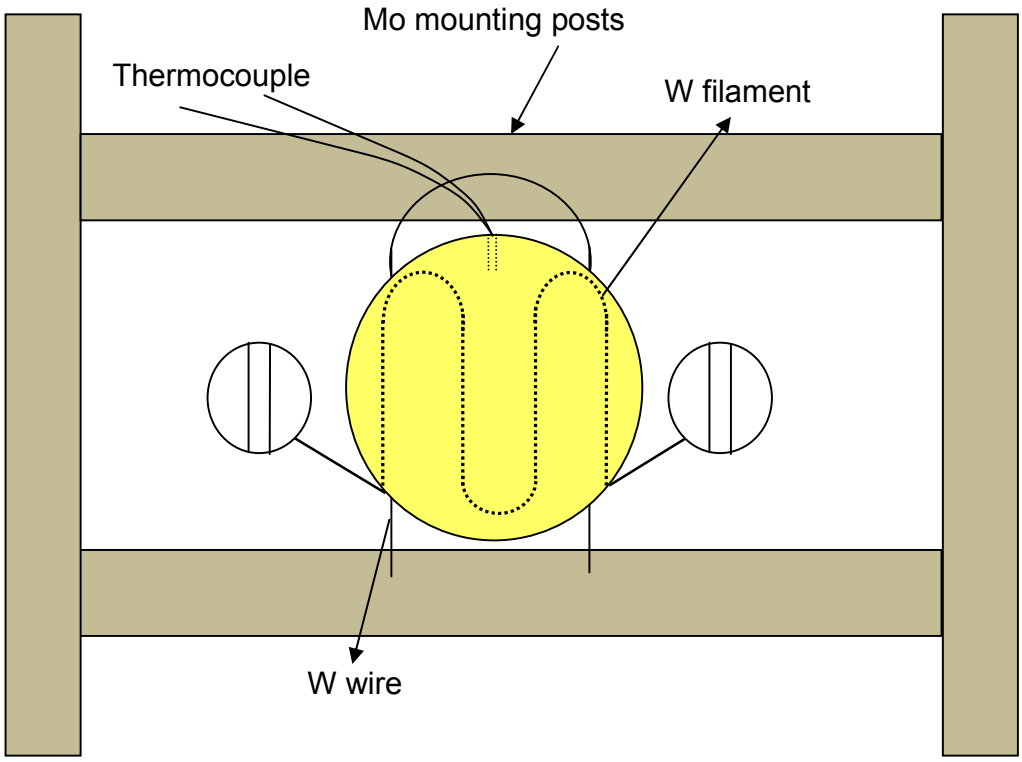

Figure 3.7: Diagram of the sample holder for the Au(110) substrate. The tungsten mounting wire is spot welded to the molybdenum rods. The dotted black line indicates the W filament for sample heating mounted directly behind the Au. The temperature was measured using an R–type thermocouple.

segregate to the single crystal surface. The annealing recrystallizes the sample surface, forming a well ordered surface where any damage caused by the ion etching process has been removed. The ion etching process involved backfilling the chamber to 5x10^{-6} mbar of Ar gas via a leak valve on the ion gun. The sample was then put through numerous cycles consisting of 20 minute sputter sessions at 500 eV at room temperature, followed by a 10 minute anneal at 700 K, as this yields the largest domains of the Au(110) 2×1 'missing row' structure [115]. The

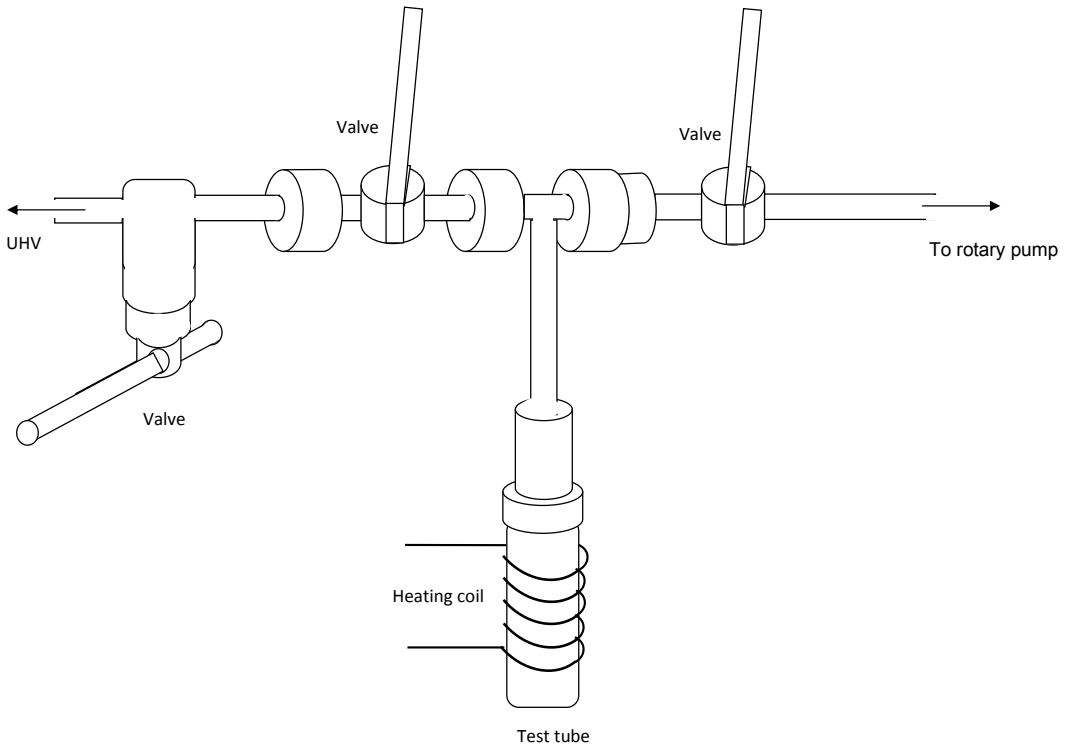

Figure 3.8: Cysteine deposition attachment for the UHV system.

cycling gradually exhausts the surface region of impurities that segregate to the surface. The surface quality was confirmed using LEED, Auger and RAS.

Cysteine was sublimed onto the sample surface in UHV from a pyrex test tube (Figure 3.8). The attachment to the UHV chamber was pumped down, and the cysteine outgassed to 400 K. The valve to the pumping line was then closed, the cysteine heated to approximately 430 K, and finally the valve to the UHV system was opened. A background pressure of 10^{-6} mbar of cysteine was established for about 45 minutes by passing a current of 200 mA through a heating coil surrounding the test tube. The temperature was measured using a K-type thermocouple. The deposition is monitored *in situ* using RAS to compare with

previous work done by Weightman *et al* [88].

3.3 Reflection anisotropy spectroscopy

3.3.1 Introduction

As was discussed in Chapter 1, RAS is a non-destructive, non-invasive optical technique used to probe surfaces and interfaces. The technique measures the difference, Δr, normalised to its total reflectance, r, between the normal incident reflectances for two orthogonal polarisation directions in the surface plane of the material system under investigation. RAS is sensitive to optical anisotropy in thin films and nanostructures at the surface and interface, if the bulk is isotropic. An isotropic surface or bulk structure has equal reflectivities from both the x and y directions on the surface plane and will yield no RAS response; this is the case with the double–domain Si(001)–2×1 surface discussed previously (Figure 2.2).

3.3.2 Experimental arrangement

The apparatus consists of a broad band light source (Xe lamp), an input polariser which cleans up the polarisation before illuminating the sample at normal incidence, a photoelastic modulator (PEM), which alternates the polarisation between 0 ° and 90 °, an output polariser which converts the polarisation modulation into an intensity modulation, and finally the monochromator and detector. The RAS system, shown schematically in Figure 3.9, follows the design as described in [10]. The incident polarisation is chosen to be at 45 ° with respect to two main orthogonal symmetry directions of the sample, in order for the PEM to modulate

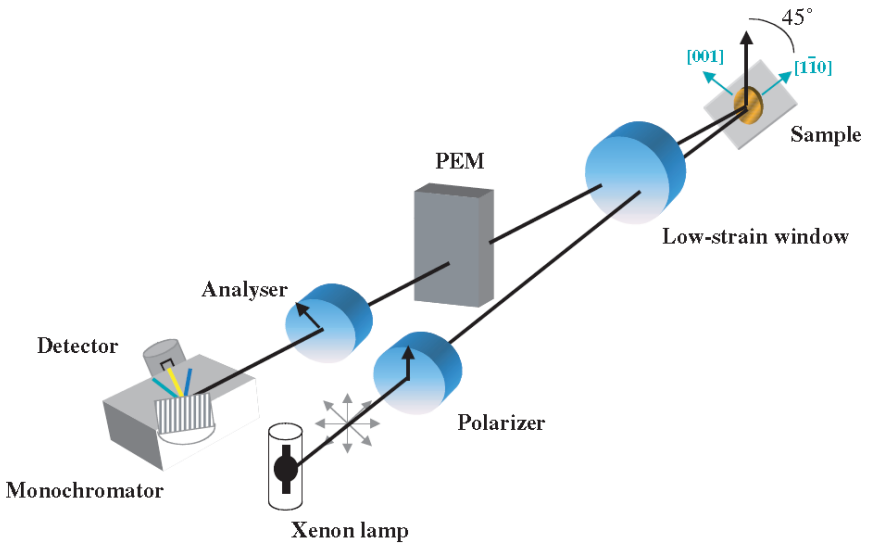

Figure 3.9: Diagram of a PEM RAS setup, after [10]. When performed *in situ*, a low strain window must be fitted to the chamber, as strain in the window produces an artificial RAS signal.

the polarisation along orthogonal axis to measure anisotropy. Two RAS systems of similar design were used, a smaller system with an energy range of 0.76-5 eV, and a larger broad band system with an energy range of 0.42-5 eV (Figure 3.9). The smaller, more portable RAS consists of a Xe lamp, MgF_2 coated aluminium mirrors, quartz Glan-Taylor polarisers, a fused silica PEM, a Si-InGaAs detector (Electronik Manufaktur Mahlsdorf [116]) and a double grating monochromator. The components that differ in the broad band RAS are the MgF_2 polarisers, the CaF_2 PEM, a LN cooled InAs detector and a triple grating monochromator. A Labview (National Instruments) program facilitates the interchangability between the components. Several types of measurements are possible with this setup: spectral RAS, time-dependent RAS to monitor growth, and magnetic field dependent measurements of the polar magneto–optical Kerr effect [MOKE; 117–119].

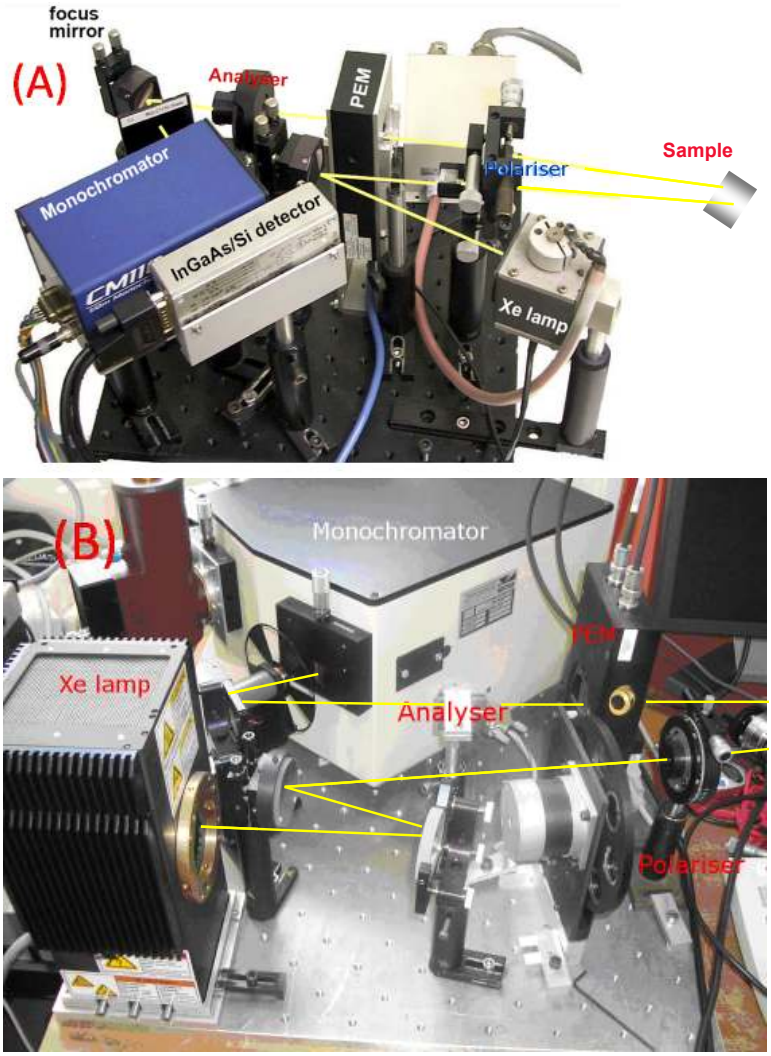

Figure 3.10: a) Small RAS used for *in-situ* work 0.76-5 eV. b) Broad band RAS 0.42-5 eV

Light polarised parallel to the modulation axis of the PEM will undergo a retardation of Γ, of the form;

$$\Gamma = \Gamma_0 \sin(\omega\ t) \tag{3.1}$$

where Γ_0 is the modulation amplitude and ω is the modulation frequency (50kHz).

The effect of light passing through these components on the amplitude can be described using the Jones matrix formalism,

$$A \propto \begin{pmatrix} \cos\frac{\Gamma}{2} & i\sin\frac{\Gamma}{2} \\ i\sin\frac{\Gamma}{2} & \cos\frac{\Gamma}{2} \end{pmatrix} \begin{pmatrix} r_x & 0 \\ 0 & r_y \end{pmatrix} \begin{pmatrix} 1 \\ 1 \end{pmatrix} \propto \begin{pmatrix} r_x \cos\frac{\Gamma}{2} + ir_y \sin\frac{\Gamma}{2} \\ r_y \cos\frac{\Gamma}{2} + ir_x \sin\frac{\Gamma}{2} \end{pmatrix} \quad (3.2)$$

where Γ is the retardation caused by the PEM, and r_x and r_y are reflection coefficients. The resulting intensity at the detector is proportional to $|A|^2$, and is a harmonic series $I_0 + I_\omega + I_{2\omega} + ...$, where I_0 is the time–independent component and the remaining terms are root-mean-square oscillations at the angular frequencies indicated by the subscripts. Setting Γ_0 to 2.405 radians ensures half–wave modulation and hence rotation of the plane of polarisation and leads to [10, 120];

$$\frac{I_{n\omega}}{I_0} = \frac{2J_n(\Gamma_0)\mathrm{Im}[\Delta r/r]}{1 + |\Delta r/r|^2/4} \approx 2J_n(\Gamma_0)\mathrm{Im}\frac{\Delta r}{r} \quad (3.3)$$

where n is an odd integer and J_n is a Bessel function of order n,

$$\frac{I_{n\omega}}{I_0} = \frac{2J_n(\Gamma_0)\mathrm{Re}[\Delta r/r]}{1 + |\Delta r/r|^2/4} \approx 2J_n(\Gamma_0)\mathrm{Re}\frac{\Delta r}{r} \quad (3.4)$$

where n is an even integer. The real and imaginary parts of the reflectance difference $\frac{\Delta r}{r}$, are proportional to the AC/DC ratios of the signal at 2ω and ω, respectively:

$$\mathrm{Re}\frac{\Delta r}{r} \approx \frac{I_{2\omega}}{I_0} \quad (3.5)$$

$$\mathrm{Im}\frac{\Delta r}{r} \approx \frac{I_\omega}{I_0} \quad (3.6)$$

One of the advantages of this setup is that it allows for the possibility of recording both real and imaginary (the first and second harmonic) parts of $\frac{\Delta r}{r}$ using a lock-in amplifier.

3.4 Second–harmonic generation

3.4.1 Introduction

As was discussed in Chapter 1, SHG is a non-linear optical technique used for the characterisation of surfaces and interfaces, which is sensitive to broken symmetries [98]. Where there is a centre of inversion present in a crystal, SHG is bulk dipole forbidden [101]. A break in symmetry at the surface or interface of a crystal, which can be caused by reconstructions, step formation and strain, as well as by local electric or magnetic fields, gives rise to a dipolar second–harmonic response.

3.4.2 Experimental arrangement

As discussed in section 3.1, the experimental approach depends greatly on whether the sample is to be measured *in situ* or *ex situ*. Two geometries are typically used: a rotating sample geometry, which involves rotating the sample while keeping the input and output polarisations fixed, or a rotating polarisation geometry which requires rotating the input (or output) polarisation while keeping the output (or input) polarisation in a fixed position. A rotating polariser configuration was preferred since sample rotation is difficult when working in UHV; all SHG experiments performed for this thesis were made using a rotating polarisation geometry.

Femto-second lasers are used for SHG studies because they are a source of

intense radiation with high peak powers while maintaining a low average power to minimise sample heating. A Coherent Inc. Mira 900–F Ti-sapphire femtosecond laser was used for the SHG work conducted in this thesis. The Mira is pumped by a 5 W continuous wave Verdi laser. The green beam of the Verdi V5 is produced from a laser diode pumped Nd:YVO_4 crystal, frequency doubled using lithium triborate. Passive Kerr lens modelocking produces pulses of approximately 150 fs at a repetition rate of 76 MHz. The spectral width of the pulse is typically 12 nm at the pump wavelength of 800 nm. Diagnostic tools such as a laser spectrum analyser and autocorrelator help to keep the laser working to specification, which is important for sensitive experiments of this kind.

The experimental arrangement for SHG is shown in Figure 3.11. The optical components consist of two Glan Taylor polarisers, a zero order half wave plate for 800 nm, a dielectric mirror working in the 790-1000 nm range and a 50 cm focal length Ag coated concave focussing mirror. To ensure that only the SH signal from the sample was detected a Schott glass filter (OG550) was placed between the focussing mirror and the sample. After reflection from the sample, care was needed in choosing the material of the optical components as, for example, quartz will generate a the SH signal, at 400 nm; for this reason the output optical components (optics after reflection from the sample), consisting of a lens, right angled prism and Pelin Broca prism, are all made of fused silica. The Pelin Broca prism is used to separate the intense first harmonic signal (at 800 nm) from the second–harmonic (at 400 nm) signal using total internal reflection. An additional Schott glass filter (BG39) was placed before the monochromator and removes any additional first harmonic that may have been scattered off the surrounding optics. A photomultiplier tube (PMT) Hammamatsu R1427P was used to detect the SH

in photon counting mode. The photon counter (Stanford Research SR400) was connected to a computer via a GPIB and the counts recorded using a Labview program. Several kinds of SHG experiments are possible: polarisation rotation, sample rotation, time–dependent SHG and magnetic field dependent SHG (also known as MSHG). As a smaller spot size will yield a greater SH response, the Gaussian beam was expanded using a telescope configuration and re–focussed with a concave mirror to achieve a small spot size. Expanding the beam by a factor of 8 makes it possible to focus down to below 100 microns, as measured using the standard knife-edge technique. For SHG measurements involving chiral studies, the half-wave plate is replaced with a quarter-wave plate, in order to produce right and left–circularly polarised light (see Section 2.2.2 for details). For *in situ* chiral studies the arrangement was similar to that shown in Figure 3.11.

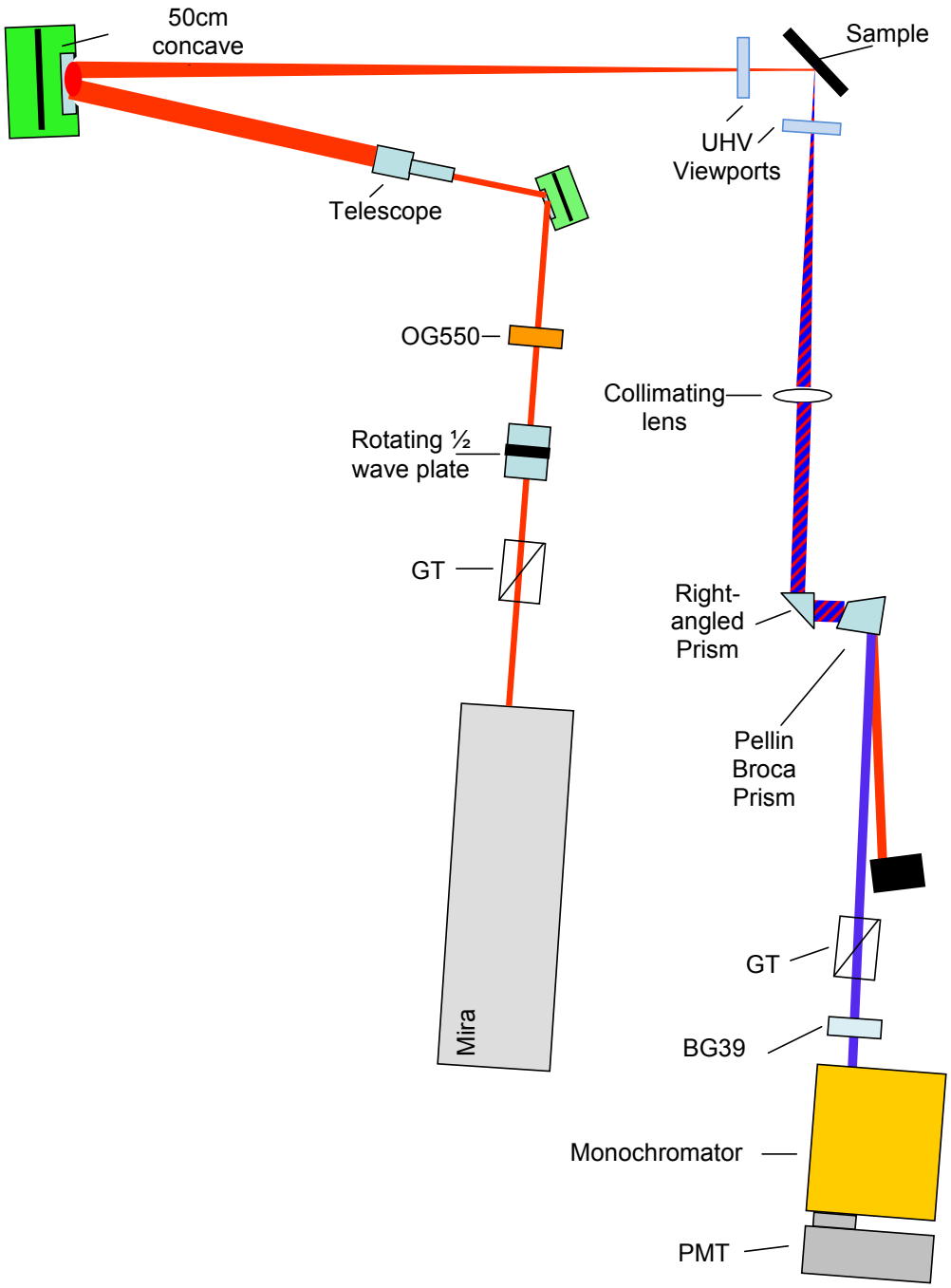

Figure 3.11: Schematic of the rotating polariser SHG experimental arrangement.

3.5 Conventional surface science techniques

3.5.1 Low energy electron diffraction (LEED)

Low energy electron diffraction (LEED) is a technique which uses the diffraction of electrons by a crystal lattice in the surface region to probe its structure. The diffracted beams form a LEED image on a phosphor screen, which is a projection of the lattice in reciprocal space. The position and intensity of the LEED spots (diffraction spots) can yield information on symmetry, size and alignment of the adsorbate unit cell with respect to the substrate unit cell. In this work LEED was used to confirm the formation of the required symmetry. LEED employs a beam of electrons of well defined energy, typically in the range 20-200 eV, which are nomally incident on the sample. A LEED pattern is then generated if the surface is well ordered. The wavelength of electrons given by the de Broglie relation,

$$\lambda = \frac{h}{p} \tag{3.7}$$

where the electron momentum

$$p = mv = (2mE_k)^{\frac{1}{2}} = (2meV)^{\frac{1}{2}} \tag{3.8}$$

V is acceleration voltage and the other symbols have their usual meaning. For a beam of electrons of energy 20 eV, the electron wavelength is 0.3 nm, which is comparable to the size of surface atomic spacings, making this technique highly sensitive to the surface structure. Figure 3.12 shows the LEED pattern from clean Au(110).

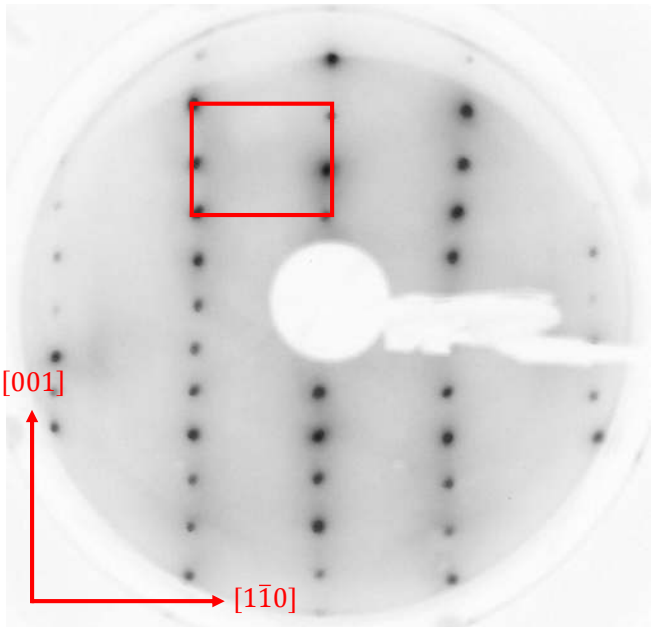

Figure 3.12: LEED image of the clean Au(110)–1×2 reconstruction at 129 eV showing the unit cell and crystallographic directions.

3.5.2 Auger electron spectroscopy (AES)

Auger Electron Spectroscopy (AES) is a technique which measures elemental composition of the surface using the Auger effect. Auger electrons are emitted as a result of a decay of the core hole created by the incident electron beam. As each atom has its own unique spectrum, AES can provide information on the constitution of the surface. AES involves focussing a beam of electrons on the sample surface at a fixed energy of 3 keV, and applying a modulating voltage of 1-10 V peak-to-peak to the middle grids of the retarding field analyser, detecting total secondary electrons using a lock-in amplifier. Both LEED and AES are measured using the same apparatus, an Omicron SpectaLEED rear–view LEED/AES system, (shown in Figure 3.13). Figure 3.15 shows the typical AES spectra from clean Au and Si substrates.

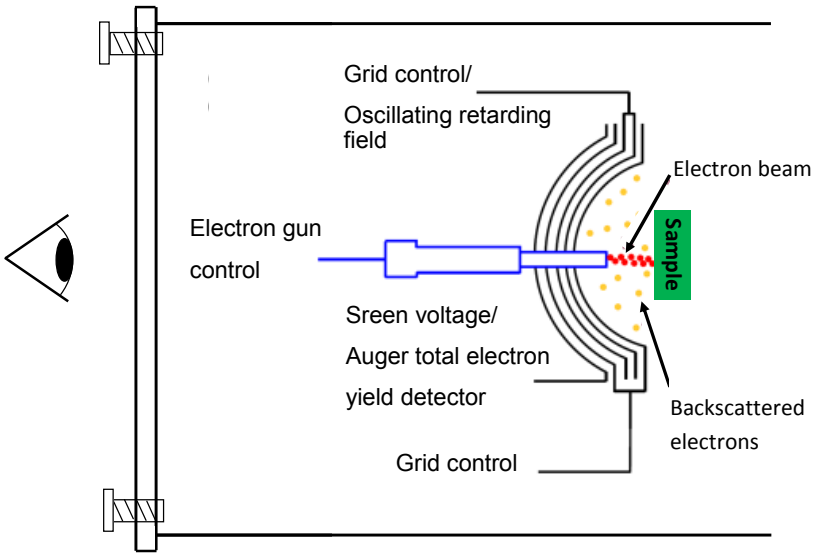

Figure 3.13: Schematic of the LEED-Auger system. To change from a LEED measurement to AES the inner grids are switched to an oscillating retarding field.

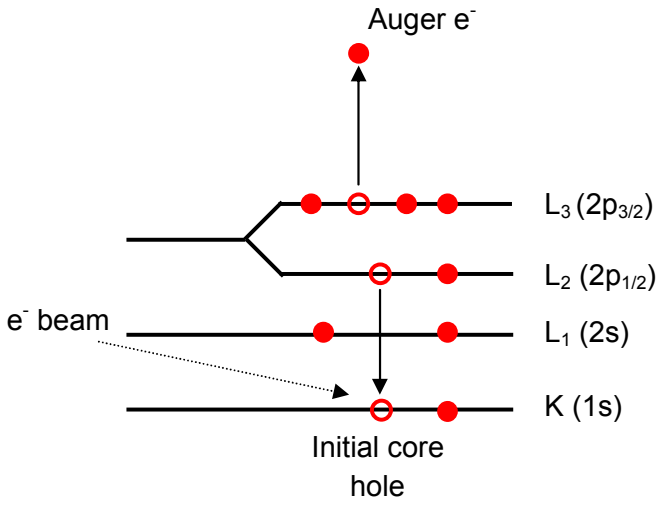

Figure 3.14: Schematic of the Auger effect. By convention, this is described as a $KL_{2,3}L_{2,3}$

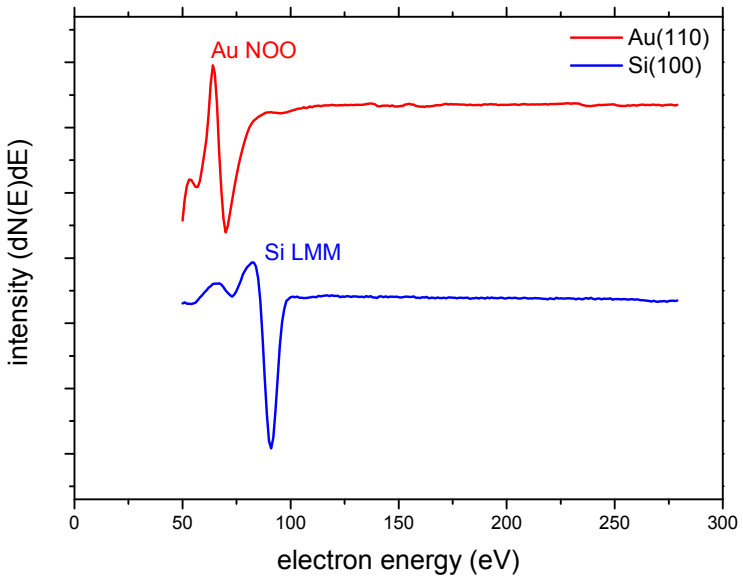

Figure 3.15: AES spectra from clean Si and Au substrates from an energy range of 0-300 eV. The NOO and LMM transitions at 69 eV and 92 eV respectively were confirmed using reference spectra from [121]. An NOO transition is 4f 5d 5d and an LMM transition is 2p 3d 3d, in the more usual notation.

3.6 Spectroscopic ellipsometry

SE is an optical technique which uses the change in polarisation of light upon reflection from a thin film or substrate to determine the dielectric funstion and the thickness of the thin film.

Linearly polarised light reflected by a sample at an oblique angle of incidence becomes elliptically polarised. The reflection coefficient parallel (r_p) and perpendicular (r_s) to the plane of incidence will undergo a phase and amplitude modulation, where r is defined as the ratio of reflected to incident electric field amplitude. Ellipsometry measures the complex reflection ratio ρ, which is then related to $\epsilon(\omega)$ and the angle of incidence θ (see Section 2.1.2).

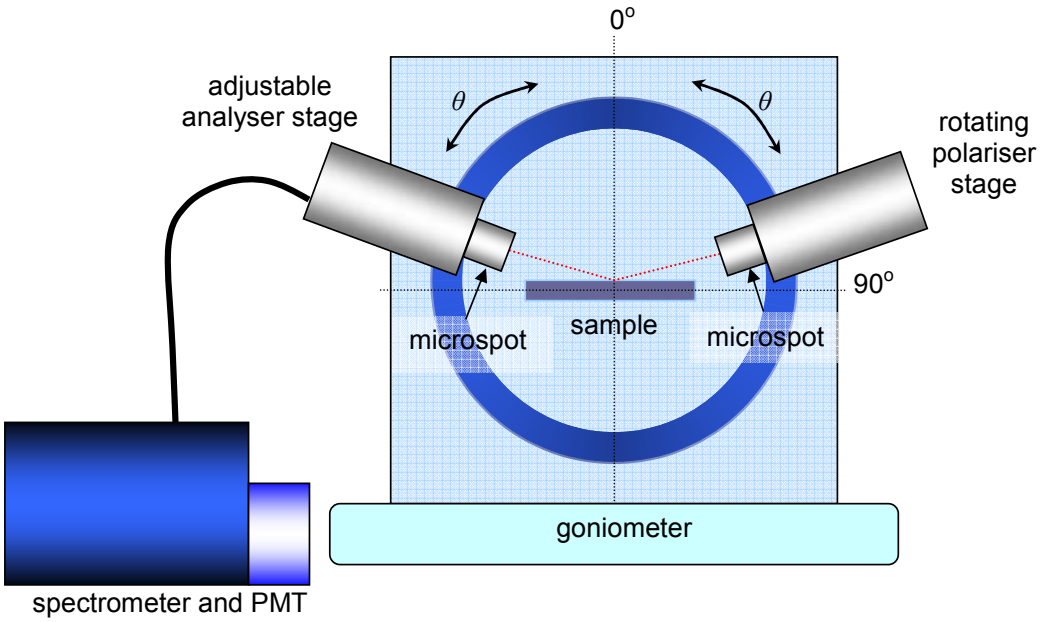

Figure 3.16: Schematic of the ellipsometry system.

The variable angle spectroscopic ellipsometer used was the SOPRA GESP5, which works in a rotating input polariser configuration. The light source is a xenon lamp, chosen for its broad and relatively flat spectrum. After reflection from the sample the signal is measured by an adjustable analyser polariser, monochromator and PMT detector, the input polariser and analyser are quartz Rochon polarisers attached to stepper motors. SOPRA multi–layer modelling software was used to extract film thicknesses, after calibration of the system using a SiO_2 layer of known thickness grown on a Si wafer. The instrument itself is set up according to the schematic in figure 3.16. The polariser and analyser are mounted on separate stages and move with symmetric motion. Their movement is controlled by individual stepper motors which orientate themselves to the chosen angle during measurements with an accuracy of $\leq 0.02\,^{\circ}$. Microspot

attachments are placed in front of the two stages in order to focus the beam. The microspot attachment reduces the optical beam diameter to 300 μm; otherwise the beam is a few millimetres in diameter.

Chapter 4

Analytic theory of the linear optical response of aligned ellipsoidal nanoparticles on planar surfaces

> "Mankind is not a circle with a single center but an ellipse with two focal points of which facts are one and ideas the other."
>
> –*Victor Hugo*

Modelling the anisotropic optical response from ellipsoidal islands is challenging, as analytic expressions only exist for NPs which are isotropic in the surface plane [61]. The resonant structure of the NP depends on particle dimensions, the dielectric function of the embedding medium and shape of the NP. The plas-

monic response is further modified by image charge effects when the single NP is supported on a substrate, which in turn modifies the optical response of the system. Additionally, where the NPs are present in arrays on the surface, the local fields are further modified by the direct and image charge multipolar interactions between the NPs.

4.1 Theory and phenomenological model

Local field effects contribute to the splitting of resonances along the crystallographic axes, x, y and z, for anisotropic ellipsoidal islands grown by self-assembly. The basic assumption of the model is that the NP can be regarded as being embedded in the capping layer. With this assumption, Camelio *at al* [67] based on the work by Yamaguchi [122, 123] show that local field effects can be combined as an effective depolarization parameter, F', in the expression for the in-plane and out of plane dielectric response of the NP layer:

$$\epsilon_L = \epsilon_{cap}\left(1 + \frac{NV(\epsilon - \epsilon_{cap})}{\epsilon_{cap} + F'(\epsilon - \epsilon_{cap})}\right) \tag{4.1}$$

$$F' = \frac{\epsilon_0 \epsilon_{cap}^2}{\epsilon - \epsilon_{cap}}\alpha\beta + L(1 + \epsilon_0 \epsilon_{cap}\alpha\beta) \tag{4.2}$$

where N is the number of NPs per unit volume, each NP of volume V, ϵ_{cap} is the capping layer dielectric function, ϵ is the NP dielectric function, L is the NP geometrical depolarisation factor, β is the dipole interaction between neighbouring islands and α is the polarisability per unit volume.

In the course of this chapter, a full analytical treatment of the optical response

has been developed, where the effects of island anisotropy, coupling effects, image charge contribution and effects of capping have been taken into consideration. Once an analytical expression for the NP layer dielectric function has been obtained, a transfer matrix formalism is introduced to compare experiment and theory. The validity of the approach developed herein is verified by comparing the simulation with experiments performed on three different samples. In this approach, only oblate spheroids were considered.

First, the Pb on Si system will be used as an example to discuss the theory of the optical response. The experiments carried out for this work are detailed elsewhere [49], where the measurement of the anisotropic reflectance of Pb islands grown on Si(557)–5×1–Au was measured using a visible/near IR (0.45–5 eV) RAS system. Two large features are seen in the RAS response of these elongated Pb islands: one related to the LSPR along the length of the island at 0.4 eV (the x resonance) and one related to the width of the island at 0.9 eV (the y resonance), approximately. Experiments were also performed on samples which were capped with an amorphous Si (a–Si) layer, in order in investigate the effect of capping on the theoretical plasmonic response. The experimental data for both uncapped and capped samples are shown in Figures 4.1 and 4.2. SEM studies of the Pb islands indicated the dimensions of the islands to be 250 nm in length, 65 nm in width and 12 nm in height, with an island number density of 3×10^{13} m^{-2}. The same model will then be applied to other systems: Ag on Al_2O_3 and Ag on Si(001).

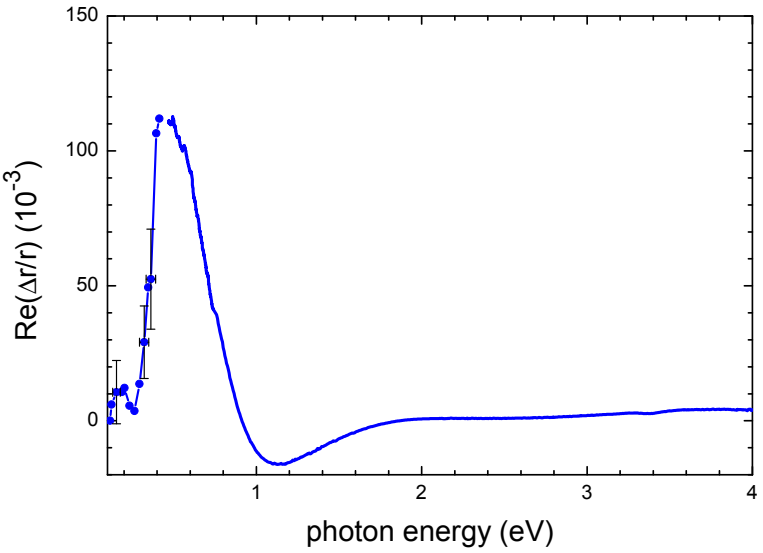

Figure 4.1: Experimental RAS data from uncapped Pb islands on Si(557)–Au. The solid line was recorded using the PEM RAS system, while the points (with straight line segments and representative error bars) were recorded with the rotating sample RAS assembly. Resonances occur at 0.4 eV and 1.125 eV.

4.1.1 Dielectric function of the NP material

The simplest way to describe the dielectric function of the metal is using the Drude–Sommerfield model (Equation 4.3), where a material is approximated to a simple harmonic oscillator of mass m and charge e. An external driving field, E displaces the charge from its equilibirium position resulting in,

$$\epsilon_{Drude}(\omega) = 1 - \frac{\omega_p^2}{\omega(\omega + i\gamma_b)} \tag{4.3}$$

where γ_b is the bulk scattering rate and ω_p is the plasma frequency of the metal given by

$$\omega_p = \left(\frac{ne^2}{\epsilon_0 m^*}\right)^2 \tag{4.4}$$

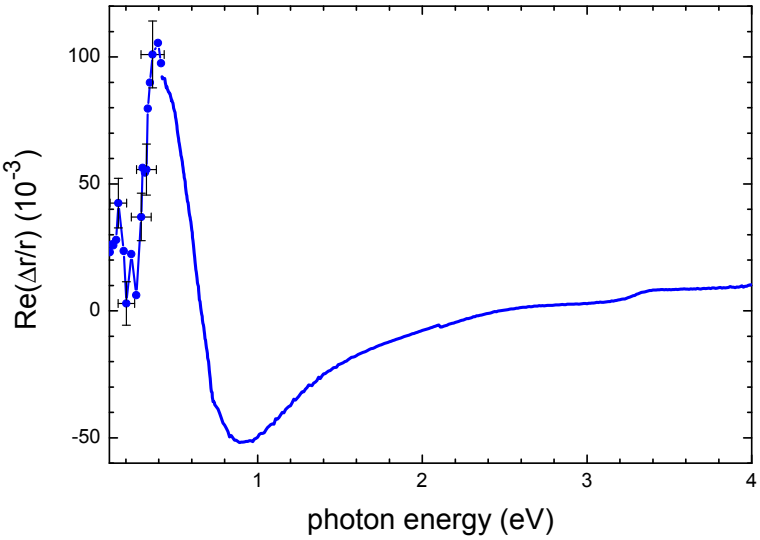

Figure 4.2: Experimental RAS data from capped Pb islands on Si(557)–Au. The solid line was recorded using the PEM RAS system, while the points (with straight line segments and representative error bars) were recorded with the rotating sample RAS assembly. Resonances occur at 0.425 eV and 0.9 eV.

Although the Drude–Sommerfeld model gives accurate results for the optical properties of metals in the IR, it fails to account for the response by bound electrons in the visible region. This effect can be represented by an additional constant contribution ϵ_b^m. Finally interband transitions needs to be taken into account, which are usually found at higher energies outside the plasmonic resonances. The modified Drude model, modified in the direction j, assumes the NP dimensions are shorter than the electron inelastic scattering mean free path in the bulk metal and accounts for size dependent scattering rates from NP bounderies:

$$\epsilon_j(\omega) = \epsilon_b^m(\omega) + \frac{\omega_p^2}{\omega(\omega + i\gamma_b)} - \frac{\omega_p^2}{\omega(\omega + i\gamma_j)} \tag{4.5}$$

Table 4.1: Material parameters for bulk Ag and Pb, after [128, 129]

	ω_p	γ_b	v_f
Ag	8.85 eV	0.037 eV	1.4×10^6 ms^{-1}
Pb	8.65 eV	0.20 eV	2.96×10^6 ms^{-1}

ϵ_b^m is the experimental bulk metal dielectric function. Equation 4.5 arises from taking the experimental bulk dielectric function, which includes inter–band transitions, removing the bulk free–electron-like response and replacing it with a modified free–electron–like response appropriate to NPs. The RAS response from ellipsoidal isalnds can be modelled by assuming different scattering rates in the x and y directions in the surface plane. As the metal NP is reduced in size below the bulk scattering length, the scattering rate increases as electrons are scattered from the NP surface. The modified scattering rate is be defined as:

$$\gamma_j = \gamma_b + \frac{Av_f}{R_j} \tag{4.6}$$

where v_f is the Fermi velocity of the conduction electrons assumed not to be size dependent, R_j, is the semi-axis of the ellipsoid and A has been treated as a fitting parameter close to unity, but varying between 0.2 and 2 [124–126]. A detailed treatment of this is dicussed in [127], where an isolated NP term and an interface term are identified, and it is shown that the perpendicular interface term can be neglected. A value of $A^{interface}$=0.4 is used for the model. The increase in the scattering rate leads to homogeneous broadening of the plasmon resonance of a single NP. The material parameters for Pb and Ag are shown in Table 4.1.

$$A = A^{size} + A_{||}^{interface} \tag{4.7}$$

4.1.2 Isolated NP and local field effects

Neglecting the influence of the supporting substrate and interparticle interaction, the placement of a NP in a dielectric environment experiences a modified field due to local field it experiences which differs from the external applied field, E_{ext}. The induced dipole moment p is related to E_{ext} by

$$p = \epsilon_m \epsilon_0 \alpha E_{ext} \tag{4.8}$$

where ϵ_0 is the vacuum permittivity, and α is the anisotropic polarizability tensor of the NP in a direction j written as,

$$\alpha_j = \frac{\pi abc}{6} \frac{\epsilon_j - \epsilon_{cap}}{\epsilon_{cap} + L_j(\epsilon_j - \epsilon_{cap})} \tag{4.9}$$

where a, b and c are the axis of the ellipsoid and ϵ_{cap} and ϵ_j is the dielectric function of the embedding medium and of the metal NP respectively. L_j is the depolarization factor for an isolated ellipsoidal NP, which accounts for the curvature of the islands defined as,

$$L_j = \frac{lwd}{2} \int_0^\infty \frac{dq}{(l^2+q)\sqrt{(l^2+q)(w^2+q)(d^2+q)}} \tag{4.10}$$

where l, w and d are the semi–axis of the islands in each direction, $\sum L_j$=1. The relative sizes of the axes are relavent here and were upscaled in order to ease numerical integration. Also, the presence of a surface or interface, will cause the sum rule to break down and the depolarisation factors sum to less than unity [122, 123].

4.1.2.1 Size effects

Electrons can scatter with the NP surface randomly, resulting in a loss of coherence of the plasmon oscillation. The smaller the particles, the faster the electrons reach the surface, as a consequence the plasmon band broadens. For larger nanoparticles plasmon peak energies also experience a red–shift with with increasing sizes, due to retardation effects. The effect of changing island length on the RAS signal is shown in Figure 4.3. The width and height of the island was held constant at 65 nm and 12 nm respectively. The maximum shifts to the IR as the island gets longer and also sharpens as a result of a lower scattering rate along the length of the island.

Figure 4.4 shows the effect of increasing the width of the island on the RAS spectrum, with the island length and height kept constant at 250 nm and 12 nm respectively. As the width increases the minimum shifts towards the IR and sharpens as a result of the reduction the scattering rate across the island.

4.1.2.2 Capping effects

The dielectric constant of the medium surrounding the NP plays an important role in determination of the plasmon peak position and intensity. In terms of realising the potential applications of these nanostructures, the NP needs to be protected from corrosion and contamination by the environment, while maintaining the desired electronic and optical properties. The structures are capped for this reason, however, the response may be modified significantly by capping due to the high surface to volume ratio of the NPs. There has been little study of the effect of capping on nanostructures, due to the difficulty that conventional surface

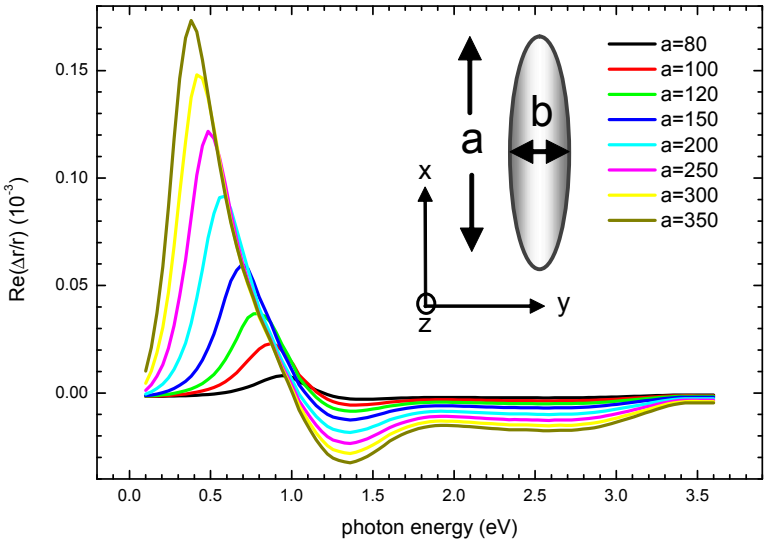

Figure 4.3: RAS spectra showing the effect of changing the island length, a, while keeping the island width and height fixed at 65 nm and 12 nm respectively. The x resonance increases and sharpens, due to a decreased scattering rate. There is also a red–shift of the maximum.

techniques have in probing buried interface structure, but surface and interface optical techniques ('epioptics') offer unique advantages in this area [2]. The in-plane anisotropy can be easily probed using Reflection anisotropy spectroscopy (RAS), and has been used successfully for probing capped structures [21]. For the plasmonic structures described within this chapter, the inclusion of the dielectric function of the capping layer in the model is treated as a simple average of the substrate and the capping layer, since the NP is partially in contact with both substrate and capping layer resulting in,

$$\epsilon_{eff} = 0.5(\epsilon_{sub} + \epsilon_{cap}) \tag{4.11}$$

The effect of capping of an isolated NP is shown in Figure 4.5. The entire structure is shifted towards the IR and a reduction in the minimum is observed. this is

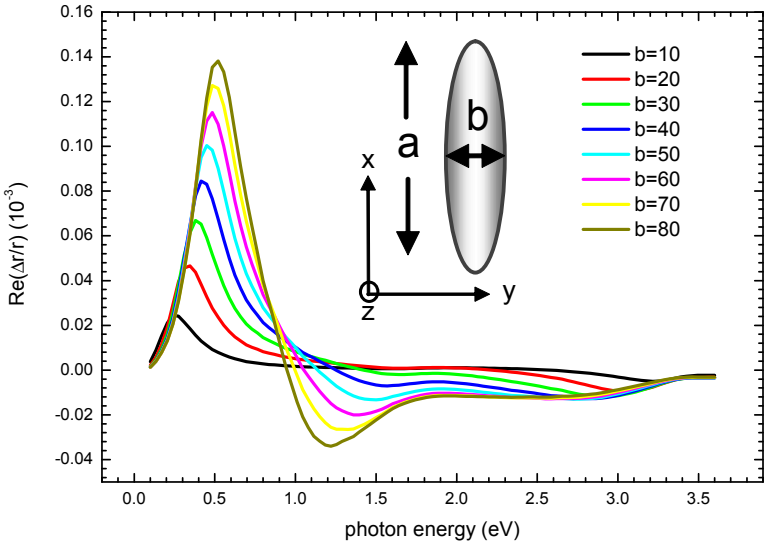

Figure 4.4: RAS spectra showing the effect of changing the island width, while keeping the length and height fixed at 250 nm and 12 nm respectively. As the width increases the minimum shifts towards the IR and sharpens due to the reduced scattering rate in the direction across the island.

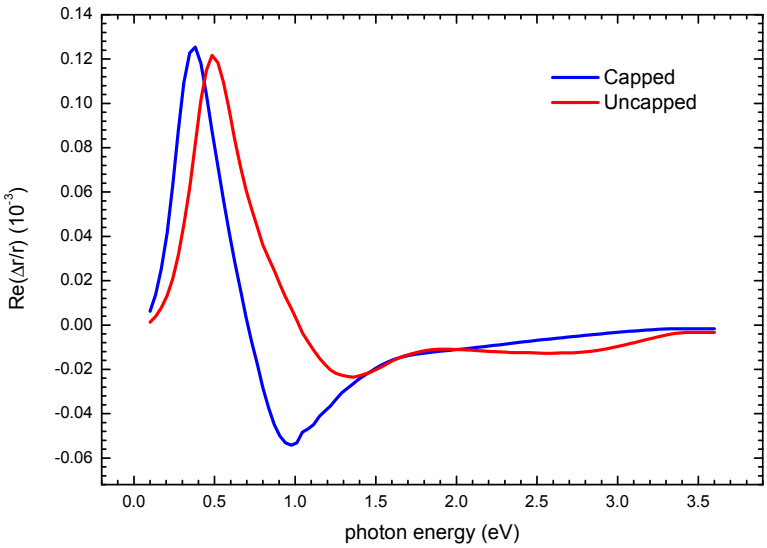

Figure 4.5: RAS spectra showing the effect of capping the nanostructures with a–Si. The entire structure is shifted towards the red.

consistent with embedding the island in a material of higher refractive index than the ambient.

4.1.3 Coupling effects

So far we have discussed the optical response of an isolated NP. However, the systems dealt with here consist of an aligned array of islands on a substrate, these local field effects can be dealt with by introducing dipole–dipole interactions as a result of neighbouring islands, and image charge contributions due to the interaction with the substrate. The dipolar interaction β, with other NPs in the array and including the self–image effect is given by [67]:

$$\beta = -\frac{V}{4\pi\epsilon_0\epsilon_{cap}}\left(\sum_i \frac{3\cos^2\theta_i - 1}{r_i^3} + F\frac{1}{(2d)^3} + F\sum_i \frac{3\cos^2\theta_i' - 1}{r_i'^3}\right) \tag{4.12}$$

and

$$F = \frac{\epsilon_b - \epsilon_{cap}}{\epsilon_b + \epsilon_{cap}} \tag{4.13}$$

where ϵ_0 is the permittivity of free space, ϵ_b is the bulk dielectric function of the substrate, θ_i is the dipole angle, r_i is the separation of the point dipole from the central particle, θ_i' is the image dipole angle and r_i' is the separation of the image point dipole from the central particle, with the centre of the particle a distance d from the interface in the z–direction. The first term describes the point dipole interaction of the central NP with the array of other NPs, the second is the self–image dipolar interaction of the NP, whose centre is d above the interface, and the third term is the dipole interaction of the central NP with the array of image charges of other NPs. Figure 4.6 shows the effect of bringing the islands closer

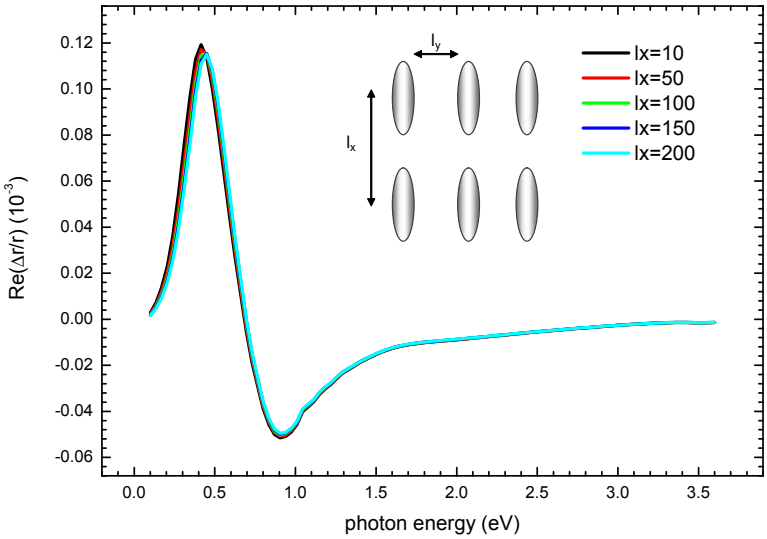

Figure 4.6: RAS showing the effect of including the dipole–dipole interaction from neighbouring islands. The islands are brought closer in the direction along the islands.

together in the direction along the islands. The RAS response remains mostly unaffected with increasing l_x, with a slight shift towards the red. Similarly Figure 4.7 shows the effect of changing the distance in the direction perpendicular to the islands, which has a significant effect on the plasmonic response. When the distance l_y is below a 20 nm, the NP dielectric function in x and y are comparable, thus reducing the size of the plasmonic response.

Finally an interaction with the substrate must be included in the model. The pre–factor F in Equation 4.12 accounts for the strength of the image charge effect: if the particle is embedded in a single medium, there is no image charge and F goes to zero. We use a NP corrected centre at a distance d, above the interface following [123, 130]. The standard spherical approach using d=$c/2$, is commonly used, where c is the height of the island in the z direction, however this is known to overestimate the interaction with the substrate, and thus red–shift

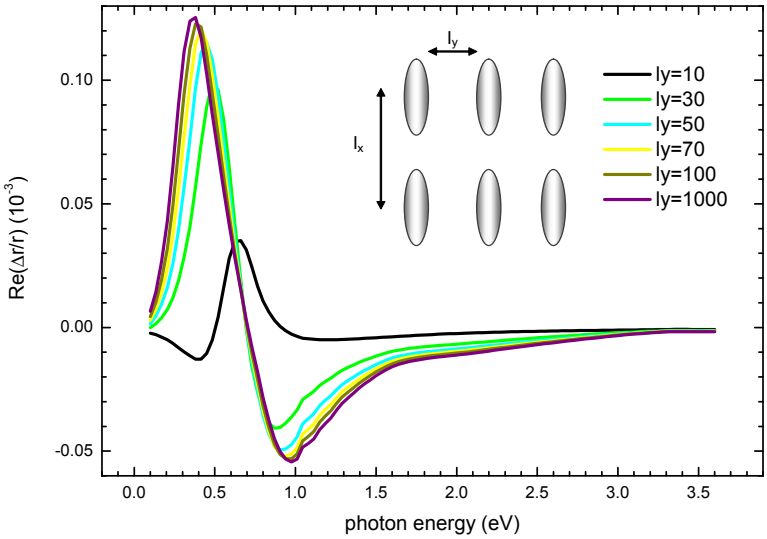

Figure 4.7: RAS spectra showing the effect of including dipole–dipole interactions from neighbouring islands. The effect is investigated by bring the islands closer together in the direction across the islands, while maintaining the separation along the island constant at 50 nm.

the response too much [130]. Figure 4.8 shows the resulting RAS spectra with an image charge effect included, for the uncapped and capped islands. An image charge effect is more significant in the case where the islands are uncapped, as the structure is red–shifted and increasing the intensity of the resonances. However, for the capped case the structure remains entirely unchanged when an image charge correction is included, this is explained by considering that the dielectric function of crystalline Si and a–Si are quite similar in the region of the resonances that results in $F \approx 0$.

4.1.4 Retardation effects

The quasi–static approximation discusses how the incident radiation may be considered as uniform within the volume of the NP. This can be sufficient for parti-

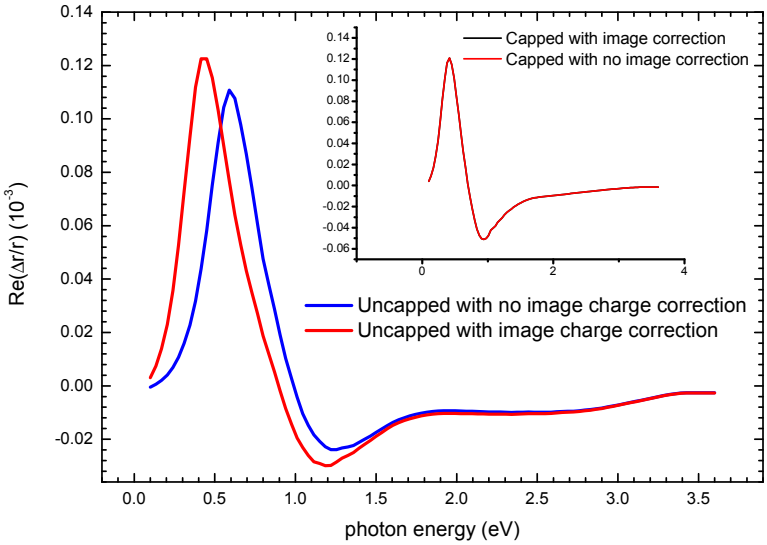

Figure 4.8: RAS spectra showing the effect of including an image charge correction for the uncapped and the capped structures. In the uncapped case the correction is significant as the strength of the image charge is strong. Inset: shows the effect of including the image charge correction for the capped sample.

cles up to a size of 100 nm. Given the size of the Pb islands, retardation effects must be taken into account in order to predict the dependence of the optical response on NP dimensions. Moroz [131] discusses this for spheroidal NPs with a volume equivalent to a sphere of radius 5–50 nm and summarizes the modified long wavelength approximation (MLWA), which is applied as a correction to the depolarization factor as:

$$L_{MLWA} = L_j - \frac{1}{3}(ka)^2 - i\frac{2}{9}(ka)^3 \tag{4.14}$$

where $x = ka$, for a sphere of radius a, and the wavevector $k = (2\pi/\lambda)\sqrt{\epsilon_{eff}}$ for the NP layer. When $ka \geq 1$, unphysical results are given. Also when adapting this to elongated islands the depolarisation factors can be as low as 0.02 along

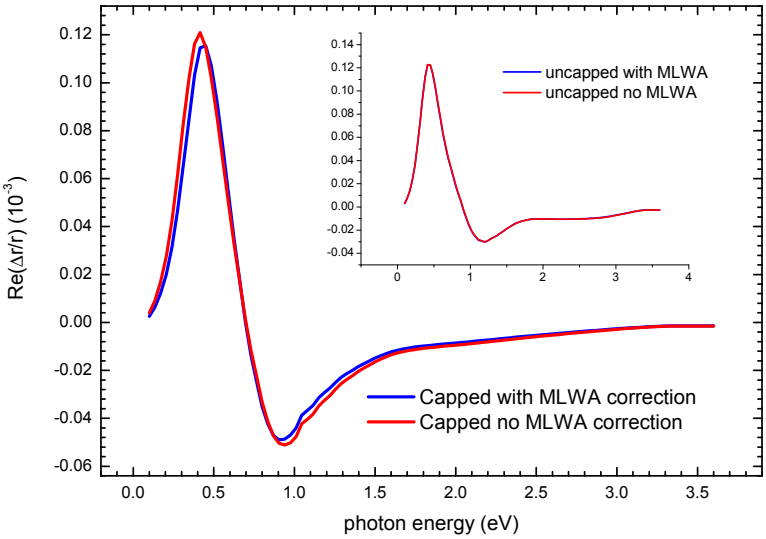

Figure 4.9: RAS spectra showing the effect of including the MLWA correction both the uncapped and capped samples.

the island. Maier *et al* [132] used $x = k(abc/8)^{1/3}$. This keeps the parameter to a maximum of ∼0.3. The correction using the adapted spherical expression becomes,

$$L_{MLWA} = L_j - \frac{1}{4\pi}\left[\frac{k^2}{3}\left(\frac{3V}{4\pi}\right)^{\frac{2}{3}} - i\frac{k^3V}{6\pi}\right] \tag{4.15}$$

Figure 4.9 shows the effect of adding the MLWA correction to the model for the capped and uncapped case. The x component requires a significant correction due to is long dimension, but this correction becomes significant after 1 eV. The x resonance is at 0.5 eV, so no effect is seen. Even at ∼3 eV, where the correction is large, the plasmon response is negligible. This correction has to be included in general because resonances in other materials, with different dimensions, may occur at higher energies.

4.1.5 Solving the T–matrix

We have implemented the T–matrix approach of Schubert *et al* [133, 134]. The system is modelled as a multiple layered system with plane parallel interfaces in order to calulate the RAS, and data are more easily compared to theory. An incident light wave with wave vector k_a coming from the incident medium at an angle of incidence ϕ_a, then k_a and k'_a is the reflected wave from the plane of incidence. T is defined by relating the field amplitudes inside the ambient medium to those inside the exit medium. A general transfer matrix can be defined for any layered structure:

$$\begin{pmatrix} A_s \\ B_s \\ A_p \\ B_p \end{pmatrix} = \mathbf{T} \begin{pmatrix} C_s \\ D_s \\ C_p \\ D_p \end{pmatrix} = \begin{pmatrix} T_{11} & T_{12} & T_{13} & T_{14} \\ T_{21} & T_{22} & T_{23} & T_{24} \\ T_{31} & T_{32} & T_{33} & T_{34} \\ T_{41} & T_{42} & T_{43} & T_{44} \end{pmatrix} \begin{pmatrix} C_s \\ 0 \\ C_p \\ 0 \end{pmatrix} \tag{4.16}$$

where A_p, A_s and B_p, B_s denote complex amplitudes of the p and s modes of the incident and reflected waves, respectively. The exit medium does not include a back side and hence, only two amplitudes for the transmitted p and s modes, C_p and C_s, respectively (back traveling waves not permitted, D_p and D_s=0). The 4×4 matrix describes the propagation of monochromatic plane waves through the entire layered system. The general transfer matrix T is most easily obtained from the product of all inverted matrices T_{ip} for each layer, as well as the incident and exit matrices in order of their appearance.

$$T = L_a^{-1} \prod_{i=1}^{N} [T_{ip}(d_i)]^{-1} L_f = L_a^{-1} \prod_{i=1}^{N} T_{ip}(-d_i) L_f \tag{4.17}$$

where L_a and L_f are incident and exit matrices, respectively. They project the incident and the reflected wave amplitudes through the surface and the transmitted amplitudes through to the exit medium. Once the transfer matrix is found, it is related to the complex reflection coefficients,

$$R_{pp} = \frac{T_{11}T_{43} - T_{41}T_{13}}{T_{21}T_{33} - T_{23}T_{31}} \tag{4.18}$$

$$R_{ps} = \frac{T_{11}T_{23} - T_{21}T_{13}}{T_{11}T_{43} - T_{41}T_{13}} \tag{4.19}$$

$$R_{sp} = \frac{T_{41}T_{33} - T_{43}T_{31}}{T_{21}T_{33} - T_{23}T_{31}} \tag{4.20}$$

4.2 Pb on Si(557)–Au

Figure 4.10 and 4.11 show the output of the model for this system with all local field effects included. The model produces reasonanble results, especially in terms of the capped Pb sample. However, in the case of the uncapped the model fails to predict the correct intensity of the resonance across the island.

4.2.1 Ag on Al_2O_3

The next system used for testing this model is the Ag on Al_2O_3 system, where Ag islands can be deposited on facetted sapphire at a glancing angle to create aligned ellipsoidal arrays with strong plasmonic resonances. This details of this work has been published by Verre *et al* [22, 64]. The dimensions of the NPs were studied using SEM and TEM, and were found to have a=18 nm, b=15 nm and c=12 nm, where a, b and c are length, width and depth of the island respectively. The island density was found to be 3.5×10^{14} m^{-2}, approximately. SE was used

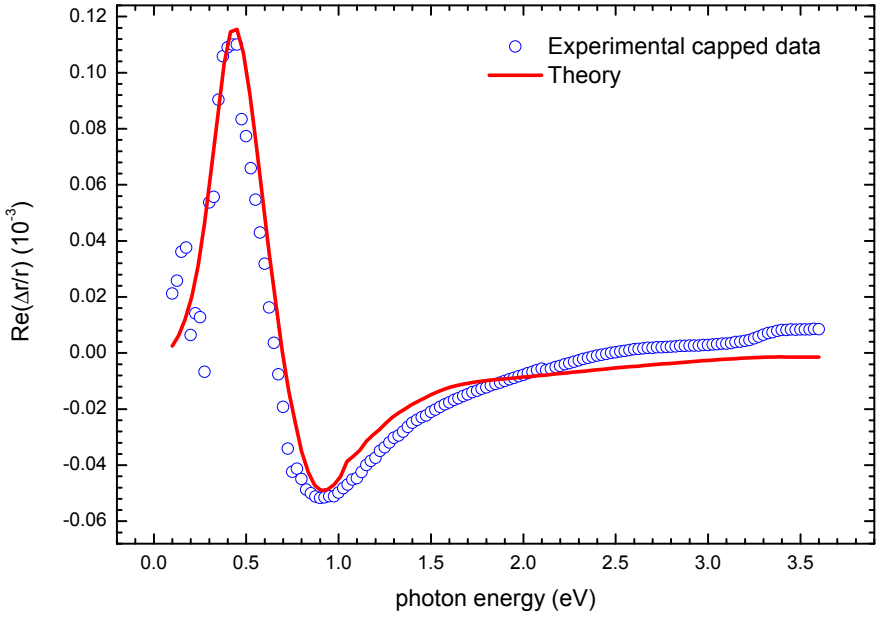

Figure 4.10: Modelled RAS response of capped Pb islands compared with experimental results.

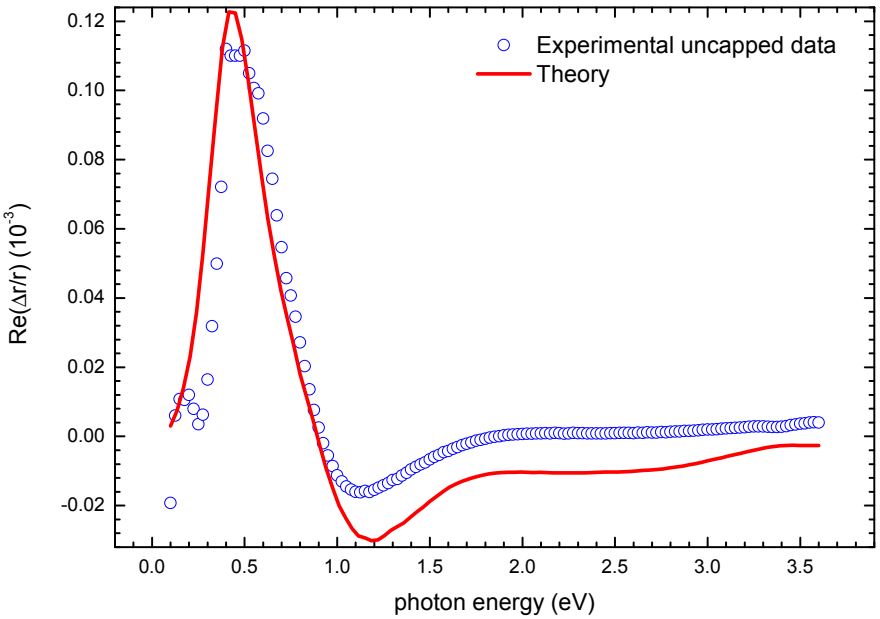

Figure 4.11: Modelled RAS response of uncapped Pb islands compared with experimental results.

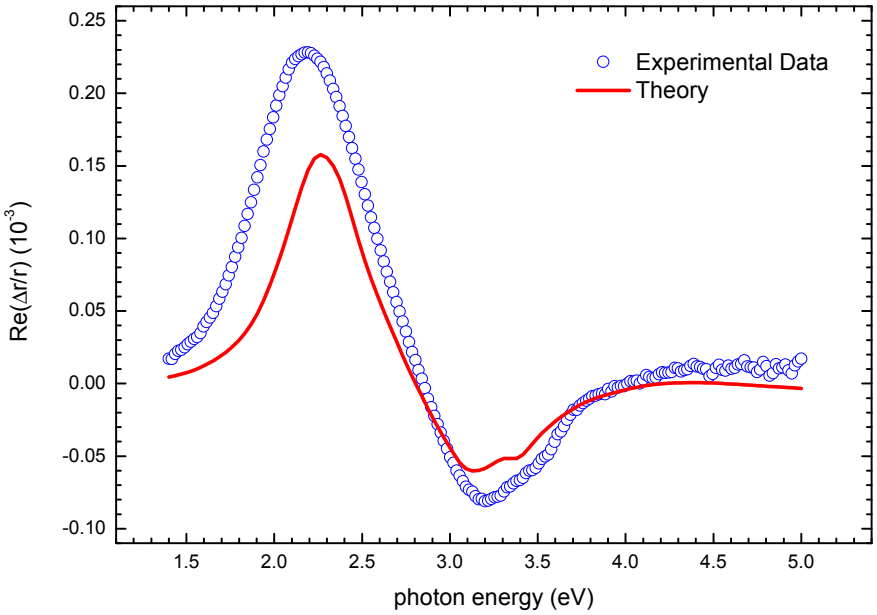

Figure 4.12: Al2O3

to find the pseudo–dielectric function parallel and perpendicular to the islands. The model could then be modified to calculate SE data and then used to fit the experimental pseudo–dielectric function. This serves as a more stringent test of the model, as SE is performed off–normal incidence and probes the out–of–plane response from the z–resonance of the NP, which is not measurable with RAS.

Figure 4.12 shows the RAS response of these small Ag islands deposited on facetted sapphire, where the peaks are associated with plasmonic absorption of the NP layer. The x resonance appears at 2.19 eV while the y resonance is at 3.2 eV. Given the small dimensions of the islands compared to the Pb, the quasi–static approximation still holds. The Schubert approach was used to calculate ellipsometric data by changing the angle of incidence to one that was used experimentally, in this case 61°.

The model fails to predict the correct intensity of the plasmonic resonances.

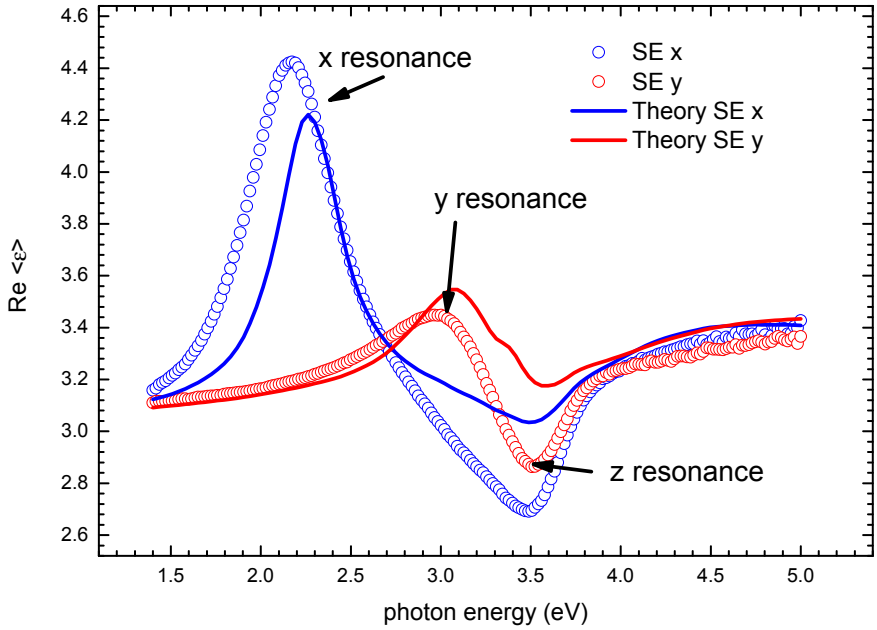

Figure 4.13: Al2O3

however the resonances are correctly estimated, with the x at 2.26 eV and the y resonance at 3.13 eV.

Figure 4.13 and 4.14 shows the fit to the pseudo–dielectric function obtained by SE. The fit to the real part of the dielectric function is reasonable, with the model correctly predicting the presence of x, y and z resonances. The imaginary pseudo–dielectric function is more difficult to simulate due to contributions from the real part. The line–shape is obtained correctly, as well as the position of the resonances.

4.2.2 Ag on rippled Si(001)

Finally the model will be used to model the plasmonic response of Ag on rippled Si templates. Figure 4.15 shows an SEM image of Ag deposited on rippled Si,

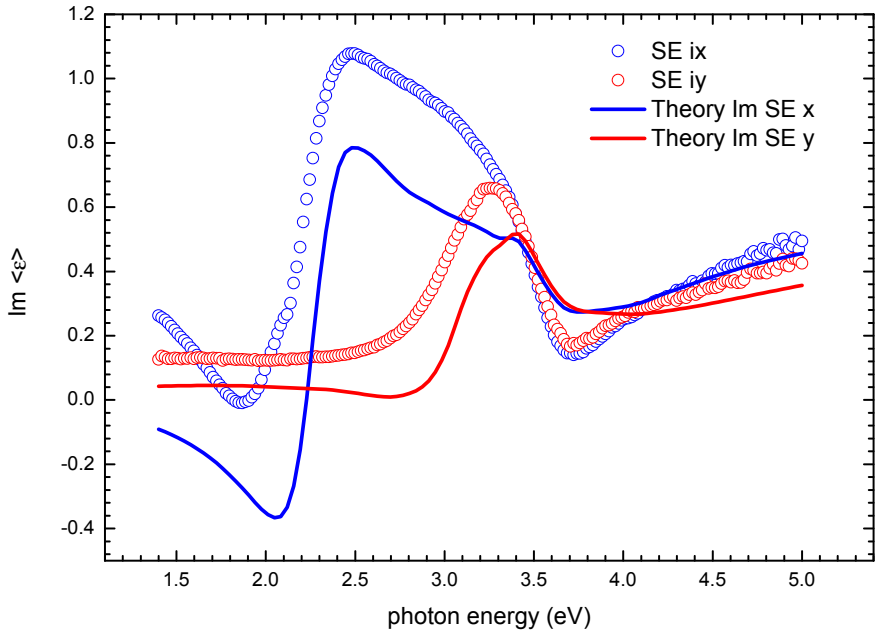

Figure 4.14: Al2O3

named sample UA10. After deposition of Ag, this sample was annealed to 350°, consequently this will produce morecentrosymmetric NPs. Analysis of SEM images the value of a was set to 18 nm, b to 14 nm, and c was varied within the model. The experimental RAS spectra of is shown in Figure 4.16 together with the simulated RAS spectra. The intensity of the peaks is reasonable, however, the simulated RAS is shifted too far into the red by 0.2 eV, approximately. It seems that adjusting the value for c, the height of the NP, will correctly displace the spectra into the blue to match experimental data, however the value then becomes too large to be physical. Figure shows the simulated pseudo–dielectric function of the same sample (needs to be inserted).

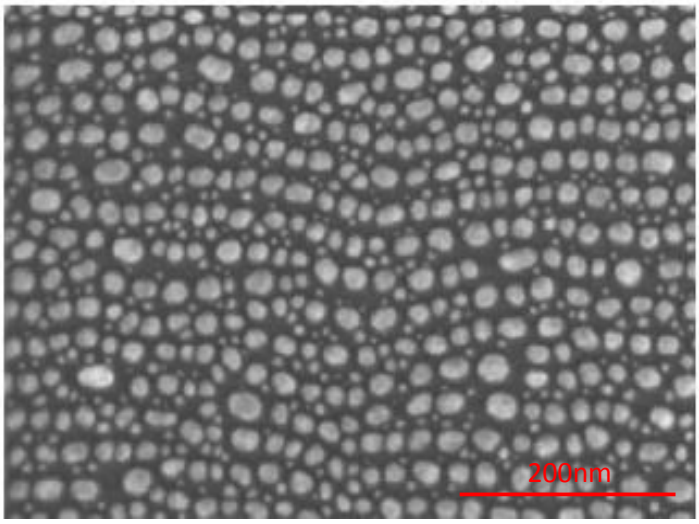

Figure 4.15: SEM of Ag deposited on rippled Si.

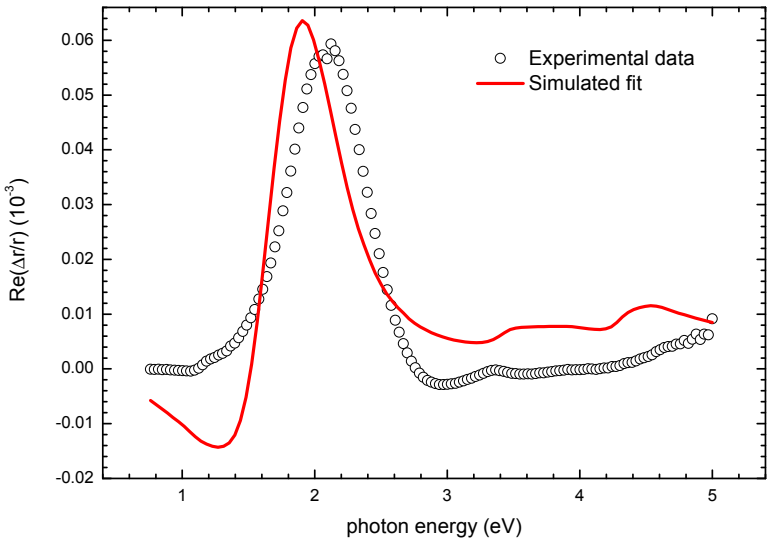

Figure 4.16: Simulated RAS spectra of Ag on rippled substrate (sample UA10).

4.3 Conclusions

The analytical model presented here has shown reasonable success in determining the optical response on various substrates, metals and NP densities. Despite the detailed approach, the model often fall short in predicting the pseudo–dielectric functions the the NP layer, emphasising the complexity of modelling these systems. Theoretical calculations are a possible in order to predict their behaviour, however, typically $\sim 10^5$ points are required, making it computationally expensive.

The Pb on Au system was mostly successful, as resonance position were correctly predicted for both capped and uncapped samples, and the RAS intensity was correctly estimated for the capped case. The uncapped sample showed some deviation from experimental spectra and the model was unable to predict the RAS intensity in the y resonance.

The Ag on Al_2O_3 system was also successful in determing the RAS response, although when determining the pseudo–dielectric functions some departure from experiment was observed.

The Ag on rippled Si samples were the most challenging, as can be seen from SEM images, the NP sizes are not consistent and the preparation technique of the samples implies the surface may be straightforward and may contain contributions from tarnished Ag, especially in the capped samples. A 5–phase model including the dielectric function at the interface may be able to properly account for these effects.

Chapter 5

Linear and nonlinear characterisation of plasmonic nanostructures on rippled Si templates

This chapter will discuss the optical response of rippled Si templates for the purpose of the fabrication of plasmonic nanostructures, and contains work published in *physica status solidi* 2012, [135]. Epioptic techniques will be used to monitor the formation of these ripples *in situ*. The optical response of Ag islands deposited on the rippled templates will then be discussed, with a view to being able to characterise them using linear and nonlinear optical techniques.

5.1 Rippled Si templates

Irradiation of a surface with high energy ions leads to the removal of surface atoms. This process of ion erosion or sputtering is often used as a method of surface modification by industry in order to roughen, smoothen, or clean surfaces. Navez *et al* [136], showed that that this technique could be used to create self–organised periodic patterns on glass surfaces, and since then patterns have been produced on a whole variety of materials such as metals [137], semiconductors [138, 139], and insulators [140]. Periodicity of the ripples can be adjusted by varying energy of the ions and can range from 10 nm up to a few μm. Depending on the angle of incidence, the ripples can be orientated either parallel or perpendicular to the direction of the ion beam.

Native–oxide–covered rippled nanostructures on Si(001) were grown at the Helmholtz–Zentrum Dresden–Rossendorf using a procedure that has been described in [69]. The rippled structures had nanoscale periodicity ranging from $\sim$20 to $\sim$50 nm and an amplitude of $\sim$0.8 to $\sim$1.5 nm as measured by AFM. The templates were prepared by irradiating native–oxide–covered Si(001) substrates at room temperature with a collimated beam of 500 eV Ar^+ ions, aligned with the $\langle 100 \rangle$ azimuth and at an angle of incidence of 67° with respect to the surface normal. Fluences in the range $\sim 10^{16}$ to $\sim 10^{19}$ ions cm^{-2} were used.

5.1.1 Ambient measurements

Optical measurements on the rippled templates were performed in ambient conditions. Measurements were repeated after 2 months and were reproducible within experimental error, but initial SHG measurements on some samples, within a

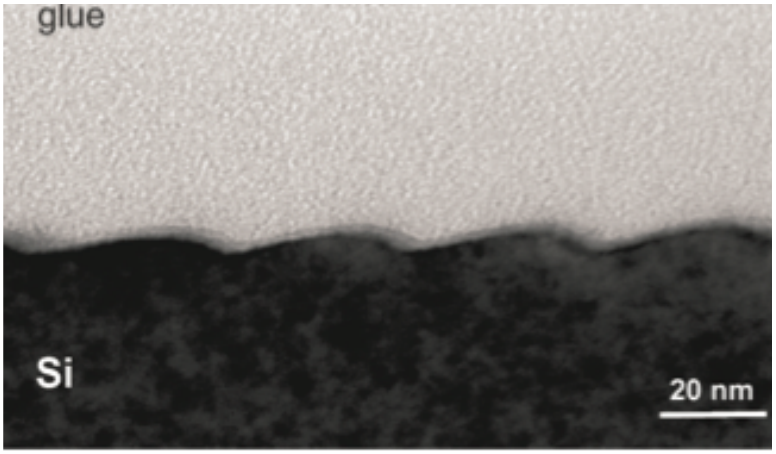

Figure 5.1: Cross–sectional transmission electron microscope (TEM) image of rippled Si(001).

week of exposure to the ambient, showed a variation that may indicate sensitivity to the initial stages of native oxide growth. No significant correlation with the amplitude of the ripples was observed in either the RAS or SHG measurements.

The in–plane anisotropy of the rippled samples was measured using the RAS system, as described in Chapter 3. SHG measurements were made using a femtosecond laser tuned to a wavelength of 800 nm. Unamplified 130 fs Ti:sapphire laser pulses of an average power of 200 mW at the samples were used, at a repitition rate of 76 MHz. A fundamental beam of 800 nm was used of 60 μm in diameter at the sample, at 45 $^\circ$ angle of incidence. A half–wave plate in the input beam was rotated and the p– and s– polarised SH responses were measured as a function of wave plate angle (see Figure 3.11). The diode–pumped laser system is very stable and it was sufficient to normalise the signal using the square of the laser output power.

5.1.1.1 RAS

It is well established that the rippled structure produced by Ar^+ irradiation is defective on the nanoscale, with textured crystalline and amorphous Si regions and with the first few nanometers of surface being amorphised [141, 142]. In addition, X–ray diffraction measurements on similar structures produced by Xe^+ ion irradiation in the 5–35 keV range have shown that the structure is anisotropically strained, with the lattice spacing expanded more along the ripples than across them [113]. Figure 5.1 shows that the ripples are asymmetric in cross–section. The periodicity of the ripples increases with increasing fluence, with the longest periodicities having the largest exposure to the ion beam [69]. Figure 5.2 shows the RAS response of native–oxide–covered rippled Si(001). As mentioned previously, in the absence of ripples, native–oxide–covered Si(001), is optically isotropic with no RAS response [143]. The main effect of the rippled structure is to introduce a broad maximum, centred at ∼2.5 eV and less than 1 RAS unit in amplitude. A smaller broad minimum at ∼3.3 eV is observable at higher fluences, but no correlations could be extracted. With these small RAS amplitudes a discontinuity associated with a grating change in the monochromator can be seen at 2.1 eV. The upper left inset in Figure 5.2 shows the smoothed spectra, and the upper right inset shows the smoothed RAS amplitude at 2.5 eV, plotted as a function of periodicity. In Figures 5.2, 5.5, 5.6 and 5.7 the data points of the insets are colour–coded from the main graphs, allowing the periodicity of each graph to be identified. The right inset in Figure 5.2 shows considerable scatter in the data, but an overall decrease in RAS amplitude with increasing periodicity, and thus ion beam exposure can be seen. A linear regression analysis gives an

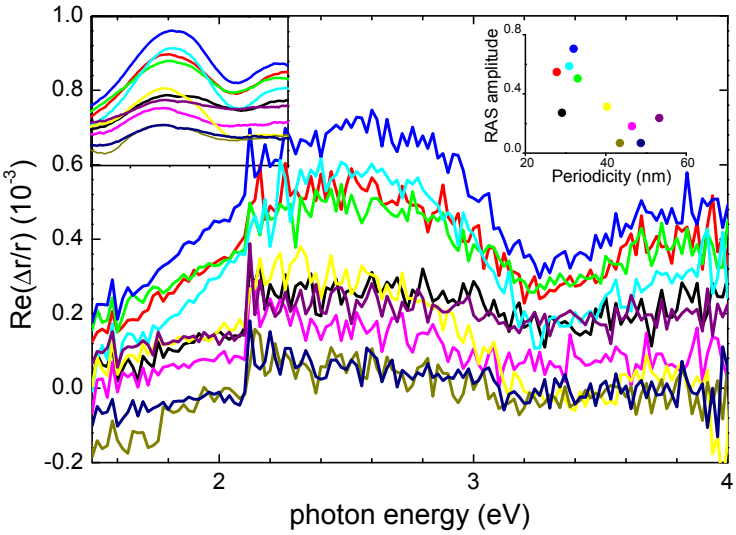

Figure 5.2: RAS response of native–oxide–covered Si(001) with ripples periodicities of ∼30–50 nm. Upper left inset: smoothed curves (20 point adjacent averaging). Upper right inset: plot of RAS amplitude at 2.5 eV versus periodicity.

adjusted R–squared value of 0.50. Small shifts in the position of the maxima can be seen in the smoothed data, but the use of the maxima does not improve the correlation significantly, nor does the use of peak areas rather than amplitudes. *In situ* monitoring of the change of the RAS signal at a fixed spectral energy may be possible, if the RAS system is optimised for this spectral region. It appears likely that sample–to–sample variation contributes to the scatter in the data and it would be interesting to explore whether the recently developed sequential sputtering technique [70], for improving sample quality would reduce this scatter significantly.

RAS has been shown to be sensitive to macroscopic strain, with signals of the order of 1 RAS unit being obtained when external stress is applied to native–oxide–covered Si(001) along the principle crystallographic directions [143]. For

example a sharp derivative–type feature, associated with the crystalline Si E_0' critical point, is observed at 3.4 eV for stress applied along the $\langle 100 \rangle$. The behaviour observed in Figure 5.2 is consistent with strain in textured nanocrystalline and amorphous Si (a–Si) regions. However, the broad maximum at 2.5 eV is more likely to arise from strained a–Si.

5.1.1.2 SHG

As discussed in Section 2.2.1.1, the SH intensity as a function of half–wave–plate angle can be expressed as,

$$I_p^\alpha \propto [A\cos^2\alpha + B\sin^2\alpha + C\sin 2\alpha]^2 \tag{2.23}$$

$$I_s^\alpha \propto [F\cos^2\alpha + G\sin^2\alpha + H\sin 2\alpha]^2 \tag{2.24}$$

where α is the polarisation vector angle with respect to the x axis. The SH response is fitted to Equations 2.23 and 2.24. The tensor components contributing to A, B, C, F, G and H depend on the symmetry of the system, and are a function of the Fresnel coefficients, dipolar second order susceptibility χ_{ijk}, bulk quadrupolar terms and possible third order terms that may arise from electric fields or strain. For a p–polarised output, A corresponds to a pP geometry and B corresponds to an sP geometry, where the letters refer to the input and output polarisations, respectively. For an s–polarised output, F corresponds to pS and G corresponds to sS.

Figure 5.3 shows the geometry of the SHG experiments performed with respect to the direction of the ripples. Placement of the optical plane of incidence across the ripples is defined as x, whereas the placement of the plane of incidence along

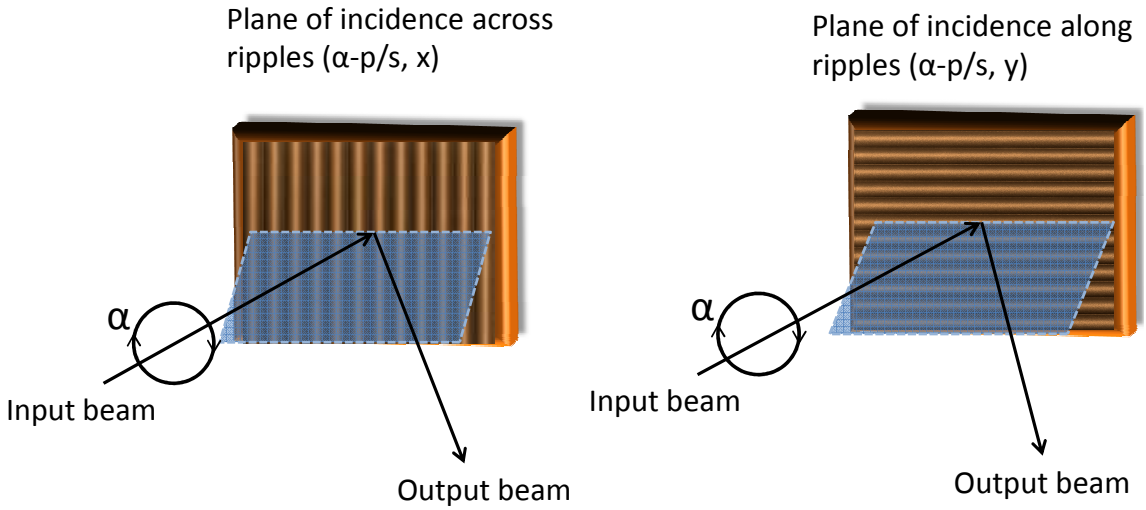

Figure 5.3: Explanation of the geometry of SHG measurements. α-px (or α-sx) measures the SH response across the ripples, while α-py (or α-sy) measures the SH response along the ripples.

the ripples is known as y. α-p and α-s measuremnts were performed on the rippled samples, in both x and y azimuths. Figure 5.4 shows the response from native–oxide–covered Si(001) for p– and s–polarised output. The response is equal in xz and yz planes ($\langle 100 \rangle$ and $\langle 010 \rangle$ azimuths), and the characteristic $\sin^2 2\alpha$ behaviour, shown in the α–s response, is indicative of mirror plane symmetry ($|A|=|B|=0$). It can be seen that the α–s response is an order of magnitude smaller than the α–p response.

Figure 5.5 and 5.6 shows the α–s response from the rippled samples for the xz plane (across the ripples) and the yz plane (along the ripples). Surprisingly, the nanoscale amorphisation, damage and disorder does not reduce the size of the SHG response which, for most of the samples, is larger than the α–s response of the native–oxide–covered Si(001). The mirror plane symmetry is broken, however, with fits to Equation 2.24 showing that B is now significant, with A still negligible. Inspection of Figure 5.6 indicates a larger departure from $\sin^2 2\alpha$ beav-

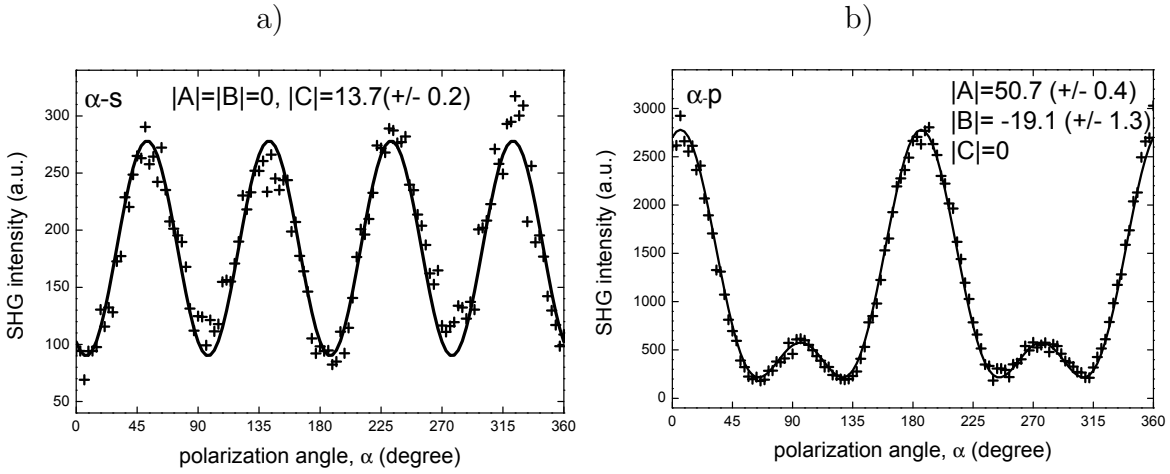

Figure 5.4: SHG response of native–oxide–covered Si(001) for the xz or the yz plane, and fits to Equation 2.23 and 2.24: (a) α–s and (b) α–p.

iour for the yz plane. Using $|B/C|$ as a measure of departure from mirror plane symmetry, which is 0 for Si(001), average values of 0.25(2) for the xz and 0.29(2) for the yz plane were obtained from the fits. Bearing in mind that, for the yz plane of incidence, s–polarised output places the SH field across the ripples, it appears reasonable that the yz response shows a larger departure from mirror plane symmetry. The insets show plots of $|C|$ as a function of periodicity. The small signal size, and the scatter, makes it unlikely that α–s measurements will be useful for the routine characterisation of the ripple structures, except to demonstrate the degree of departure from mirror symmetry.

Figure 5.7 shows the α–p response from the rippled samples in the xz plane, and fit to Equation 2.23, while the inset is a plot of the average of two measurements of A versus periodicity, taken at a 2–month interval, which shows a weak correlation (adjusted R–squared value of 0.48). The response in the yz is similar in shape but showed no correlation. The dominant parameter is A, commonly used p–in/p–out configuration, which gives the largest SHG signal. The value

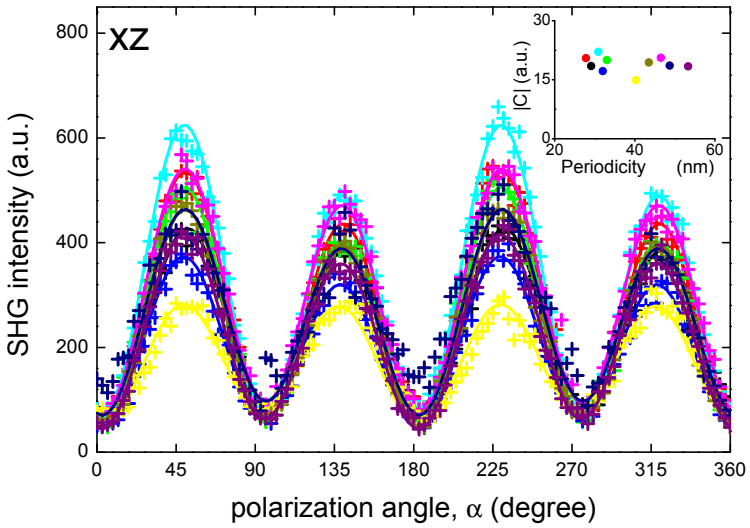

Figure 5.5: The α–s response from rippled samples in the xz plane, and fits to Equation 2.24. Inset:plot of $|C|$ versus periodicity.

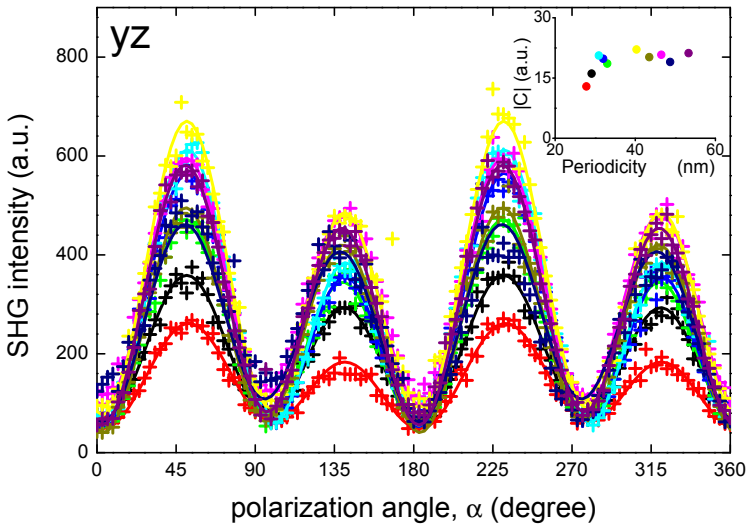

Figure 5.6: The α–s response from rippled samples in the yz plane, and fits to Equation 2.24. Inset:plot of $|C|$ versus periodicity.

of $|C|$ is small, but $|B|$, corresponding to s–in/p–out, is about 0.3 of $|A|$. The overall size of the response in Figure 5.7 is up to four times larger than that of the

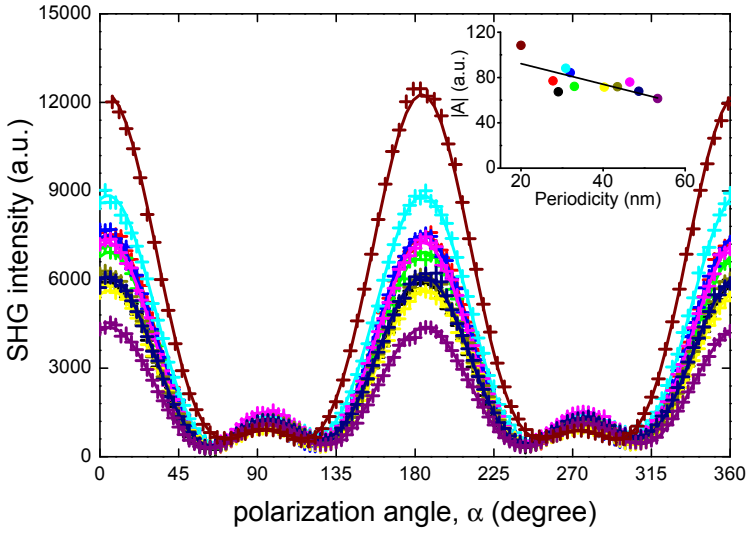

Figure 5.7: The α–p response from rippled samples in the xz plane, with ripple periodicities of ∼20–50 nm, and fits to Equation 2.23. Inset: plot of $|A|$ versus periodicity.

non rippled surface. Monitoring the decrease in the large p–in/p–out SHG signal during ion irradiation may be a possible approach for following the evolution of the rippled structure. The weak correlation with periodicity will be more useful if sequential etching reduces the experimental scatter.

The feasibility of *in situ* monitoring using either technique will, however, depend on the origin of the response. The periodicity of the ripples increases with increasing fluence, with the longest periodicities having the largest exposure to the ion beam [69]. Given the degree of damage and disorder in the near–surface region, it appears unlikely that either the RAS or SHG response is associated with the detail of the local bonding in the near–surface region. In order to test this hypothesis, some samples were etched at 20° to the ⟨100⟩ azimuth in an attempt to create more Si–O bonds but, within experimental scatter, no significant change was observed in the optical response. It is well known that much smaller fluences

will disorder the surface structure and reduce the size of the bond–related dipolar SHG response dramatically [144]. The large response observed here, compared to native–oxide–covered Si(001), points to a different origin. Given that anisotropic strain is known to develop on ripple formation [113], it is more likely that the optical response is associated with such strain and EFISH effects arising from trapped charge at the interface.

SHG is sensitive to strain [34, 145] and to quasi–static electric fields in the near–surface region of crystalline Si [34, 146]. Anisotropic strain will break the mirror plane symmetry, but electric fields normal to tilted interfaces will also do this. The decrease in signal in Figure 5.7 might then indicate some relaxation of the strain and reduction in defect density due to smoothing arising from thermal or ion–induced diffusion, or viscous flow, at high fluences [142]. *In situ* studies of ripple formation under controlled conditions will help elucidate the origin of the optical signals. *In situ* monitoring of the ripple formation using these techniques may not be possible, however, if the optical response turns out to be dominated by strain and electric fields at the interface.

5.1.2 *In situ* measurements

This section will follow the ripple formation on the Si templates in UHV conditions using epioptic techniques. The sample preparation is detailed in Section 3.2.1. The ripples were created by irradiation of the sample surface using high energy Ar^+ ions at 500 eV from an ion gun at an angle of incidence of 70°. The ion flux used in these experiments remained constant at 1×10^{17} $m^{-2}s^{-1}$ and the projection of the ion beam was aligned along the $\langle 100 \rangle$ direction on the substrate.

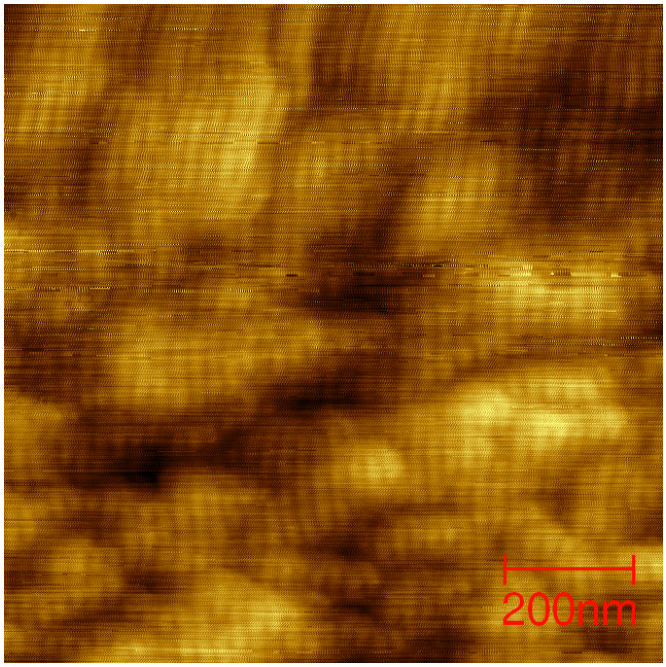

Figure 5.8: AFM of rippled sample grown in UHV, of 17 nm periodicty and 2.9$\mathring{A}$ amplitude.

The process is understood to be cumulative. The sample was irradiated for approximately 16 hours in total making the total fluence in the range of 6×10^{21} m^{-2}. The sample morphology was measured using AFM, and the ripple periodicty was found to be 17 nm $\pm$ 2.5 nm and the amplitude of the ripples was found to be 2.9 $\mathring{A}$ $\pm$ 0.6 $\mathring{A}$. Figure 5.8 shows an AFM image taken of the rippled surface after 16 hours of total irradiation.

RAS was used to monitor the evolution of the ripples in real time, however, due to the geometry of the vacuum system it was not possible to do the same for the SHG measurements, so SHG was recorded on the clean surface prior to the formation of the ripples, and then sequentially every 3–4 hours to monitor the change in the SH response.

5.1.2.1 RAS

Figure 5.9 shows the RAS response of the Si(001) substrate, measured in UHV, with increasing irradiation time. Larger RAS signals are achieved in UHV conditions during ripple growth. Previous studies show that the periodicity of the ripples increases with increasing irradiation, and ambient studies (Figure 5.2) demonstrated that increasing fluence, and hence periodicity, gives rise to a smaller RAS response. However, Figure 5.9 shows an increase in RAS amplitude at 2.5 eV with increasing irradiation. This seems to be the opposite correlation found during measurements in ambient conditions.

However, the periodicity of the sample is smaller than those tested previously, and as discussed in Section 5.1.1.1 RAS is very sensitive to strain, this increase in RAS response may be a strain related response which is stronger during the initial stages of ripple growth. Further experiments monitoring longer ripple formation may be required in order to investigate whether the RAS amplitude begins to decrease for longer periodicities, as was found in Figure 5.2. Figure 5.10 shows the RAS response of the same rippled sample measured in ambient conditions and compared with samples measured in Section 5.1.1.1. The RAS amplitude is consistent with samples of a similar periodicity.

5.1.2.2 SHG

SHG was recorded in incremental periods of 3 hours. Figure 5.11 shows the α–p response from the rippled sample grown under UHV conditions, where the inset shows A plotted agianst the number of irradiated hours (ion fluence). These results show that within the first three hours of irradiation the SHG response

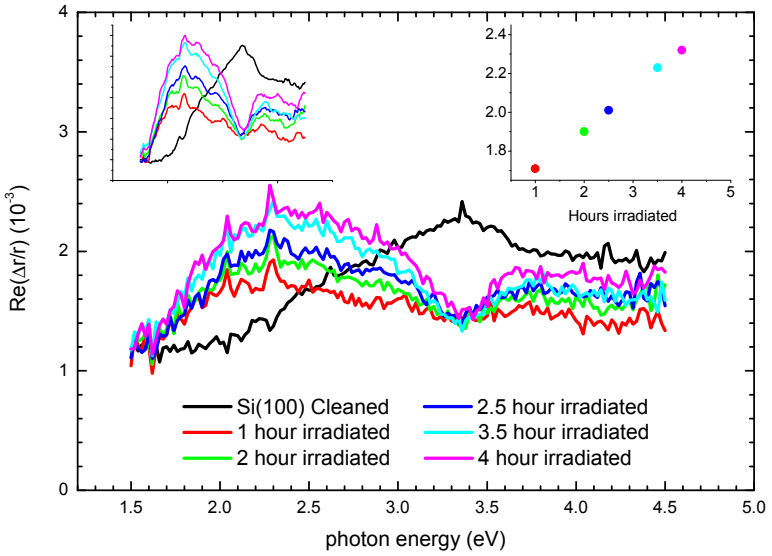

Figure 5.9: RAS response of native–oxide–covered Si(001) with increasing irradiation. Upper left inset: smoothed curves (5 point adjacent averaging). Upper right inset: plot of RAS amplitude at 2.5 eV versus irradiation time.

appears to increase, by approximately a factor of two. After this increase, the response decreases in a similar fashion to the samples measured in ambient conditions.

The initial increase in the SH signal is interesting. Again this may be due to a strain effect during the initial stages of ripple formation, which causes an increased SH response. After the initial stages of growth, some relaxation of strain may occur causing the the SH response to decrease for larger fluences. Further experiments with shorter time intervals between scans may be required to understand at what stage the signal begins to change.

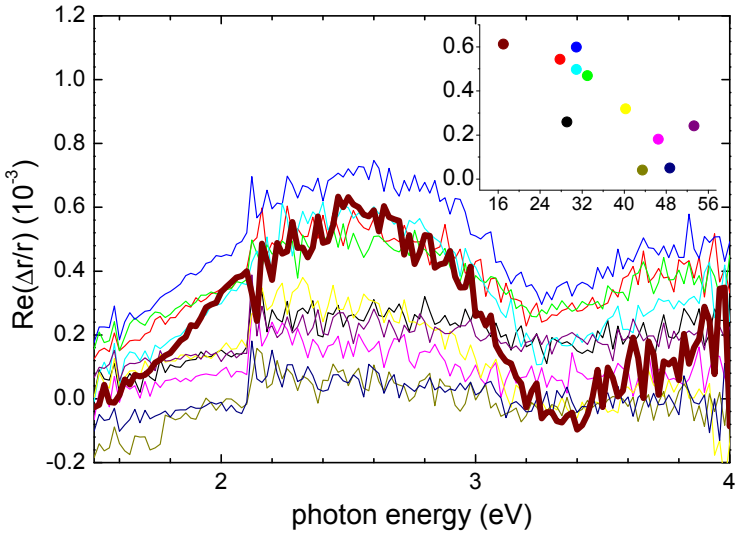

Figure 5.10: RAS response of rippled substrate measured in ambient compared to previously measured samples from Figure 5.2, with sample grown in UHV outlined in bold. Upper right inset: plot of RAS amplitude versus periodicty.

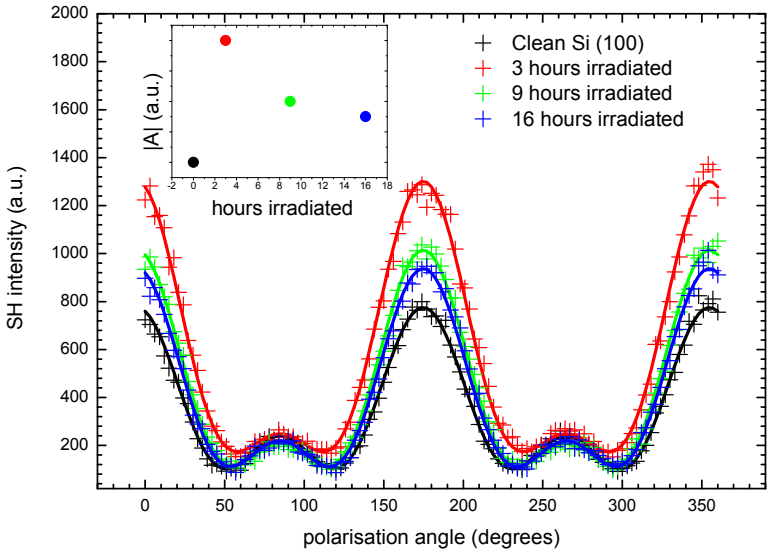

Figure 5.11: The α–p response from UHV grown rippled samples in the xz plane, and fit to Equation 2.23. Upper left inset: plot of $|A|$ versus hours irradiated.

5.2 Plasmonic structures

As discussed in Chapter 1, rippled Si templates are attractive as templates for ultra–thin film deposition as they induce morphological anisotropy and can influence the optical properties of the film significantly. Silver NPs deposited on these rippled surfaces align themselves with respect to the ripple direction, and exhibit plasmon resonances in the visible region [68, 147, 148], which can be monitored and tuned using epioptic techniques. In addition, manufacturing these templates has the advantage of a limitless choice of substrates upon which to experiment, with relatively simple preparation conditions. Figure 5.12 shows a cross–sectional TEM image of silver particles on a rippled Si substrate.

5.2.1 Ag on rippled Si templates

Ag islands deposited on rippled nanostructures on a Si(001) substrate were also grown at the Helmholtz–Zentrum Dresden–Rossendorf using a procedure that has been described in [68]. Samples were separated into various batches including:

- Silver clusters grown on a rippled substrate and capped with a Si layer of ∼20 nm.
- Silver clusters grown on a rippled substrate without a capping layer.
- Silver deposited on a flat substrate with and without a capping layer.

The periodicty of the rippled substrate was constant at 30 nm, and the capping layer was 20 nm. Statistics were carried out on the SEM images of the samples, in order to calculate approximate length and width sizes of the clusters (Table 5.1).

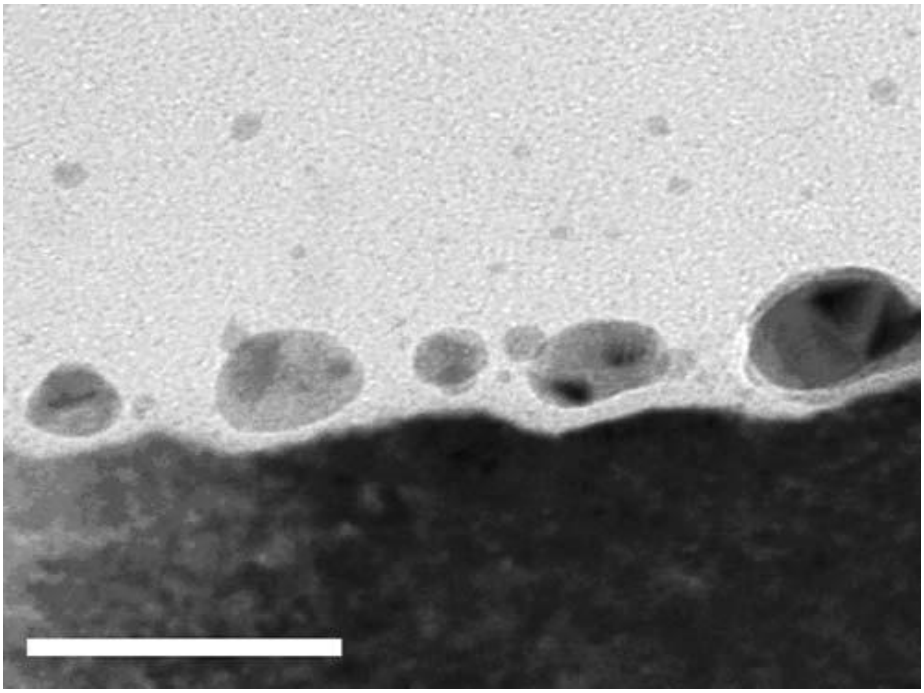

Figure 5.12: Cross–sectional TEM image of silver NPs on a rippled Si substrate with a native–oxide surface layer, from [68]. Larger NPs, are located in the ripple valleys, however, some smaller paricles nucleate on the ripple peaks. The scale bar is 50 nm.

5.2.1.1 RAS

Figure 5.14 shows the RAS response from samples with Ag clusters grown on a rippled substrate and capped with Si. The RAS response increases with increasing aspect ratio of the Ag cluster. Large anisotropies of up to 400 RAS units are observed. The small structure at 2.1 eV is an instrumental artifact arising from a grating change in the monochromator. The method of deposition produces ellipsoidal islands with two resonances: in the x direction along the islands and in the y direction, across the islands (third resonance in the z direction is not accessible by RAS). Only the y resonance is observed in the capped samples, as

Table 5.1: Sample details of capped and uncapped Ag islands on rippled Si. Where the prefix C indicates a capped sample, U indicates uncapped and A and F indicates annealed and flat substrate respectively.

Sample name	Length	Width	Aspect ratio
C1	13.03	9.22	1.41
C3	21.52	14.55	1.48
C4	24.07	15.53	1.55
C5	28.04	16.62	1.68
CA7	13.73	11.60	1.18
CF8	13.83	9.61	1.43
U9	22.49	14.47	1.55
UA10	17.88	13.87	1.28
UF11	13.90	10.54	1.31
U12	29.21	15.67	1.86
U13	32.70	20.42	1.60

the x resonance is further displaced in the IR due to the presence of the capping material. By inspection, an increase in the negative amplitude is associated with a red shift in the spectrum. This is due to a decrease in the scattering rate as the island size increases. Figure 5.15 shows the RAS response of samples with Ag deposited on a rippled substrate without a capping layer. Large anisotropies of up to ∼200 RAS units are observed and again the amplitude increases with increasing aspect ratio of the island. It appears that capping produces an overall shift in the spectrum, which is consistent with embedding the Ag islands in a medium of higher refractive index than the ambient, as now the x resonance is visible.

The RAS response from samples with Ag on flat Si, with and without a capping layer is shown in the inset. Interestingly, a small anistropy is still observed of 10 RAS units approximately. One might expect the RAS response to remain small as the Ag will tend to form more centrosymmetric islands on flat substrates

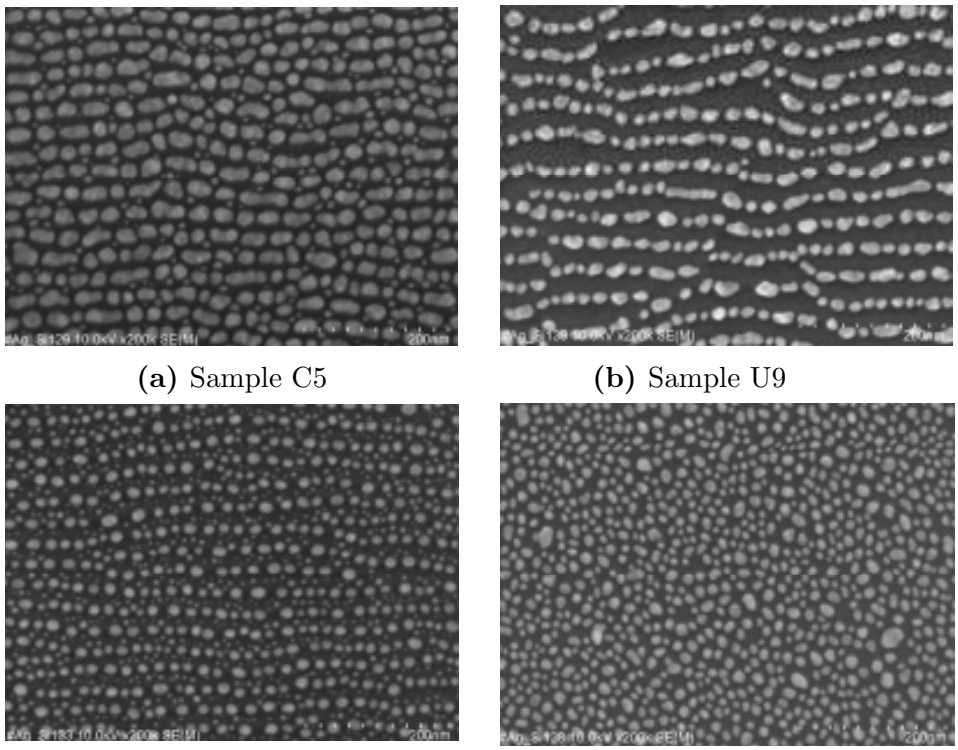

(a) Sample C5 **(b)** Sample U9

(c) Sample CA7 **(d)** Sample UF11

Figure 5.13: SEM images of the various samples investigated (a) capped Ag clusters on a rippled substrate (b) uncapped Ag clusters on a rippled substrate (c) capped Ag clusters on a rippled substrate and annealed (d) uncapped Ag clusters deposited on a flat substrate.

(Figure 5.13d). It is known that Ag islands with only a 10% departure from in–plane isotropy can produce a RAS response of this size, so it appears likely that the deposition method results in some ellipsoidal islands. The effect of capping is clearly shown as the entire spectrum is shifted to the red. Samples like UA10, which have been annealed, are interesting to note as the process of annealing tends to produce more isotropic islands and smaller RAS signals will result.

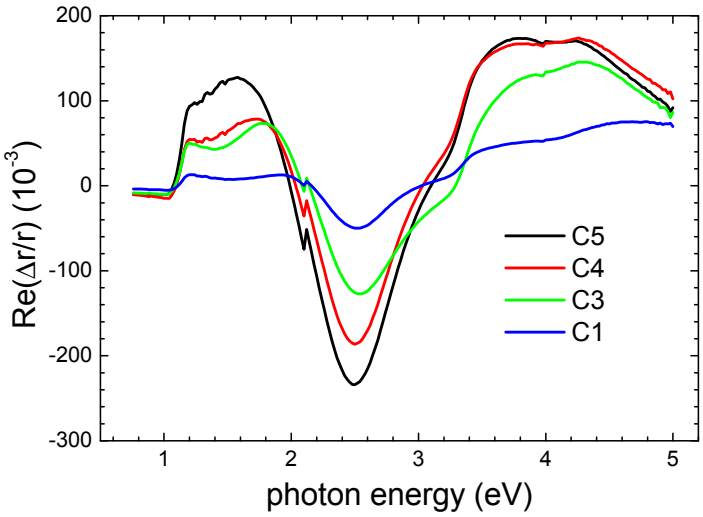

Figure 5.14: RAS response of Ag NPs capped with a–Si on rippled Si. The RAS response increases with increasing aspect ratio.

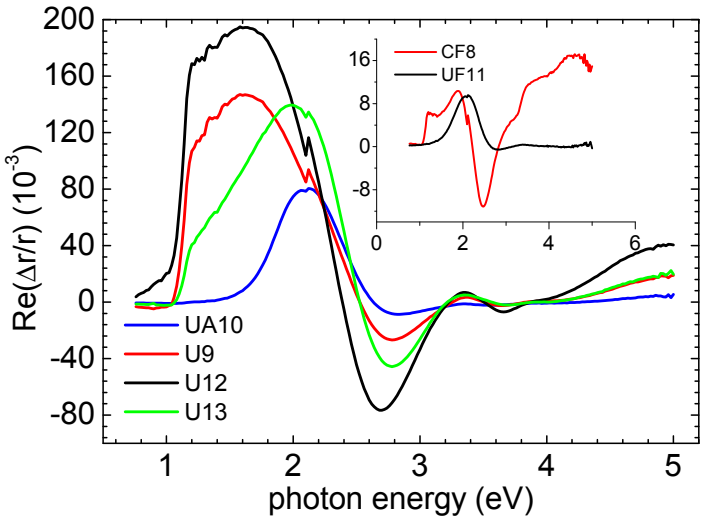

Figure 5.15: RAS response from Ag on rippled Si with no capping layer. The RAS response is greatest for NPs of larger aspect ratios. The overall spectra are blue shifted, compared to the capped samples, since the surrounding medium is of a lower refractive index. Inset: RAS response from Ag on flat Si with and without a capping layer. Again a red–shift is aparent when a cap is introduced since it has a higher refractive index.

5.2.1.2 SHG

Local electric field enhancements can enhance nonlinear processes by many orders of magnitude [149]. These field enhancements, caused by LSPRs, make SHG a viable epioptic technique for characterising these systems, since SHG has intrinsic sensitivity to electric fields at interfaces. This section discusses the nonlinear optical response of aligned NPs arrays. The use of SHG on plasmonic systems has been reported previously [77], however, this is usually performed spectroscopically with a view to tuning the plasmonic response as opposed to providing information on symmetry and morphology of the system. Polarisation dependent SHG can give an insight into the symmetry of these aligned NP arrays. The input polarisation angle, α, is rotated using a half–wave plate and the p– or s–polarised output is detected. The variation with α is fitted to Equation 2.23 and 2.24. The graphs show the SHG intensity as a function of input polarisation angle, α, of linear polarised light, with respect to the optical plane of incidence. The SHG intensities have been normalised to the square of the laser power. Figure 5.16 show the geometry of the experiments performed in relation the Ag deposited on rippled Si. Placement of the plane of incidence across the NP array is given the designation x, whereas placement of the plane of incidence along the NP array is defined as y. α-p and α-s measurements were perfomed on the capped and uncapped Ag on rippled Si samples, in both x and y azimuths. The α-s measurements should reveal interesting information on the symmetry of the NPs in the plane of surface: a centrosymmetric NP will have a negligible sS response.

The results to follow will discuss the SH response from capped Ag on rippled Si samples alone, when SHG was performed on uncapped samples tarnishing of

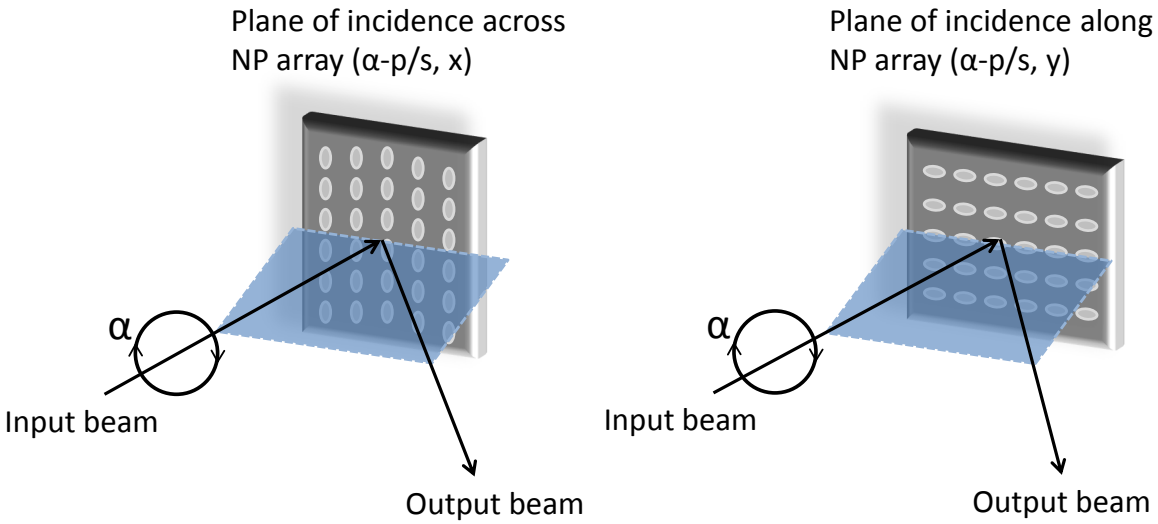

Figure 5.16: Explanation of the geometry of SHG measurements. α-px (or α-sx) measures the SH response across the aligned NP array, while α-py (or α-sy) measures the SH response along the aligned NP array.

the Ag islands made it difficult to obtain reproducible results. Figure 5.17 shows the α-p response across and along the Ag array of capped samples. The system is modelled as a surface of 1m symmetry, with 10 allowed tensor components (Table 2.1). Table 5.2 and 5.3 show the values of the parameters extracted from the fits and the contributing tensor components associated with each fitting parameter. Error in the fitted parameters were estimated by changing the value of each parameter separately and observing the effect on the residuals, such that an increase of 10% occurs in the residual value e.g. if the original fitted parameter is 2.0 and a 10% increase in the residuals requires increase in parameter value to 2.1, so the parameter value is 2.0 $\pm$ 0.1 expressed as 2.0(1). The original parameter is then reset, and the next parameter error is estimated.

Table 5.2: Fitted parameter values and allowed tensor components for α-p measurements on Ag deposited on rippled Si. Numbers in brackets indicate errors associated with each parameter.

Sample		x-azimuth		y-azimuth	
C5	A	-52(5)	zxx zxz zzz	246(2)	zyy yzy zzz
			xxx xzx xzz		yyy yzy yzz
	B	188(1)	zyy xyy	5(9)	zxx yxx
	C	1(4)	zxy zyz	4(1)	zyx zxz
			xyx xyz		yxy yxz
C4	A	-45(4)	zxx zxz zzz	236(2)	zyy yzy zzz
			xxx xzx xzz		yyy yzy yzz
	B	150(1)	zyy xyy	9(5)	zxx yxx
	C	5(1)	zxy zyz	5(2)	zyx zxz
			xyx xyz		yxy yxz
C3	A	-15(4)	zxx zxz zzz	184(2)	zyy yzy zzz
			xxx xzx xzz		yyy yzy yzz
	B	122(1)	zyy xyy	0(5)	zxx yxx
	C	0.0(5)	zxy zyz	4(2)	zyx zxz
			xyx xyz		yxy yxz
C1	A	-40(9)	zxx zxz zzz	21(1)	zyy yzy zzz
			xxx xzx xzz		yyy yzy yzz
	B	57(7)	zyy xyy	46(2)	zxx yxx
	C	0 (9)	zxy zyz	6(1)	zyx zxz
			xyx xyz		yxy yxz

Overall the SHG response of the capped samples increase with increasing aspect ratio, with sample C5 having the largest aspect ratio and sample C1 having the smallest. Figure 5.17 shows a larger response along the islands than across them, due to coupling along the NP array. In the case of sample C5, which has the largest aspect ratio, the response is more than 10 times larger than the native–oxide covered rippled Si of the same periodicty used to make the Ag on rippled Si samples. The α–px response is dominated by the sP response, due to the excitation along the NP array and the pP response dominates for the α–py response. Generally α-p measurements are more difficult to interpret due to the

Table 5.3: Fitted parameter values and allowed tensor components for α-s measurements on Ag deposited on rippled Si. The numbers in brackets indicate errors associated with the parameter.

Sample		x-azimuth		y-azimuth	
C5	F	0.0(2)	yxx yxz yzz	2.8(8)	xyy xyz xzz
	G	20.1(6)	yyy	10.8(8)	xxx
	H	25.7(5)	yxy yzy	27.9(6)	xyx xxz
C4	F	1.7(3)	yxx yxz yzz	6.9(3)	xyy xyz xzz
	G	9.7(3)	yyy	4.5(2)	xxx
	H	18.0(6)	yxy yzy	19.0(3)	xyx xxz
C3	F	0.1(5)	yxx yxz yzz	0.0(3)	xyy xyz xzz
	G	6.0(4)	yyy	5.5(4)	xxx
	H	8.1(4)	yxy yzy	16.1(2)	xyx xxz
C1	F	0.9(3)	yxx yxz yzz	0.0(4)	xyy xyz xzz
	G	4.6(3)	yyy	8.3(11)	xxx
	H	18.7(2)	yxy yzy	$20.0(7)e^{i55}$	xyx xxz

number of tensor components involved, as shown in Table 5.2. It may be possible to monitor the pP response during deposition of Ag, as the response along the Ag array is strongest.

Usually s–polarised responses varies as $\sin^2 2\alpha$ via the H parameter in Equation 2.24. Figure 5.18 shows the α-s measurements performed in both azimuths. Both x and y responses are dominated by large C terms which account for their $\sin 2\alpha$ behaviour, however, there is departure from mirror plane symmetry as shown by non–zero G terms, which is indicative of an sS type response, this usally signifies asymmetry in the plane of the surface and would typically be zero in the presence of more centrosymmetric islands. From Table 5.2 sS responses are due to χ_{yyy} component in the xz–plane, or χ_{xxx} in the yz–plane. Larger islands, like sample C5, has the largest sS response, which is expected due to its larger aspect ratio, and decreases as the island gets smaller and more centrosymmetric. Again it may be feasible to monitor the sS response during Ag deposition

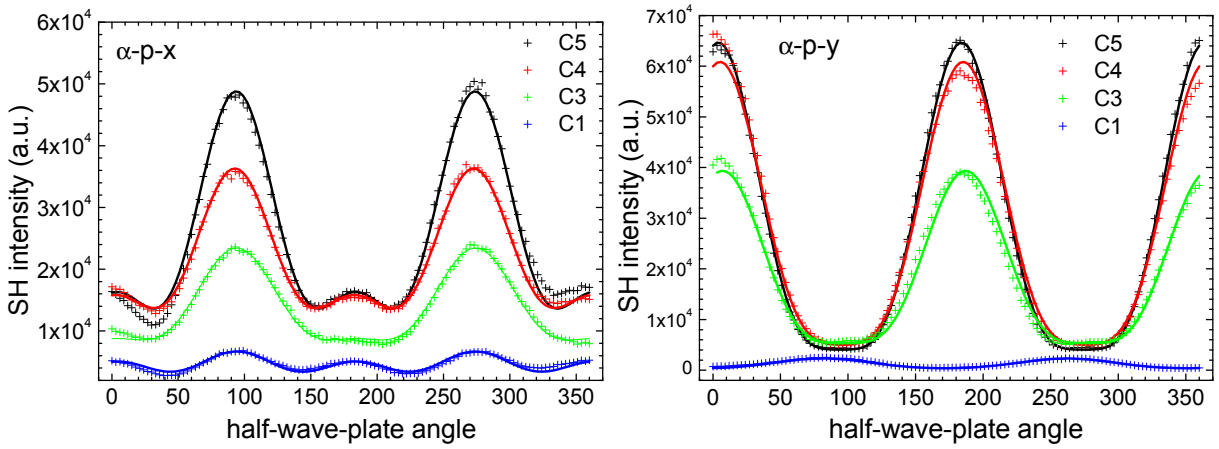

Figure 5.17: α–p response of capped Ag on rippled Si substrates and fits to Equation 2.23. The SH response increases with increasing aspect ratio of the islands. The response along the islands is greater than across, due to coupling between islands in the direction along the islands.

in order to achieve asymmetry in the NP. SHG studies were also performed on samples with Ag on flat Si(001), however, only a very small signal above noise was observed, indicating that the response from centrosymmtric Ag NPs is very small in this experimental geometry.

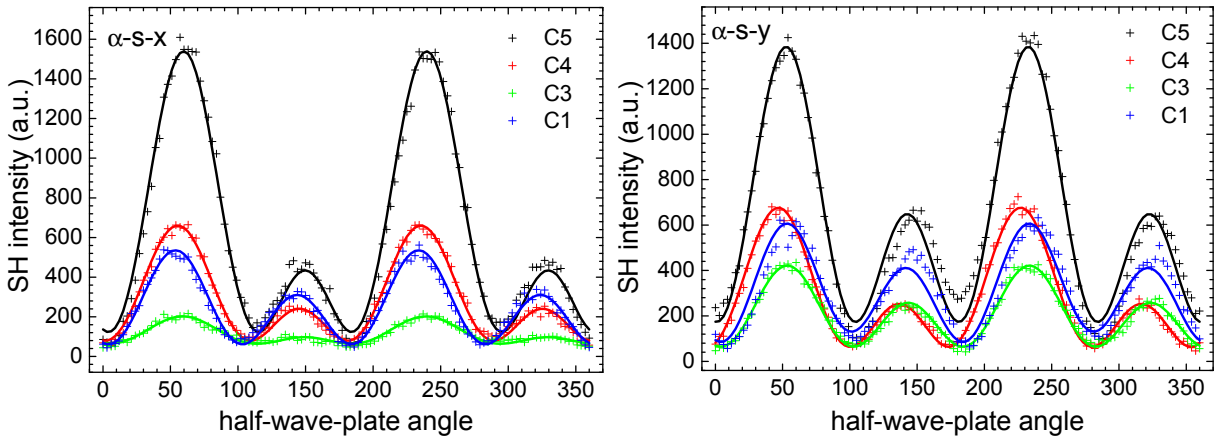

Figure 5.18: α–s response of the capped Ag on rippled Si substrates and fits to Equation 2.24. Responses in both x and y azimuths are dominated by the C term.

5.2.2 Ag on Al_2O_3

A comparative study of the Ag on Al_2O_3 system is discussed in this section in order to fully understand the SH response from Ag on rippled Si. The preparation for these samples are detailed in [22, 64]. The Ag on Al_2O_3 system is a good example of surface–enhanced SHG, as the Al_2O_3 substrate alone has a negliable response and SH response will originate entirely from the Ag NP arrays. Two samples were measured for comparison, on one of which Ag has been deposited on facetted sapphire to create an aligned array of NP, and a second sample where the annealing treatment to produce the facets was not performed, consequently NP arrays are not formed as Ag is deposited on a flat substrate.

5.2.2.1 SHG

Table 5.4 and 5.5 show the fitted parameter values extracted from the fits and the possible tensor components associated with each parameter. Figure 5.19 shows the α-p responses from both azimuths, interestingly all responses are different, highlighting the sensitivity to the NP array. The line shape of the α-p is similar to that of the rippled samples, with the α–px dominated by the sP response, and hence an excitation along the array, also α–py is very large and dominated by the pP response. The α–sx response is complex, which may indicate a nearby electronic resonance. It is dominated by the C term, which explains the $\sin 2\alpha$ behaviour with a small non–zero sS response indicating a small departure from symmetry in the xz plane. α-sy is real and dominated by the excitation along the island array, pS and does not display $\sin^2 2\alpha$ behaviour, proving that the yz plane does not possess mirror plane symmetry. The sS responses, χ_{yyy} and χ_{xxx},

Table 5.4: Fitted parameter values and allowed tensor components for α-p measurements on Ag deposited on Al_2O_3. The numbers in brackets indicate errors associated with the parameter.

Sample		x-azimuth		y-azimuth	
Ag on Facetted sapphire	A	11.7(8)	zxx zxz zzz	131.8(6)	zyy yzy zzz
			xxx xzx xzz		yyy yzy yzz
	B	75.6(1)	zyy xyy	11.4(21)	zxx yxx
	C	0.0(3)	zxy zyz	4.2(8)	zyx zxz
			xyx xyz		yxy yxz
Ag on Flat sapphire	A	311(1)	zxx zxz zzz	286.7(18)	zyy yzy zzz
			xxx xzx xzz		yyy yzy yzz
	B	62(3)	zyy xyy	59.6(43)	zxx yxx
	C	0.0(3)	zxy zyz	0.0(4)	zyx zxz
			xyx xyz		yxy yxz

are smaller than the rippled samples as the NPs in question are much smaller.

Table 5.5: Fitted parameter values and allowed tensor components for α-s measurements on Ag deposited on Al_2O_3. The numbers in brackets indicate errors associated with the parameter.

Sample		x-azimuth		y-azimuth	
Ag on Facetted sapphire	F	0.1(5)	yxx yxz yzz	38.1(7)	xyy xyz xzz
	G	$5.8(7)e^{i129}$	yyy	11.3(13)	xxx
	H	28.8(3)	yxy yzy	12.5(5)	xyx xxz
Ag on Flat sapphire	F	0.0(3)	yxx yxz yzz	0.0(3)	xyy xyz xzz
	G	6.9(12)	yyy	-8.0(6)	xxx
	H	-138.2(11)	yxy yzy	118.0(7)	xyx xxz

Finally Figure 5.21 and 5.22 show Ag deposited on a flat sapphire substrate. The response for α-p and α-s are the same for both x and y azimuths, as the islands do not form anisotropic arrays, confirming that both azimuths are mirror planes of the surface. The α–p response is dominated by the pP response, which is large and real. The α–s responses are dominated by the C term and showing $\sin 2\alpha$. Both azimuths display small non–zero sS terms, this indicates that the

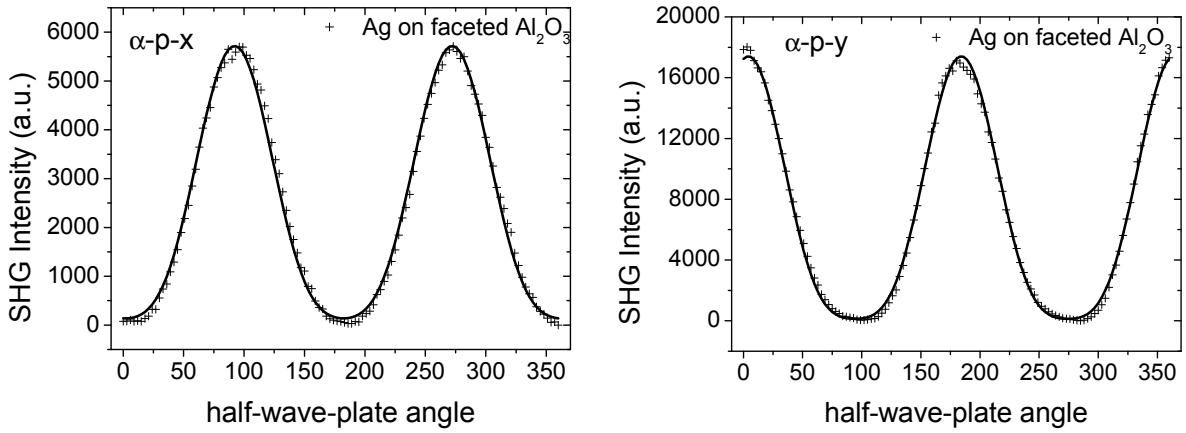

Figure 5.19: α–p response of Ag on facetted sapphire in both azimuths and fits to Equation 2.23. The response is largest along the island array which is consistent with rippled Si studies.

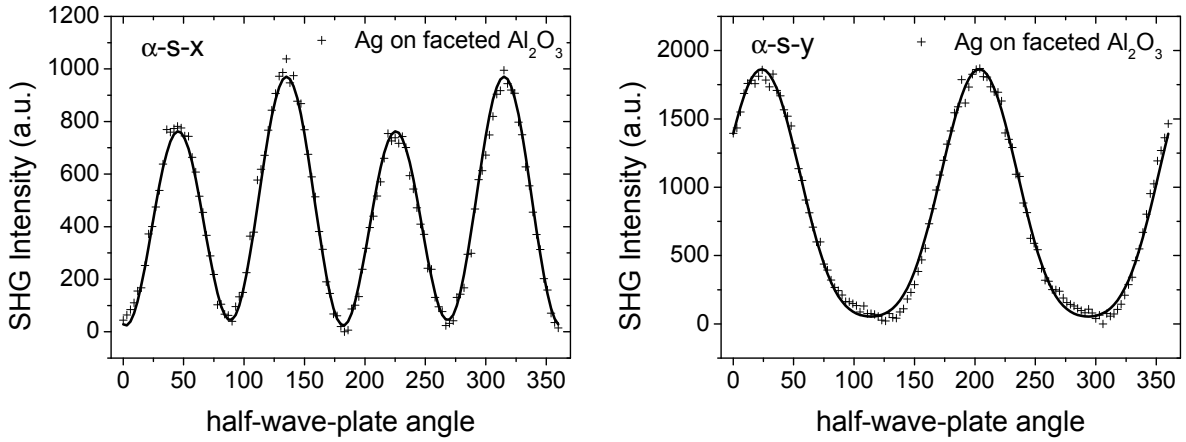

Figure 5.20: α–s response of Ag on facetted alumina and fits to Equation 2.24. α–sy does not observe the typical $\sin^2 2\alpha$ behaviour indicating lack of mirror plane symmetry along the yz plane.

deposition method for Ag produces asymmetric islands.

These results demonstrate SHG can successfully characterise aligned arrays of NPs on anisotropic templates. The SH response is highly sensitive to NP symmetry. There is a strong surface enhanced signal due to LSPRs which amplifies weak nonlinear signals, even in the non–resonant regime.

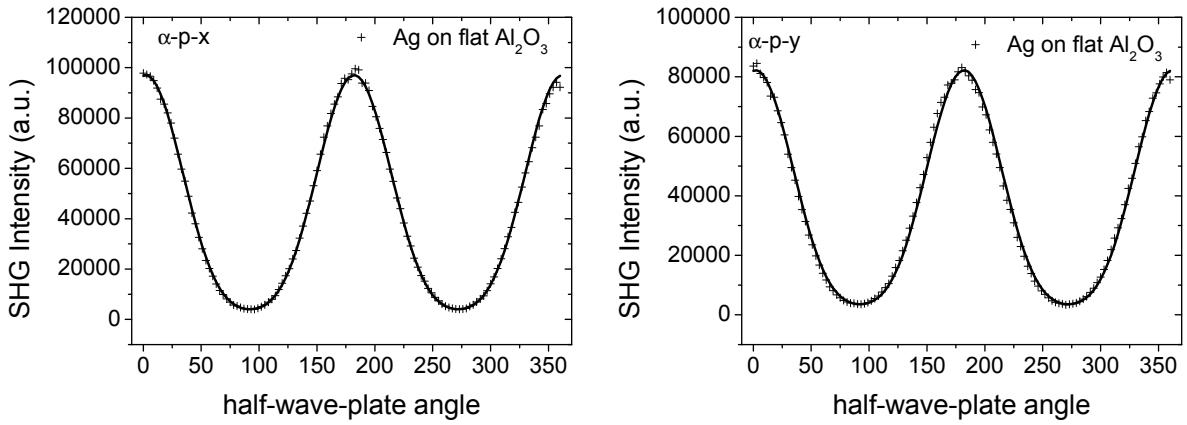

Figure 5.21: α–p response of Ag on a flat sapphire substrate and fits to Equation 2.23. The responses along both azimuths are similar since the islands are deposited on a flat substrate producing more isotropic islands.

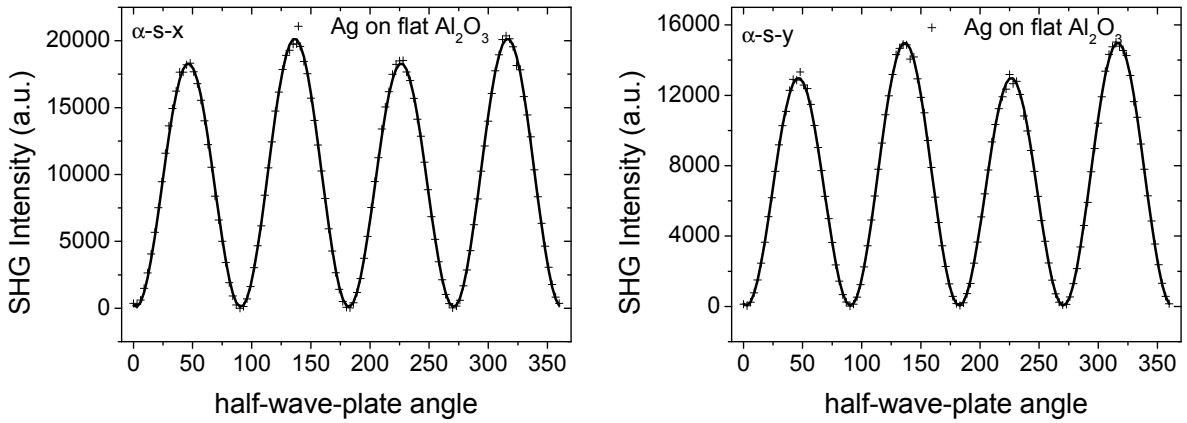

Figure 5.22: α–s response of Ag on a flat alumina substrate and fits to Equation 2.24. Responses are the same in both azimuths indicating a mirror plane in both x and y directions, as the Ag is deposited on a flat substrate. The responses are dominated C term.

5.3 Conclusions

Epioptic techniques have been used to characterise rippled Si templates in ambient as well as in UHV conditions. The RAS response of the ripples showed an increase in RAS amplitude with ion fluence within the first few hours of ripple

formation when prepared *in situ*, which seemed to be contrary to initial studies in ambient. The results were similar for SHG studies, where an increase in signal was observed after the fist 3 hours of irradiation, after which the signal begins to decrease. It is likely that the strain–related response is dominant during the first few hours of ripple formation, which tends to relax when longer ripples form on the surface. Further experiments monitoring the RAS and SHG signals at shorter intervals could be interesting as they will demonstrate at what stage the strain begins to change.

The RAS response of Ag deposited on rippled Si templates was measured and large anisotropies were observed, the size of which was consistent with the aspect ratios of the NPs calculated from SEM images. The SHG from these plasmonic structures was also measured and the amplitude of their response was consistent with RAS results. Overall samples with larger aspect ratios produced stronger SH responses, with the responses along the NP array being stronger than across the array. It was possible to determine the symmetry of the NPs from the extracted fitting parameters, where islands of larger aspect ratios displaying departures from mirror plane symmetry, indicated by a non zero sS components (χ_{xxx} and χ_{yyy}). SHG experiments were also performed on a Ag on facetted alumina system to determine the extent to which the SH responses varied on a similar system of 1m symmetry. The results were consistent: the SH response had a larger response along the Ag array and departures from mirror plane symmetry could be observed, with similar lineshapes in most cases. The SH response is highly sensitive to morphology of the NP layer, as confirmed from the response of silver on flat alumina substrate where the repsonses were equal in both azimuths. Undoubtedly the rippled Si system contains contributions from the oxide interface and possibly

strain related signals, further experiments will be required to determine the extent to which this is the case. However, we expect that for larger islands deposited on longer periodicities the large signals from the metal NPs may make these contributions negligible. It may also be interesting to perform SHG studies on arbitrary shaped islands to investigate the dependence on the SHG response. These results are among the first of their kind as polarisation dependent SHG is seldom reported as a characterisation technique for systems of this kind.

Chapter 6

Optical characterisation of small organic chiral molecules at surfaces

> "I call any geometrical figure, or any group of points, chiral, and say it has chirality, if its image in a plane mirror, ideally realized, cannot be brought to coincide with itself."
>
> *–Lord Kelvin*

The importance of developing optical techniques for characterising small chiral molecules adsorbed on surfaces was discussed in Chapter 1. This chapter investigates the chirality of ultra–thin films using epioptic techniques. The phenomenological model was tested using the well studied chiral molecule, 1,1'–

binaphthalene-2,2'–diol (hereafter referred to as binol), on a fused silica substrate measured in a transmission geometry. The model was then applied to the smaller cysteine molecules adsorbed on Si(001) and Au(110), in reflection geometry. The work in the ambient described here has been published in *physica status solidi (b)* [150].

6.1 Ultra–thin binol films on fused silica

The sample preparation for binol films is detailed in Section 3.2.2. Experiments were performed in ambient conditions, on binol films deposited on fused silica for comparison with the previous work of Hicks *et al* [41, 42]. A solution of binol was deposited on fused silica and SHG measurements were carried out in a transmission geometry (Figure 6.1). Unamplified 130 fs laser pulses were used, with an average power of 200 mW, a repetition rate of 76 MHz and a beam diameter of 60 μm at the sample. A quarter–wave plate in the input beam was rotated and the p–polarised second harmonic (SH) response was measured as a function of the wave plate angle, θ, which is the angle between the fast axis of the wave plate and the p–polarised direction.

A film of average thickness 50 nm was deposited after evaporation of the solvent. The SH response from both (R)– and (S)–enantiomers was recorded. Coverage was found to be uneven for the samples, as confirmed by optical microscopy, and produced SHG intensities that varied by up to four orders of magnitude as the laser beam was scanned over the sample. No signal above background was observed from the fused silica substrate in uncoated areas, confirming that the signal is as a result of the binol film. Data were taken from the thinnest regions

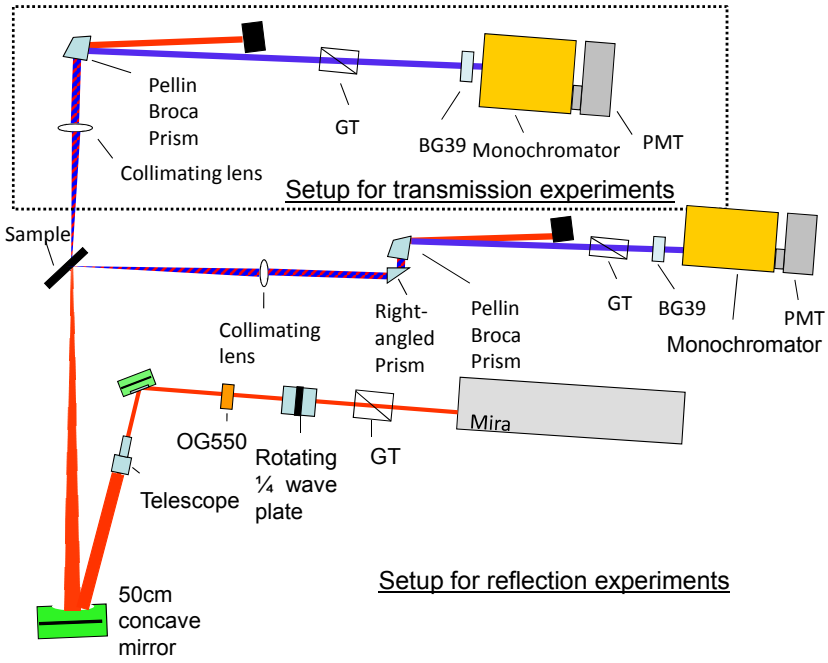

Figure 6.1: Experimental arrangement for chiral SHG studies in the ambient for reflection and transmission geometries.

of the film, where there was still a measurable change from the SHG responses of the substrate. Given the four orders–of–magnitude variation in SHG intensity, and allowing for the quadratic dependence on thickness, the regions sampled are estimated to be a few monolayers thick.

Table 6.1: Fitted parameter values and allowed tensor components for (R)–(+)–binol on fused silica. Numbers in brackets indicate errors associated with each parameter.

Parameter		Allowed tensor component
f′	1.8(2)	χ^{eee}_{zzz}, χ^{eee}_{zxx}, χ^{eee}_{xxz}
g′	-1.89(3)	χ^{eee}_{zxx}
h′	0.0(10)	χ^{eee}_{xyz}
f″	0.22(3)	χ^{eem}_{xzy}, χ^{eem}_{zxy}, χ^{mee}_{xyz}
g″	11.1(7)	χ^{eem}_{xyz}, χ^{eem}_{zxy}
h″	-7.6(6)	χ^{eem}_{xxz}, χ^{eem}_{xzx}, χ^{eem}_{zxx}, χ^{eem}_{zzz}, χ^{mee}_{xxz}

As discussed in Section 2.2.2, a simultaneous least–squares fit of Equation 2.30 to the measured SH response of both enantiomers, and the racemic was used:

$$I(2\omega) \propto (f' - g' + 4f'' \cos 2\theta - (f' - g') \cos 4\theta + 2h'' \sin 2\theta - h' \sin 4\theta)^2 + (f'' - g'' - 4f' \cos 2\theta - (f'' - g'') \cos 4\theta - 2h' \sin 2\theta - h'' \sin 4\theta)^2 \quad (2.30)$$

For a p–polarised output, the parameters f and g depend only on achiral tensor components, while h depends on chiral tensor components and thus changes sign between (R)– and (S)–enantiomers. Conversely, for an s–polarised output f and g depend on chiral components, which change sign between enantiomers, and h contains only achiral components.

The SHG response from the binol films was stable and did not show evidence of photobleaching or photodegradation. Figure 6.2 shows the normalised p–polarised fitted data for binol films, obtained using the transmission geometry shown in Figure 6.1, with an angle of incidence of 45 °. The response from (R)– and (S)–enantiomers is very different, confirming a strong chiral response. Reasonable fits are obtained, where the difference in the response of the enantiomers

Table 6.2: Fitted parameter values and allowed tensor components for (S)–(−)–binol on fused silica.Numbers in brackets indicate errors associated with each parameter.

Parameter		Allowed tensor component
f′	1.83(2)	χ^{eee}_{zzz}, χ^{eee}_{zxx}, χ^{eee}_{xxz}
g′	-1.89(12)	χ^{eee}_{zxx}
h′	0(1)	χ^{eee}_{xyz}
f″	0.2(4)	χ^{eem}_{xzy}, χ^{eem}_{zxy}, χ^{mee}_{xyz}
g″	11.1(2)	χ^{eem}_{xyz}, χ^{eem}_{zxy}
h″	7.6(2)	χ^{eem}_{xxz}, χ^{eem}_{xzx}, χ^{eem}_{zxx}, χ^{eem}_{zzz}, χ^{mee}_{xxz}

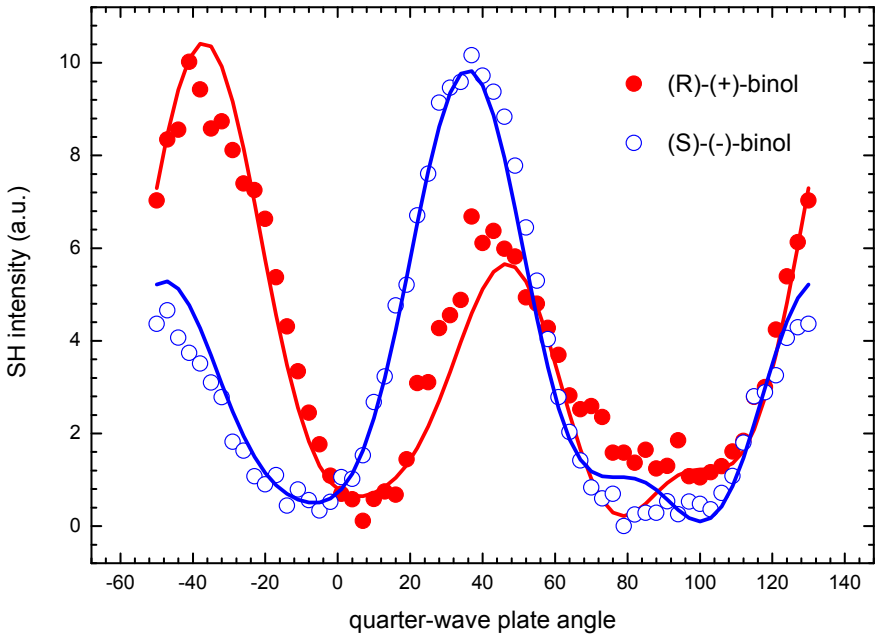

Figure 6.2: SHG response of (R)–(+)–binol (filled circles) and (S)–(-)–binol (open circles) on fused silica in transmission geometry, and fits (solid lines) to Equation 2.30.

is accounted for by simply changing the sign of the chiral component, h, while maintaining its absolute value. All other parameters are constrained to have the same value for the two enantiomers, as required by theory.

The amplitude of the chiral parameter h is relatively large, being about half

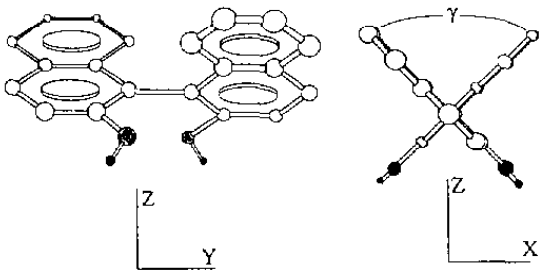

Figure 6.3: Binol geometry and molecular coordinates, where γ indicates the inter–ring twist angle from [151].

the size of g, and is imaginary, within the error estimate. The largest parameter is g, which is also complex, while f is real and quite small. At 45 °, the electric dipole tensor components of f appear in the form $\chi^{eee}_{zzz} + \chi^{eee}_{zxx} - 2\chi^{eee}_{xxz}$, while g depends on χ^{eee}_{zxx} [111]. Molecular hyperpolarisability calculations indicate that away from resonance, the α^{eee}_{zzz} component makes the largest contribution to the SHG of binol, where the z–axis is defined as the bisector of the inter–ring twist angle [151]. Even allowing for the partial cancellation between components in the f term, it appears likely that the dominance of the g term, and thus the χ^{eee}_{zxx} component, indicates that the average orientation of the binol molecules does not have the molecular z–axis normal to the surface (Figure 6.3). A racemic mixture (50:50 mixture of both enantiomers) was also measured for comparison, which is shown in Figure 6.4. The response in this case is quite different than that for R– and S–enantiomers: the fit was performed by using the same values of f and g, while setting the chiral component h to zero. The scatter in the sample data is thought to originate from the roughness apparent on the film.

The work of Hicks *et al* on binol had the added complexity of performing experiments spectroscopically in order to observe resonantly enhanced SH effects,

Table 6.3: Fitted parameter values and allowed tensor components for racemic–binol on fused silica.Numbers in brackets indicate errors associated with each parameter.

Parameter		Allowed tensor component
f′	1.8(6)	χ^{eee}_{zzz}, χ^{eee}_{zxx}, χ^{eee}_{xxz}
g′	-1.9(9)	χ^{eee}_{zxx}
h′	0.0(2)	χ^{eee}_{xyz}
f″	0.2(6)	χ^{eem}_{xzy}, χ^{eem}_{zxy}, χ^{mee}_{xyz}
g″	11.1(4)	χ^{eem}_{xyz}, χ^{eem}_{zxy}
h″	0.0(2)	χ^{eem}_{xxz}, χ^{eem}_{xzx}, χ^{eem}_{zxx}, χ^{eem}_{zzz}, χ^{mee}_{xxz}

as shown in Figure 6.5. As the SH wavelength was tuned closer to a resonance lying between 200 nm and 250 nm, the chiral effect is amplified, and a large difference between left– and right–circularly polarised light is observed. However, the work in this section confirms that even off–resonance, using polarisation rotation studies, chiral information from tensor components can be extracted successfully, and suggests that this method may also be applicable to smaller chiral molecules. As discussed in Chapter 1, no SHG studies have been reported on small chiral molecule adsorption on well–characterised single crystal surfaces. The following section will investigate applying the methods discussed here to cysteine, a small chiral amino acid, on reflecting surfaces.

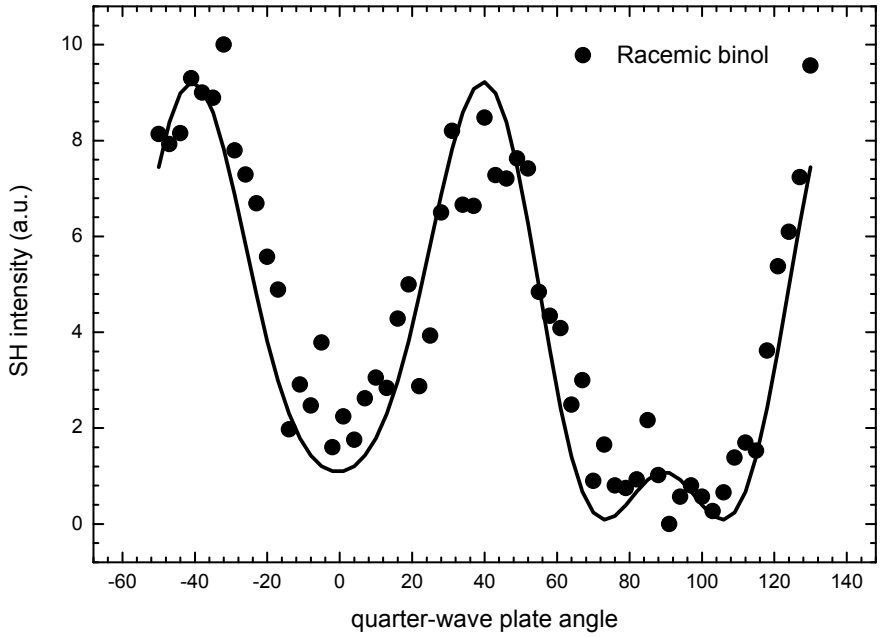

Figure 6.4: SHG response of racemic binol on fused silica in transmission geometry, and fit (solid line) to Equation 2.30.

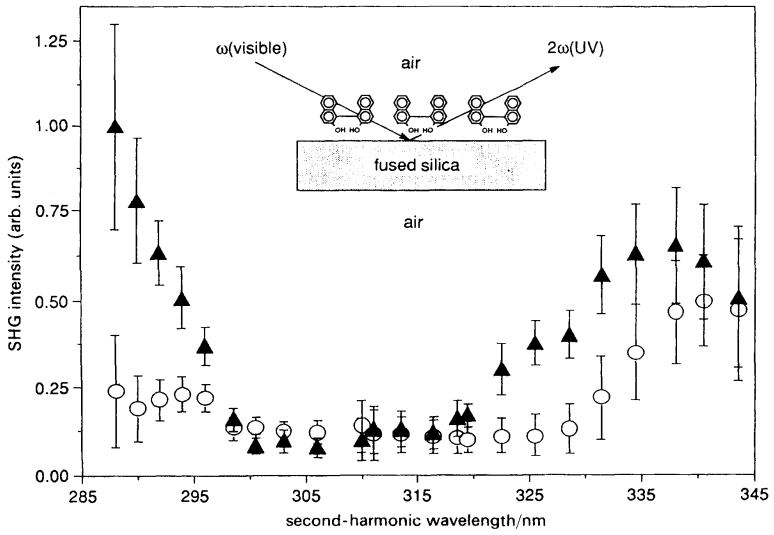

Figure 6.5: SHG efficiencies as a function of the second–harmonic wavelength for (R)–binol at the air/silica interface using left– (closed triangles) and right–circularly (open circles) polarised light (after [152]).

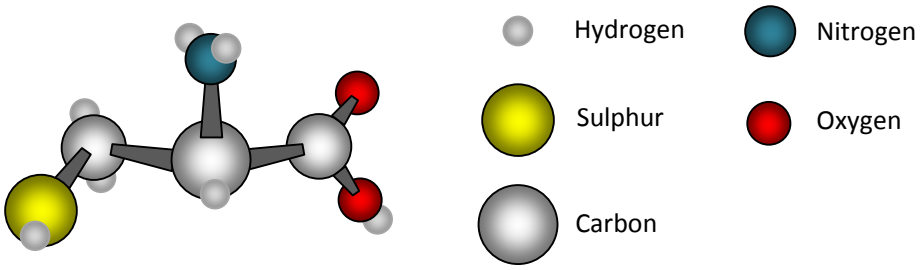

Figure 6.6: Model of cysteine.

6.2 Cysteine on reflecting surfaces

The successful application of our model to the previously studied binol system allowed other thin film chiral systems to be investigated, namely ultra–thin cysteine films on reflecting surfaces. Cysteine (Figure 6.6) is a small amino acid of considerable biophysical interest, as discussed in Chapter 1. Films of cysteine were prepared and deposited on native–oxide–covered Si(001), while cysteine MLs were prepared on Au(110) surfaces.

6.2.1 Cysteine on Si(001)

The sample preparation for cysteine films on Si(001) is discussed in detail in Section 3.2.3). A solution of cysteine was dissolved in water and deposited on a native–oxide–covered Si(001) substrate and the p–polarised SHG response was measured in ambient, in a reflection geometry, at 45 ° (Figure 6.1). Again the coverage was found to be uneven, and data were taken from the thinnest regions of the film, where there was a measurable change from the SHG response of the substrate. In the case of the cysteine on Si(001), an additional fit on the data

Table 6.4: Fitted parameter values and allowed tensor components for clean Si(001), where f',g',h' indicate real components, while f'', g'' and h'' indicate imaginary components. Numbers in brackets indicate errors associated with each parameter.

Parameter		Allowed tensor component
f′	0.435(6)	χ^{eee}_{xxz}, χ^{eee}_{zxx}, χ^{eee}_{zzz}
g′	-0.23(2)	χ^{eee}_{zxx}
h′	0.232(1)	χ^{eee}_{xyz}
f″	0.0(10)	χ^{eem}_{xzy}, χ^{eem}_{zxy}, χ^{mee}_{xyz}
g″	-1.162(8)	χ^{eem}_{xyz}, χ^{eem}_{zxy}
h″	0.36(1)	χ^{eem}_{xxz}, χ^{eem}_{xzx}, χ^{eem}_{zxx}, χ^{eem}_{zzz}, χ^{mee}_{xxz}

from the substrate alone was included, as native–oxide–covered Si(001) produces a significant SHG response [34]. This allowed the substrate contribution to the overall response to be determined. However, on film deposition, the measured substrate response may require to be scaled in amplitude and, as the overall SH response is the coherent sun of the substrate and film response, a complex phase factor has to be introduced. Thus two additional fitting parameters are required (Table).

$$P_{total}(2\omega) = P_{film}(2\omega) + Ae^{i\phi}P_{sub}(2\omega) \tag{6.1}$$

where the total SH polarisability, $P_{total}(2\omega)$, is the coherent sum of the film contribution, $P_{film}(2\omega)$, and the substrate contribution, $P_{sub}(2\omega)$, allowing for a scaling factor, A, and a complex relative phase factor, ϕ. A reasonable fit could not be obtained if a contribution from the substrate was not included. For measurements nonresonant at both ω and 2ω, the electric dipole terms are real and the magnetic dipole terms are imaginary. Phase differences between chiral and achiral tensor components make a significant contribution to the sensitivity of the technique.

The Si(001) substrate is known to give a dichroic response arising from in-

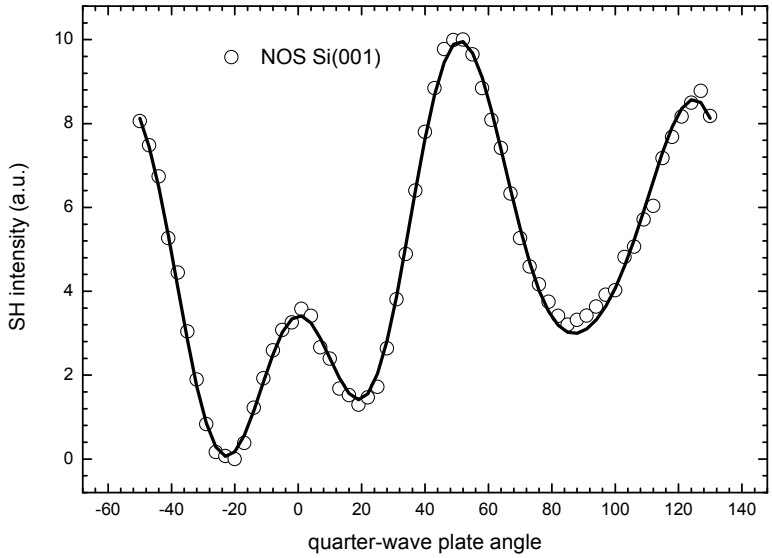

Figure 6.7: SHG response of native–oxide covered Si(001), in reflection geometry at 45 °, and fit to Equation 2.30.

Table 6.5: Fitted parameter values and allowed tensor components for (R)–(+)–cysteine on Si(001), where f',g',h' indicate real components, while f'', g'' and h'' indicate imaginary components. The parameters h' and h'' change sign for (S)–(−)–cysteine. Numbers in brackets indicate errors associated with each parameter.

Parameter		Allowed tensor component
f′	0.244(4)	χ^{eee}_{xxz}, χ^{eee}_{zxx}, χ^{eee}_{zzz}
g′	-0.14(1)	χ^{eee}_{zxx}
h′	0.088(6)	χ^{eee}_{xyz}
f″	0.000(5)	χ^{eem}_{xzy}, χ^{eem}_{zxy}, χ^{mee}_{xyz}
g″	1.806(9)	χ^{eem}_{xyz}, χ^{eem}_{zxy}
h″	0.831(6)	χ^{eem}_{xxz}, χ^{eem}_{xzx}, χ^{eem}_{zxx}, χ^{eem}_{zzz}, χ^{mee}_{xxz}

terference between bulk quadrupolar and interface dipolar terms [153]. This is an optical effect at the Si/SiO_2 interface, and does not arise from chiral structures at the interface. Figure 6.7 shows the SH response, together with the fit, of the native–oxide–covered Si(001). The fitted parameter values from Table 6.4, were used to determine the substrate contribution to the overall signal. Figure

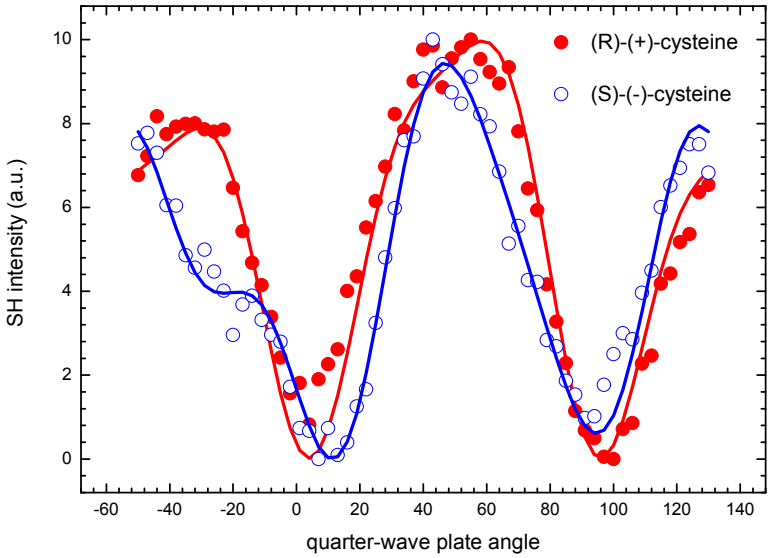

Figure 6.8: SHG response of ultra–thin films of (R)–(+)–cysteine (filled circles) and (S)–(-)–cysteine (open circles) deposited on native–oxide–covered Si(001), in reflection geometry at 45 ° angle of incidence, and fits to Equation 2.30.

6.8 shows the normalised p–polarised SHG data with fits for the cysteine films, obtained using the reflection geometry. The substrate tensor components were scaled at 0.4 of the cysteine component values and the phase difference 160 ° (Table 6.5). There is a clear difference in the SHG response from (R)– and (S)–enantiomers. As with the binol film, the fits show that the difference in the response of the enantiomers can be accounted for by simply changing the sign of h, thus confirming a detectable chiral response. The quality of the fit was assessed by repeating the least squares fit with $h = 0$, which would be the case if there were no detectable chiral response. This resulted in a much poorer fit, with the residuals worsening by a factor of 5.8 for binol and a factor of 3.6 for cysteine. The amplitude of the chiral component of cysteine was about 20% of the achiral contribution.

6.2.2 Cysteine on Au(110)

The sample preparation for cysteine on Au(110) is detailed in Section 3.2.3. Experiments were performed in UHV and experimental details for SHG are described in Section 6.1. The p– and s–polarised SHG response was measured as a function of wave–plate angle using reflection geometry (Figure 6.1). As with cysteine on Si(001), SHG measurements were made on the clean, well–ordered surface of Au(110) first, in order to determine the substrate contribution. RAS was then used to monitor the deposition and coverage of cysteine on Au(110) in real time, and a comparison was made with the previous work of Isted *et al* [88]. The SHG response of cysteine on Au(110) was then measured. Separate experiments were performed for the enantiomers (R)–(+)– and (S)–(−)–enantiomers.

The adsorption of cysteine onto various substrates has been widely studied [154, 155]. Due to the presence of the thiol group (Figure 6.6), cysteine tends to bond favorably on gold surfaces. The adsorption of cysteine on Au has been studied extensively, particularly on the (111) and (110) surfaces [156–159]. The surface of Au(110) forms a 2×1 missing–row reconstruction at room temperature. The main characteristic of the missing–row reconstruction is the formation of (111) microfacets, leading to the removal of every second atomic row along the $[1\bar{1}0]$ direction. The adsorption of cysteine on the Au(110)–2×1 surface causes the hydrogen atom of the sulphhydryl group (HS–) to be dissociated, allowing a strong covalent bond to be formed between the sulphur atom and the Au surface.

Depositing with the substrate at low temperatures, cysteine molecules are physisorbed on the surface and the hydrogen atom of the mercapto group does not

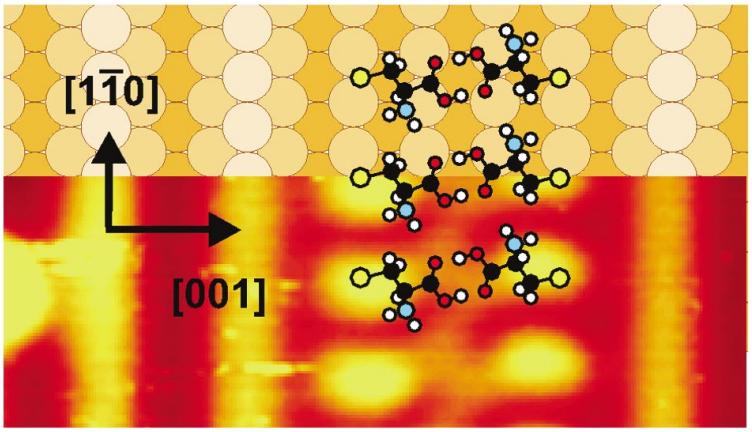

Figure 6.9: Most stable double–row structure, obtained from density functional theory (DFT) calculations, superimposed onto an STM image for the (S)–(-)–cysteine on Au(110) surface (after [160]).

dissociate, preventing a strong linkage to the substrate. Increasing the temperature above 270 K causes dehydrogenation of the cysteine molecules and cysteine becomes chemisorbed on the surface via a covalent sulphur–gold bond. Annealing with the temperature between 300 K and 400 K, the cysteine chains form dimers and dense chiral domains along the [1$\bar{1}$0] direction. Previous STM studies on the adsorption geometry of cysteine on the gold surface indicate that the cysteine induces a surface rearrangement and forms double–row structures, where two cysteine molecules arrange themselves in molecular pairs along the [1$\bar{1}$0] direction (see Figure 6.9), with the main axis of the pair rotated in opposite directions for each enantiomer [160]. Care was taken not to anneal above 420 K, as there is evidence of dissociative desorption, where only atomic sulphur is left behind [161]. The evaporation of cysteine from our source was monitored by a quadrupole mass spectrometer. The main peak was at 121 a.m.u., which is evidence that the cysteine evaporated without decomposition.

As with previous chiral systems a simultaneous least–squares fit of Equation 2.30 to the SH response of both enantiomers was used. However, for the α–s response the sign of f and g is reversed between enantiomers, as they depend on chiral tensor components and h depends on achiral components. As mentioned for cysteine on Si(001) measured in the ambient, an amplitude and phase factor was included in the fit in order to account for the overall size and relative phase of the substrate response.

6.2.3 RAS response of cysteine on Au(110)

The adsorption of cysteine on Au(110) in UHV has been studied previously by RAS [88], allowing a comparitive analysis to be performed prior to the nonlinear studies. The RAS spectrum of the clean Au(110) surface shows negative–going peaks at 2.5 eV and 3.5 eV (Figure 6.10 and 6.11), and hence higher reflectivity along the [001] direction, relative to the [1$\bar{1}$0] direction. The RAS profile is similar to previous observations [91, 162, 163]. The RAS features above 2 eV have been assigned to surface modified bulk transitions, while the region below 2 eV is sensitive to adsorbates and has been assigned to transitions involving surface states. The amplitude of the overall RAS response obtained is larger than that of previous work, which would tend to indicate better surface order, but the 2.5 eV peak is less intense than previous work. LEED confirms a well–ordered surface (Figure 6.14c). On deposition of cysteine the region below 2 eV attenuates and the ratio of the 2.5 eV to the 3.5 eV peak heights increases, in agreement with previous work [88]. The RAS spectra for both (R)–(+)– and (S)–(−)–cysteine were very similar, as shown by Figures 6.10 and 6.11, which

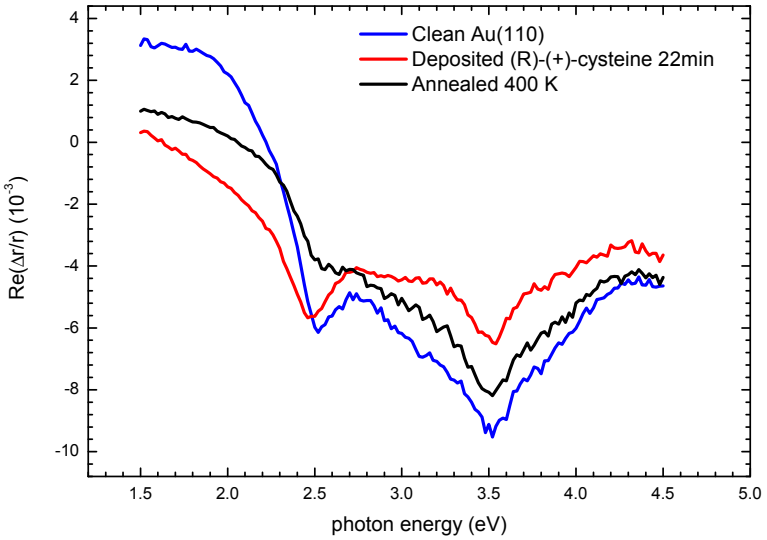

Figure 6.10: Room temperature RAS spectra of the clean Au(110) surface (blue solid line), the (R)–(+)–cysteine saturated surface (red solid line) and the (R)–(+)–cysteine saturated surface following heating to 400 K and cooling to room temperature (black solid line).

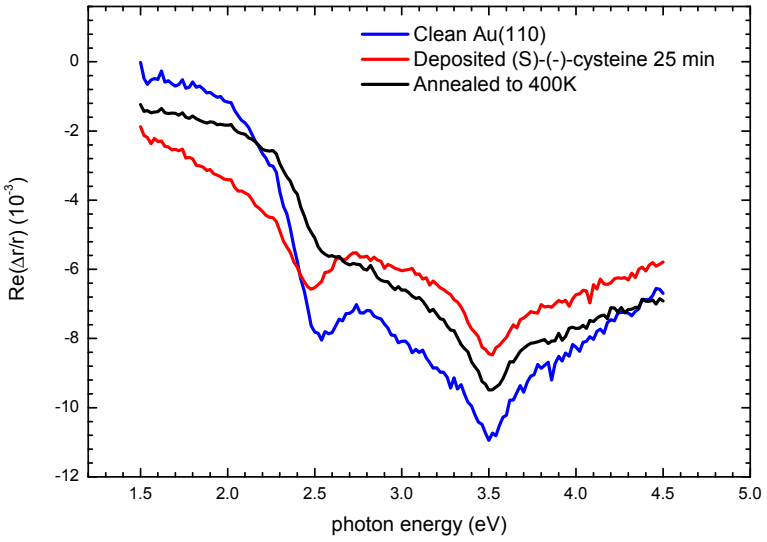

Figure 6.11: Room temperature RAS spectra of the clean Au(110) surface (blue solid line), the (S)–(−)–cysteine saturated surface (red solid line) and the (S)–(−)–cysteine saturated surface following heating to 400 K and cooling to room temperature (black solid line)

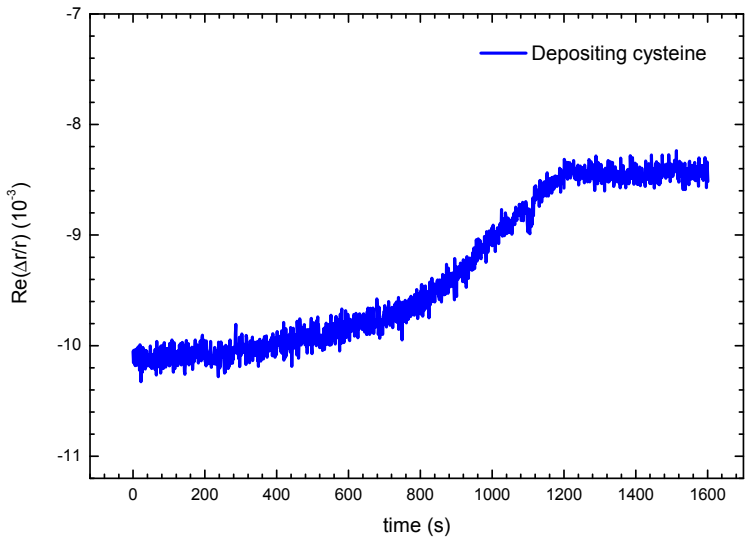

Figure 6.12: The RAS spectra response at 3.5 eV, monitoring the deposition of cysteine on Au(110) in real time. The signal increases by 2 RAS units until a plateau is reached.

compare clean Au(110) with the deposition of cysteine before and after annealing the sample to 400 K. On annealing to 400 K, the 2.5 eV peak is sigificantly attenuated, consistent with previous annealing studies [88]. The reproducible changes in the RAS spectra make it possible to follow the deposition in real time by monitoring the 3.5 eV peak. On deposition at RT the RAS signal increases in intensity (normally by 2 RAS units) until a plateau is reached (Figure 6.12).

Figure 6.13 shows the differential RAS spectra, plotted in order to identify any differences between the deposition of the enantiomers. The major differences lie in the surface state region between 1.5 eV and 2.5 eV, but the left inset shows that comparable changes occur between clean Au(110)–2×1 surfaces in this region. The sensitivity to surface preparation in this spectral region, where apparent differences between enantiomers is observed, makes the use of RAS to detect chiral differences for this material system problematic. As discussed in

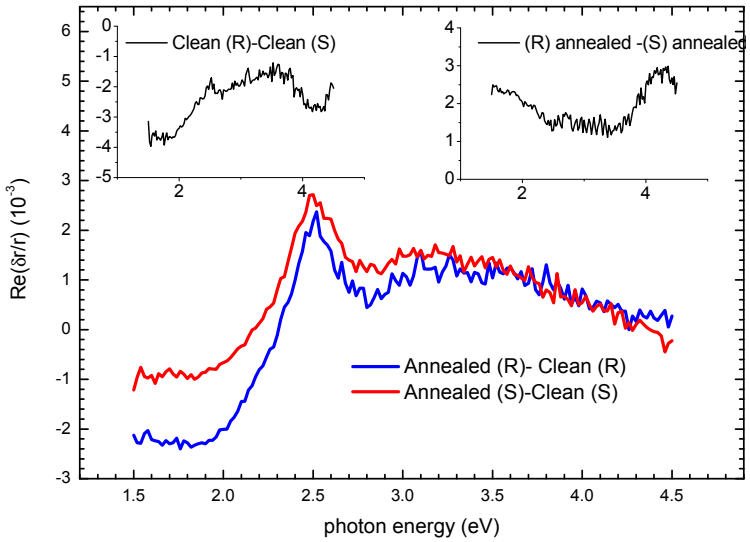

Figure 6.13: Differential RAS spectra: annealed (R)-Clean Au and annealed (S)-Clean Au. Left inset: differential RAS of the clean (R)-Clean (S). Right inset: differential RAS of annealed (R)-annealed (S). The main differences between the spectra lie in the 1.5 eV and 2.5 eV region.

Chapter 1, any differences would have to arise from an indirect mechanism, as linear optical techniques cannot detect chirality in reflection geometry.

LEED patterns were obtained from both enantiomers indicating long range ordering of the adsorbate, although this was much better developed for the (S)–(−)–cysteine (see Figure 6.14). It is interesting that previous work on (R)–(+)–cysteine adsorption on Au(110)–2×1 found no clear LEED pattern [88]. Both LEED images show some evidence of streaking along the $[1\bar{1}0]$ direction, which may be due to increased disorder in this direction. (S)–(−)–cysteine on Au(110) displays a c(4×2) LEED pattern. Line scans were performed on the (R)–(+)–adsorbed surface along the [001] direction in order to identify the order of the adsorbate. (R)–(+)–cysteine still retains a 2×1 reconstruction from the substrate, together with a faint ×3 reconstruction along [001] due to the adsorbate

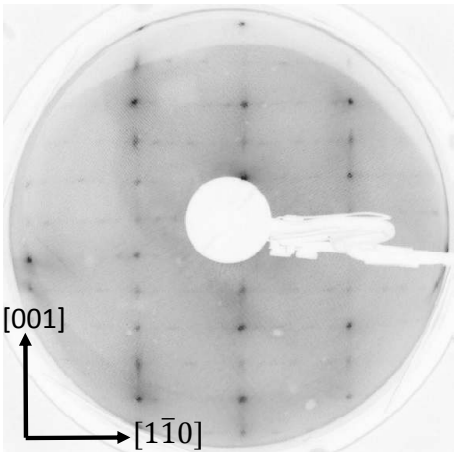

(a) Residual 2×1 of Au(110) superimposed with a faint ×3 reconstruction of (R)–(+)–cysteine in the [001] direction on Au(110)

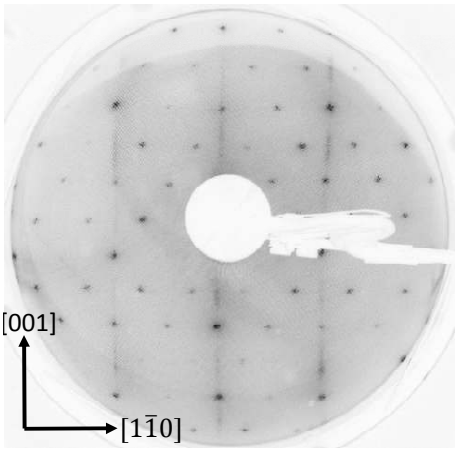

(b) c(4×2) LEED image of (S)–(-)–cysteine on Au(110)

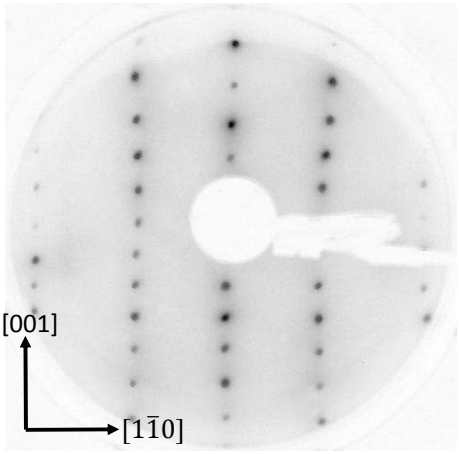

(c) 2×1 reconstruction of the clean Au(110) surface

Figure 6.14: LEED images taken of (R)– and (S)–cysteine on Au(110) compared with the clean Au(110)–2×1, all taken at 129 eV.

(Figure 6.15). The different LEED patterns are a very good indication that the cysteine adsorbed occupies sites on the Au surface which are enantiomer selective, in agreement with previous STM studies [84, 86, 157, 160, 161]. Evidence of enantioselective adsorption of cysteine at kink sites on Au(110)–2×1 was previ-

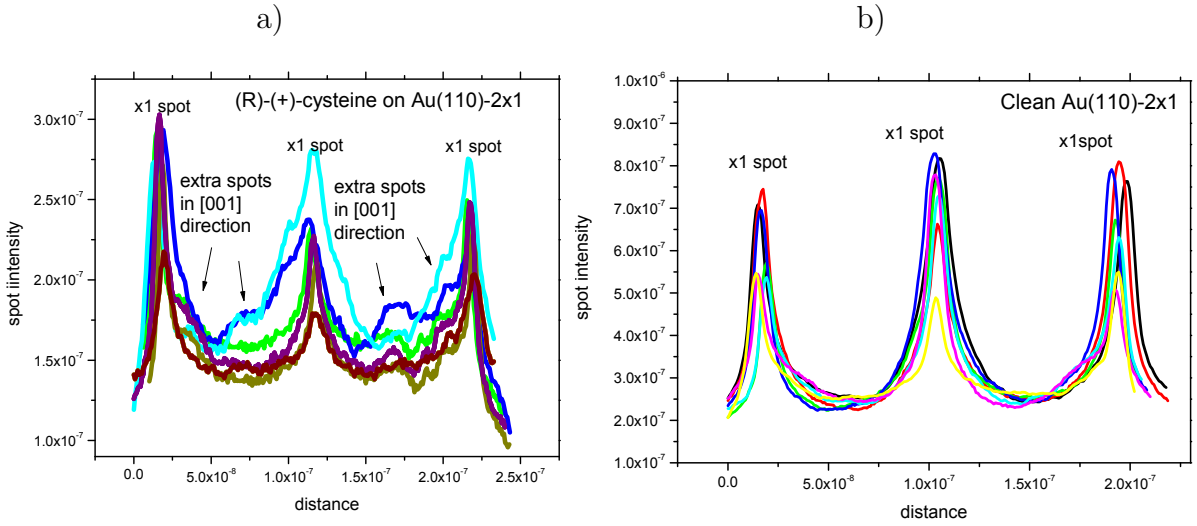

Figure 6.15: Line scans of the LEED spots along the [001] direction. (a) Line scan of the (R)–(+)–cysteine on Au(110)–2×1 surface. (b) Line scan of the clean Au(110)–2×1 surface. Extra spots are found along the [001] with adsorption of the (R)–(+)–cysteine.

ously observed by Kuhnle *et al*, where the surface is assigned R and S sites which are enantiomer selective [85]. This assignment of chirality to surface adsorption sites was introduced by Ahmadi *et al* [164].

6.2.4 SHG response of cysteine on Au(110)

As discussed previously, all data were normalised to the square of the power of the laser. *In situ* α–p and α–s scans were performed on clean Au(110) surface and after adsorption and annealing of cysteine, as monitored using RAS. Unlike the studies of cysteine in ambient, there was little change in the shape of the response. It was found that the α–s scans were much more sensitive to adsorption compared to the α–p measurements. Reproducible results were obtained: (S)–cysteine enhances the SHG signal while the (R)–cysteine reduces it, with line shape remaining the same. In order to determine the substrate contribu-

tion, the two sets of clean α–s Au(110) data, associated with the separate R– and S–cysteine experiments, were fitted simultaneously. A scaling factor of 0.739 between the two sets of data was required, probably due to the optical realignment required between the two separate experiments (Figure 6.16). Interestingly, the fit of clean Au identified a strong chiral response, indicated by the large, predominantly imaginary, f and g terms (Table 6.6). As with Si(001), this may be attributed to interference between bulk electric quadrupole and surface dipole contributions. The achiral and chiral tensor components that may contribute to the f, g and h parameters are listed in Table. It should be noted that, although the variation of the SH intensity with the quarter–wave plate angle looks similar to half–wave plate behaviour REF, the more complicated form of Equation 2.30 requires non–zero values of f, g and h to obtain a best fit to this apparently simple curve.

Repeating these experiments showed that (R)–(+)–cysteine consistently decreased the SH response, while (S)–(−)–cysteine always increased the SH response. Figure 6.17 shows the clean Au(110) response compared to the response with a ML of (R)–(+)–cysteine adsorbed (left) and a ML of (S)–(−)–cysteine adsorbed (right). The two sets of data were fitted simultaneously with the f and g values changing sign between enantiomers. The substrate parameters were fixed at the clean Au(110) values and the phase shift between the substrate and cysteine MLs allowed to vary. Reasonable fits were obtained, with cysteine making a relatively small contribution to the overall fit. Table 6.7 shows the fitting parameters extracted from the fit. The achiral parameter, h, is predominantly real and makes the largest contribution, followed by the chiral parameter, g, which is complex.

Table 6.6: Fitted parameter values and allowed tensor components for clean Au(110), where f',g',h' indicate real components, while f'', g'' and h'' indicate imaginary components. Numbers in brackets indicate errors associated with each parameter.

Parameter		Allowed tensor component
f′	0.0(4)	χ^{eee}_{xyz}
g′	0.9(5)	χ^{eem}_{xxz}, χ^{mee}_{zxx}
h′	0.1(1)	χ^{eee}_{xxz}, χ^{eee}_{yyz}
f″	10.27(7)	χ^{eem}_{xzx}, χ^{mee}_{xxz}, χ^{mee}_{yyz}, χ^{mee}_{zzz}
g″	7.2(7)	χ^{eem}_{xxz}, χ^{mee}_{zxx}
h″	-0.5(2)	χ^{mee}_{xyz}, χ^{eem}_{xzy}, χ^{eem}_{xyz}

A DC level is subtracted from all data prior to fitting, in order to account for an offset due to the background light. By treating this DC level as a fitting parameter, together with a scaling of the intensity, it proved possible to obtain a good fit without including a cysteine contribution. This possible because of the lack of structure in the curves of Figure 6.17. Thus the results are not fully conclusive since the changes in the SHG response are small and unstructured. However, performing the experiment at molecular resonances should greatly enhance these signals. From linear CD spectra, cysteine has a maximum dichroic response at ∼200 nm [165], and so perfoming the experiment with a 400 nm fundamental beam would be expected to enhance the cysteine contribution to the overall signal considerably. Attempts at high efficiency frequency doubling of the 800 nm fundamental to produce a 400 nm beam of sufficient intensity were not successful.

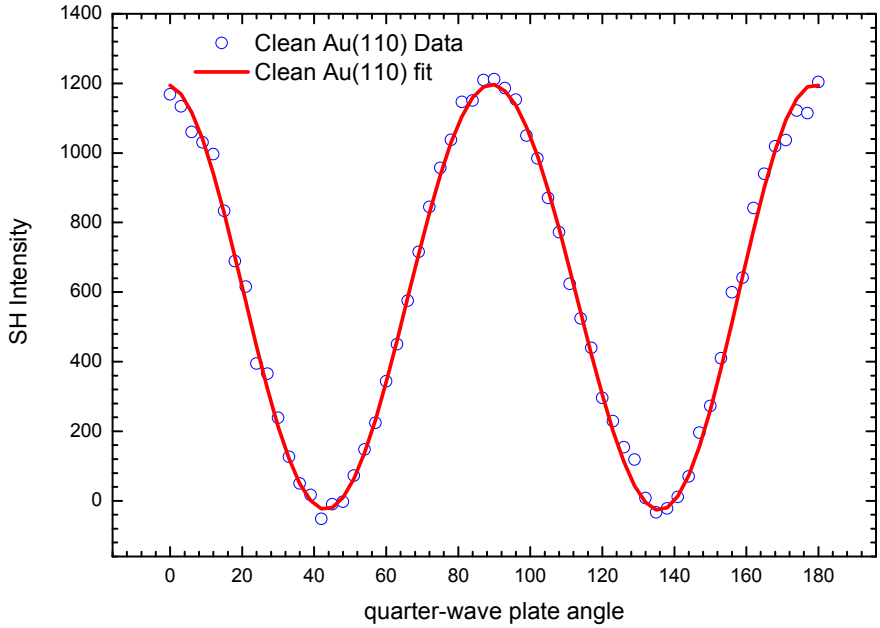

Figure 6.16: α–s response of clean Au(110) measured in *in situ* UHV conditions in reflection geometry at 45 °, and fit to Equation 2.30.

Table 6.7: Fitted parameter values for (R)–cysteine on Au(110). f and g change sign for (S)–(−)–cysteine. The numbers in brackets indicate errors associated with each parameter.

Parameter		Allowed tensor component
f′	0.0(8)	χ^{eee}_{xyz}
g′	-0.3(4)	χ^{eem}_{xxz}, χ^{mee}_{zxx}
h′	-0.8(1)	χ^{eee}_{xxz}, χ^{eee}_{yyz}
f″	0.1(1)	χ^{eem}_{xzx}, χ^{mee}_{xxz}, χ^{mee}_{yyz}, χ^{mee}_{zzz}
g″	0.2(3)	χ^{eem}_{xxz}, χ^{mee}_{zxx}
h″	-0.02(4)	χ^{mee}_{xyz}, χ^{eem}_{xzy}, χ^{eem}_{xyz}

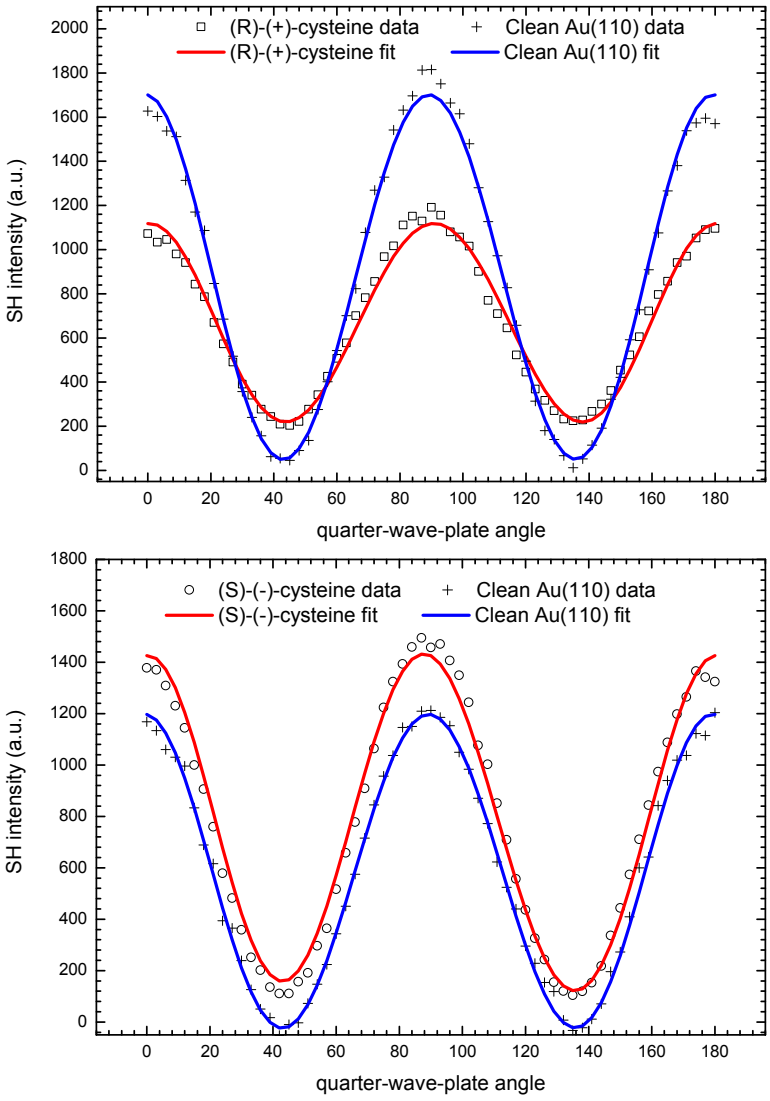

Figure 6.17: α–s response of (R)– and (S)–cysteine on Au(110) measured in UHV conditions in a reflection geometry at 45 °, and fit to Equation 2.30.

6.3 Conclusions

The chirality of ultra–thin films of binol on fused silica was successfully detected using SHG in transmission geometry. The chirality of ultra–thin films of cysteine on native–oxide–covered Si(001) was identified, using reflection geometry, by measuring the substrate response and then including an amplitude and phase factor in the fit of the total SH response. These preliminary studies performed in ambient demonstrate that the chirality of small molecules adsorbed at reflecting surfaces in nm thicknesses can be detected, even away from electronic resonances.

Cysteine was then deposited under UHV conditions on the Au(110)–2×1 surface. Gold was chosen as a substrate due to the strong covalent bond between the sulphur group of cysteine and the gold surface, which results in enantiomer–sensitive adsorption. LEED studies of annealed MLs of the two enantiomers revealed different surface order, indicating chiral adsorption sites, but RAS studies of the two surfaces revealed no significant differences. However, RAS proved to be very useful for monitoring the growth and coverage of the cysteine in real time.

SHG measurements under UHV conditions were made on both surfaces. A repeatable increase in SH response, relative to the clean Au(110)–2×1 surface, was observed on formation of the (S)–(−)–cysteine monolyer and a decrease was observed on formation of the (R)–(+)–cysteine monolayer. This was the only evidence of a chiral effect, as no additional structure was observed in the plots. Good fits were obtained assuming a chiral response, but comparable fits could be obtained by simply scaling the SH response and adjusting the DC level. The results are thus not conclusive and there is strong justification for performing the

experiment near a cysteine resonance in order to amplify the chiral effect.

The results presented in this chapter validate the use of epioptic techniques, ultra–thin films of chiral molecules deposited on crystalline substrates. Although some small molecule systems may require SH resonant enhancements in order to distuinguish the enantiomers nonlinear optical techniques are promising for investigating the chiral response of these material systems, and should be explored further.

Chapter 7

Conclusions and future work

The main objectives of this thesis were to test feasibility of using epioptic techniques to characterise plasmonic systems, secondly using the information obtained from epioptic techniques to model and understand the linear plasmonic response using an analytical model and finally using epioptic techniques to characterise ultra–thin chiral systems. The main linear technique used thoughout this thesis was RAS, and the main nonlinear technique used was SHG. With both techniques being surface and interface sensitive, they are ideal complementary techniques with which to study the material systems described above.

Epioptic tecniques like RAS are often used for monitoring and tuning the plasmonic response of small NP arrays on morphogically anisotropic templates. Growing these nanostructures in a controlled and reproducible fashion is key to their characterisation. Fabrication of plasmonic structures on nanopatterned substrates, like rippled Si, provides a stable surface upon which to grow and characterise NP arrays, and so the ability to monitor the evolution of the rippled Si templates by epioptic techniques was tested. Investigation of the effect of

the ripples in ambient condidtions with RAS showed that a broad maximum is introduced at aprroximately 2.5 eV, arising from strained a–Si, which in turn decreases in intensity with longer irradiation time and hence periodicty. When following the evolution of the ripples in UHV conditions, it was found that the first few hours of ripple formation are dominated by strain, along the ripple direction. SHG studies of the ripple formation was consistent with these finding, where there was found to be a huge enhancement of the SH response in the first 3 hours, which then decreased with increasing irradiation time. Further experiments would be useful at smaller time intervals to understand the evolution of the RAS and SHG signal with irradiation time. Finally samples with silver deposited within the valleys of the ripples were characterised using RAS and SHG. The RAS showed large anisotropic responses due to LSPRs, with the RAS signal increasing in intensity with increasing aspect ratio of the NPs, as expected. The SHG response agreed with this correlation and it was found that SHG was highly sensitive to the symmetry of the NP and morphology of the array. These results were compared to a similar system: Ag on facetted alumina, where similar results are shown. To the best of our knowledge these are among the first measurements of their kind, and it is worthwhile performing an in–depth study of thickness and NP shape dependent SHG measurements to fully understand the responses.

Modelling the linear optical response of ellipsoidal NPs is challenging since analytic solutions exist only for spheroids. An analytic model has been developed in Chapter 4, in order to model anisotropic ellipsoidal islands. Reasonable success has been shown in modelling the RAS response on various substrates and island densities, however, the model often falls short when modelling the pseudo–dielectric functions measured from SE, as this is a more stringent test of

the model since it includes x, y and z resonances. It highlights the complexity of trying to model plasmonic systems and perhaps a more extensive computational method is required. The transfer–matrix approach can be used for isolated NPs of arbitrary shape, although this can computationally expensive, however, with advances in computing power, these calculations may be a viable option.

As outlined in Chapter 1, SHG is ideal for studying chiral systems since they are asymmetric. SHG studies were performed on binol films in a transmission geometry, using these results a simple model was developed to fit the SH response, where the sign of the chiral parameter changed sign between enantiomers. The successful application of the model to binol films allowed monolayer chiral recognition. The model was extended to include an amlitude and phase factor for thin chiral films at reflecting surfaces, as the SH response will then be a coherent sum of the substrate and the chiral film. This approach was successful for thin films of cysteine on native–oxide–covered Si(001). The final test was to detect ultra–thin chiral films of cysteine deposited in UHV conditions on Au(110), monitored in real time using RAS. It was found that although SHG was sensitive to the deposition of the cysteine, the fitting of the data did not demonstrate conclusively a difference between (R)–(+)– and (S)–(−)–cysteine enantiomers, since the lineshape of the responses did not change very much, and underlining the difficulty in detecting enantiomeric excess in small chiral molecules. These results, although inconclusive, are strong justification for repeating the experiment on resonance, as this will surely amplify the nonlinear response.

References

[1] G. Chiarotti, G. Del Signore, and S. Nannarone. Optical detection of surface states on cleaved (111) surfaces of ge. *Phys. Rev. Lett.*, 21:1170–1172, Oct 1968.

[2] John F. McGilp. Optical characterisation of semiconductor surfaces and interfaces. *Progress in Surface Science*, 49(1):1 – 106, 1995.

[3] J.F. McGilp. Probing surface and interface structure using optics. *Journal of Physics: Condensed Matter*, 22(8), 2010.

[4] Bert Koopmans, Folkert van der Woude, and George A. Sawatzky. Surface symmetry resolution of nonlinear optical techniques. *Phys. Rev. B*, 46:12780–12783, Nov 1992.

[5] Y.-S. Lee and M.C. Downer. Reflected optical fourth harmonic generation at crystalline surfaces. *Thin Solid Films*, 364(12):80 – 85, 2000.

[6] Matthew M. Hawkeye and Michael J. Brett. Glancing angle deposition: Fabrication, properties, and applications of micro- and nanostructured thin films. *Journal of Vacuum Science & Technology A: Vacuum, Surfaces, and Films*, 25(5):1317–1335, 2007.

[7] J.F. McGilp. Optical response of low-dimensional in nanostructures grown by self-assembly on si surfaces. *physica status solidi (a)*, 188(4):1361–1369, 2001.

[8] D. E. Aspnes and A. A. Studna. Anisotropies in the above—band-gap optical spectra of cubic semiconductors. *Phys. Rev. Lett.*, 54(17):1956–1959, Apr 1985.

[9] V.L. Berkovits, I.V. Makarenko, T.A. Minashvili, and V.I. Safarov. Optical transitions on gaas [110] surface. *Solid State Communications*, 56(5):449 – 450, 1985.

[10] P Weightman, D S Martin, R J Cole, and T Farrell. Reflection anisotropy spectroscopy. *Reports on Progress in Physics*, 68(6):1251, 2005.

[11] D.E. Aspnes and A.A. Studna. Reflectance-difference spectroscopy of (110) gaas and inp. volume 5, pages 546 – 9, USA, 1987.

[12] D. E. Aspnes, J. P. Harbison, A. A. Studna, and L. T. Florez. Optical reflectance and electron diffraction studies of molecular-beam-epitaxy growth transients on gaas(001). *Phys. Rev. Lett.*, 59:1687–1690, Oct 1987.

[13] Z. Sobiesierski, D.I. Westwood, and C.C. Matthai. Aspects of reflectance anisotropy spectroscopy from semiconductor surfaces. *Journal of Physics: Condensed Matter*, 10(1):1 – 43, 1998.

[14] Robert Ehlert, Jinhee Kwon, Loucas Loumakos, Onise Sharia, Alexander A. Demkov, and M. C. Downer. Optical second-harmonic and reflectance-

anisotropy spectroscopy of clean and hydrogen-terminated vicinal si(001) surfaces. *J. Opt. Soc. Am. B*, 27(5):981–989, May 2010.

[15] Ph. Hofmann, K. C. Rose, V. Fernandez, A. M. Bradshaw, and W. Richter. Study of surface states on cu(110) using optical reflectance anisotropy. *Phys. Rev. Lett.*, 75:2039–2042, Sep 1995.

[16] Y. Borensztein, W. L. Mochan, J. Tarriba, R. G. Barrera, and A. Tadjeddine. Large anisotropy in the optical reflectance of ag(110) single crystals: Experiment and theory. *Phys. Rev. Lett.*, 71:2334–2337, Oct 1993.

[17] K. Stahrenberg, T. Herrmann, N. Esser, J. Sahm, W. Richter, S. V. Hoffmann, and Ph. Hofmann. Surface-state contribution to the optical anisotropy of ag(110) surfaces: A reflectance-anisotropy-spectroscopy and photoemission study. *Phys. Rev. B*, 58, Oct 1998.

[18] D.S. Martin, S.D. Barrett, and P. Weightman. Reflection anisotropy spectroscopy of clean and adsorbate-covered ni(110) surfaces. *Journal of Physics Condensed Matter*, 13(44):9847 – 9855, 2001.

[19] K. Fleischer, S. Chandola, N. Esser, W. Richter, and J.F. McGilp. Reflectance anisotropy spectroscopy of si(111)-(4×1)in. *physica status solidi (a)*, 188:1411–1416, 2001.

[20] J. Jacob, N. McAlinden, K. Fleischer, S. Chandola, and J. F. McGilp. Reflectance anisotropy studies of 52-au structures grown on si(111) surfaces with different step formations. *physica status solidi (c)*, 5(8):2569–2572, 2008.

[21] N. McAlinden and J.F. McGilp. Using surface and interface optics to probe the capping, with amorphous si, of au atom chains grown on vicinal si(111). *Journal of Physics: Condensed Matter*, 21(47), 2009.

[22] R. Verre, K. Fleischer, R.G.S. Sofin, N. McAlinden, J.F. McGilp, and I.V. Shvets. In situ characterization of one-dimensional plasmonic ag nanocluster arrays. *Physical Review B (Condensed Matter and Materials Physics)*, 83(12), 2011.

[23] P. A. Franken, A. E. Hill, C. W. Peters, and G. Weinreich. Generation of optical harmonics. *Phys. Rev. Lett.*, 7(4):118–119, Aug 1961.

[24] H. W. K. Tom, C. M. Mate, X. D. Zhu, J. E. Crowell, T. F. Heinz, G. A. Somorjai, and Y. R. Shen. Surface studies by optical second-harmonic generation: The adsorption of o_2, co, and sodium on the rh(111) surface. *Phys. Rev. Lett.*, 52:348–351, Jan 1984.

[25] H.W.K. Tom, T.F. Heinz, and Y.R. Shen. Second-harmonic reflection from silicon surfaces and its relation to structural symmetry. *Physical Review Letters*, 51(21):1983 – 6, 1983.

[26] T.F. Heinz, M.M.T. Loy, and W.A. Thompson. Study of si(111) surfaces by optical second-harmonic generation: reconstruction and surface phase transformation. *Physical Review Letters*, 54(1):63 – 6, 1985.

[27] T.F. Heinz, M.M.T. Loy, and W.A. Thompson. Study of symmetry and disordering of si(111)-77 surfaces by optical second harmonic generation. *Journal of Vacuum Science & Technology B (Microelectronics Processing and Phenomena)*, 3(5):1467 – 70, 1985.

[28] J.F. McGlip and Y. Yeh. Probing the buried metal-semiconductor interface by optical second harmonic generation: Au on si(1 1 1) and si(1 0 0). *Solid State Communications*, 59(2):91 – 94, 1986.

[29] H.M. van Driel. Second-harmonic generation from metal surfaces: beyond jellium. *Applied Physics A (Solids and Surfaces)*, A59(5):545 – 52, 1994.

[30] J.F. McGilp. Determining metal-semiconductor interface structure by optical second-harmonic generation. *Semiconductor Science and Technology*, 2(2):102 – 7, 1987/02/.

[31] J.D. O'Mahony, P.V. Kelly, and J.F. McGilp. Optical second harmonic generation from ordered si(111)-au interfaces. *Applied Surface Science*, (0):449 – 452, 1992.

[32] J.R. Power and J.F. McGilp. Resonance in the optical second harmonic response from the si(111)-sb interface. volume 287-288, pages 708 – 12, Netherlands, 1993.

[33] J. Jacob, A. Gomes Silva, K. Fleischer, and J.F. McGilp. Optical second-harmonic generation studies of si(111)- $\sqrt{3}\times\sqrt{3}$-ag and si(111)-3x1-ag grown on vicinal si(111). volume 5, pages 2649 – 2652, 2008.

[34] G. Lpke. Characterization of semiconductor interfaces by second-harmonic generation. *Surface Science Reports*, 35(34):75 – 161, 1999.

[35] Andrei Kirilyuk and Theo Rasing. Magnetization-induced-second-harmonic generation from surfaces and interfaces. *J. Opt. Soc. Am. B*, 22(1):148–167, Jan 2005.

[36] H.A. Wierenga, M.W.J. Prins, and Th. Rasing. Magnetization-induced optical second-harmonic generation from magnetic multilayers. *Physica B: Condensed Matter*, 204(14):281 – 286, 1995.

[37] L. Carroll, K. Fleischer, J.P. Cunniffe, and J.F. McGilp. Magnetic second-harmonic generation from the terraces and steps of aligned magnetic nanostructures grown on low symmetry interfaces. *Journal of Physics: Condensed Matter*, 20(26):265002 (8 pp.) –, 2008.

[38] H. Park, J. Qi, Y. Xu, K. Varga, S. M. Weiss, B. R. Rogers, G. Lupke, and N. Tolk. Characterization of boron charge traps at the interface of si/sio$_2$ using second harmonic generation. *Applied Physics Letters*, 95(6), 2009.

[39] J. Price, Y. Q. An, P. S. Lysaght, G. Bersuker, and M. C. Downer. Resonant photoionization of defects in si/sio[sub 2]/hfo[sub 2] film stacks observed by second-harmonic generation. *Applied Physics Letters*, 95(5):052906, 2009.

[40] A. Wokaun, J.G. Bergman, J.P. Heritage, A.M. Glass, P.F. Liao, and D.H. Olson. Surface second-harmonic generation from metal island films and microlithographic structures. *Physical Review B (Condensed Matter)*, 24(2), 1981.

[41] T. Petralli-Mallow, T.M. Wong, J.D. Byers, H.I. Yee, and J.M. Hicks. Circular dichroism spectroscopy at interfaces: a surface second harmonic generation study. *Journal of Physical Chemistry*, 97(7):1383 – 8, 1993.

[42] J.D. Byers, H.I. Yee, T. Petralli-Mallow, and J.M. Hicks. Second-harmonic generation circular-dichroism spectroscopy from chiral monolayers. *Physical Review B (Condensed Matter)*, 49(20):14643 – 7, 1994.

[43] Gustav Mie. Contributions to the optics of turbid media, particularly of colloidal metal solutions. *Ann. Phys*, 25:p.377, 1908.

[44] U. Kreibig and M. Vollmer. *Optical properties of metal clusters*. Number v. 25 in Springer series in materials science. Springer, 1995.

[45] Arnim Henglein and Michael Giersig. Formation of colloidal silver nanoparticles: capping action of citrate. *The Journal of Physical Chemistry B*, 103(44):9533–9539, 1999.

[46] Paul Mulvaney. Surface plasmon spectroscopy of nanosized metal particles. *Langmuir*, 12(3):788–800, 1996.

[47] Stephan Link and Mostafa A. El-Sayed. Size and temperature dependence of the plasmon absorption of colloidal gold nanoparticles. *The Journal of Physical Chemistry B*, 103(21), 1999.

[48] George H. Chan, Jing Zhao, Erin M. Hicks, George C. Schatz, and Richard P. Van Duyne. Plasmonic properties of copper nanoparticles fabricated by nanosphere lithography. *Nano Letters*, 7(7):1947–1952, 2007.

[49] N. McAlinden, J. J. Wang, and J. F. McGilp. Anisotropic optical response of elongated pb islands in the infrared spectral region. *physica status solidi (b)*, 249(6):1105–1109, 2012.

[50] Y. Ekinci, H. H. Solak, and J. F. Loffler. Plasmon resonances of aluminum nanoparticles and nanorods. *Journal of Applied Physics*, 104(8):083107, 2008.

[51] Stefan A. Maier, Pieter G. Kik, Harry A. Atwater, Sheffer Meltzer, Elad Harel, Bruce E. Koel, and Ari A.G. Requicha. Local detection of electromagnetic energy transport below the diffraction limit in metal nanoparticle plasmon waveguides. *Nat Mater*, 2(4):229–232, April 2003.

[52] Prashant K Jain, Xiaohua Huang, Ivan H El-Sayed, and Mostafa A El-Sayed. Review of some interesting surface plasmon resonance-enhanced properties of noble metal nanoparticles and their applications to biosystems. *Plasmonics*, 2(3):107–118, 2007.

[53] Harry A. Atwater and Albert Polman. Plasmonics for improved photovoltaic devices. *Nat Mater*, 9(3):205–213, March 2010.

[54] Jon A. Schuller, Edward S. Barnard, Wenshan Cai, Young Chul Jun, Justin S. White, and Mark L. Brongersma. Plasmonics for extreme light concentration and manipulation. *Nat Mater*, 9(3):193–204, March 2010.

[55] S.A. Maier and H.A. Atwater. Plasmonics: localization and guiding of electromagnetic energy in metal/dielectric structures. *Journal of Applied Physics*, 98(1):11101 – 1, 2005.

[56] Joel Henzie, Jeunghoon Lee, Min Hyung Lee, Warefta Hasan, and Teri W. Odom. Nanofabrication of plasmonic structures. *Annual Review of Physical Chemistry*, 60:147 – 165, 2009.

[57] Younan Xia and Naomi J. Halas. Shape-controlled synthesis and surface plasmonic properties of metallic nanostructures. *MRS Bulletin*, 30(5):338 – 343, 2005.

[58] Qingbo Zhang, Yen Tan, Jianping Xie, and Jim Lee. Colloidal synthesis of plasmonic metallic nanoparticles. *Plasmonics*, 4:9–22, 2009.

[59] U. Kreibig. Kramers kronig analysis of the optical properties of small silver particles. *Zeitschrift fr Physik A Hadrons and Nuclei*, 234:307–318, 1970. 10.1007/BF01394718.

[60] K. Lance Kelly, Eduardo Coronado, Lin Lin Zhao, and George C. Schatz. The optical properties of metal nanoparticles: the influence of size, shape, and dielectric environment. *The Journal of Physical Chemistry B*, 107(3):668–677, 2003.

[61] D. Bedeaux and J. Vliegar. *Optical properties ofsurfaces*. ICP, 2004.

[62] Kefeng Yu, K. Lance Kelly, Nobuyuki Sakai, and Tetsu Tatsuma. Morphologies and surface plasmon resonance properties of monodisperse bumpy gold nanoparticles. *Langmuir*, 24(11):5849–5854, 2008. PMID: 18435548.

[63] M Jalochowski, M Strzak, and R Zdyb. Reflectance anisotropy during growth of pb nanowires on well ordered si(3 3 5) surface. *Applied Surface Science*, 211(14):209 – 215, 2003.

[64] R. Verre, K. Fleischer, C. Smith, N. McAlinden, J. F. McGilp, and I. V. Shvets. Probing the out-of-plane optical response of plasmonic nanostructures using spectroscopic ellipsometry. *Phys. Rev. B*, 84:085440, Aug 2011.

[65] S. Camelio, D. Babonneau, D. Lantiat, and L. Simonot. Self-organized growth and optical properties of silver nanoparticle chains and stripes. *EPL (Europhysics Letters)*, 79(4):47002, 2007.

[66] Wai Lun Chan and Eric Chason. Making waves: Kinetic processes controlling surface evolution during low energy ion sputtering. *Journal of Applied Physics*, 101(12):121301, 2007.

[67] S. Camelio, D. Babonneau, D. Lantiat, L. Simonot, and F. Pailloux. Anisotropic optical properties of silver nanoparticle arrays on rippled dielectric surfaces produced by low-energy ion erosion. *Phys. Rev. B*, 80:155434, Oct 2009.

[68] Thomas Oates, Adrian Keller, Stefan Facsko, and Arndt Mcklich. Aligned silver nanoparticles on rippled silicon templates exhibiting anisotropic plasmon absorption. *Plasmonics*, 2:47–50, 2007. 10.1007/s11468-007-9025-z.

[69] Adrian Keller, Steven Robach, Stefan Facsko, and Wolfhard Mller. Simultaneous formation of two ripple modes on ion sputtered silicon. *Nanotechnology*, 19(13):135303, 2008.

[70] Adrian Keller and Stefan Facsko. Tuning the quality of nanoscale ripple patterns by sequential ion-beam sputtering. *Phys. Rev. B*, 82:155444, Oct 2010.

[71] N. Witkowski, Y. Borensztein, G. Baudot, V. Repain, Y. Girard, and S. Rousset. Combined scanning tunneling microscopy and reflectance anisotropy spectroscopy study of self-organized anisotropic cobalt nanodots on a vicinal au(111) surface. *Phys. Rev. B*, 70:085408, Aug 2004.

[72] J. M. Flores-Camacho, L. D. Sun, N. Saucedo-Zeni, G. Weidlinger, M. Hohage, and P. Zeppenfeld. Optical anisotropies of metal clusters supported on a birefringent substrate. *Phys. Rev. B*, 78:075416, Aug 2008.

[73] A. Otto, I. Mrozek, H. Grabhorn, and W. Akemann. Surface-enhanced raman scattering. *Journal of Physics: Condensed Matter*, 4(5):1143 – 212, 1992.

[74] Fielding Brown, Robert E. Parks, and Arthur M. Sleeper. Nonlinear optical reflection from a metallic boundary. *Phys. Rev. Lett.*, 14:1029–1031, Jun 1965.

[75] Sudhanshu S. Jha. Nonlinear optical reflection from a metal surface. *Phys. Rev. Lett.*, 15:412–414, Aug 1965.

[76] J.E. Sipe, V.C.Y. So, M. Fukui, and G.I. Stegeman. Second harmonic generation at metal surfaces. *Solid State Communications*, 34(7):523 – 526, 1980.

[77] Alessandro Belardini, Maria Cristina Larciprete, Marco Centini, Eugenio Fazio, Concita Sibilia, Mario Bertolotti, Andrea Toma, Daniele Chiappe, and Francesco Buatier De Mongeot. Tailored second harmonic generation from self-organized metal nano-wires arrays. *Optics Express*, 17(5):3603 – 3609, 2009.

[78] E.M. Kim, S.S. Elovikov, T.V. Murzina, A.A. Nikulin, O.A. Aktsipetrov, M.A. Bader, and G. Marowsky. Surface-enhanced optical third-harmonic generation in ag island films. *Physical Review Letters*, 95(22):227402 – 1, 2005.

[79] S. Houlton. Chirals continue to spiral. *Manufacturing Chemist*, 75(10):32 – 4, 2004.

[80] Vincent Humblot, Maria Ortega Lorenzo, Christopher J. Baddeley, Sam Haq, and Rasmita Raval. Local and global chirality at surfaces: succinic acid versus tartaric acid on cu(110). *Journal of the American Chemical Society*, 126(20):6460–6469, 2004. PMID: 15149243.

[81] Steven De Feyter, André Gesquière, Mohamed M. Abdel-Mottaleb, Petrus C. M. Grim, Frans C. De Schryver, Christian Meiners, Michel Sieffert, Suresh Valiyaveettil, and Klaus Müllen. Scanning tunneling microscopy: A unique tool in the study of chirality, dynamics, and reactivity in physisorbed organic monolayers. *Accounts of Chemical Research*, 33(8):520–531, 2000. PMID: 10955982.

[82] Hongbin Fang, L.C. Giancarlo, and G.W. Flynn. Direct determination of the chirality of organic molecules by scanning tunneling microscopy. *Journal of Physical Chemistry B*, 102(38):7311 – 15, 1998.

[83] Rachel McKendry, Maria-Elena Theoclitou, Trevor Rayment, and Chris Abell. Chiral discrimination by chemical force microscopy. *Nature*, 391(6667):566–568, February 1998.

[84] Angelika Kuhnle, Trolle R. Linderoth, Bjork Hammer, and Flemming Besenbacher. Chiral recognition in dimerization of adsorbed cysteine observed by scanning tunnelling microscopy. *Nature*, 415(6874):891–893, February 2002.

[85] Angelika Kuhnle, Trolle R. Linderoth, and Flemming Besenbacher. Enantiospecific adsorption of cysteine at chiral kink sites on au(110)-(12). *Journal of the American Chemical Society*, 128(4):1076–1077, 2006.

[86] T. P. Petralli-Mallow, A. L. Plant, M. L. Lewis, and J. M. Hicks. Cytochrome c at model membrane surfaces: exploration via second harmonic generation-circular dichroism and surface-enhanced resonance raman spectroscopy. *Langmuir*, 16(14):5960–5966, 2000.

[87] Marie-Claire Schanne-Klein, T. Boulesteix, F. Hache, M. Alexandre, G. Lemercier, and C. Andraud. Strong chiroptical effects in surface second harmonic generation obtained for molecules exhibiting excitonic coupling chirality. In *Nonlinear Optics: Materials, Fundamentals and Applications*, page ThC2. Optical Society of America, 2002.

[88] G. E. Isted, D. S. Martin, C. I. Smith, R. LeParc, R. J. Cole, and P. Weightman. The adsorption of l-cysteine on au(110) in ultra-high vacuum and electrochemical environments. *physica status solidi (c)*, 2(12):4012–4016, 2005.

[89] D. E. Aspnes, J. P. Harbison, A. A. Studna, and L. T. Florez. Application of reflectance difference spectroscopy to molecular-beam epitaxy growth of gaas and alas. *Journal of Vacuum Science & Technology A: Vacuum, Surfaces, and Films*, 6(3):1327–1332, 1988.

[90] J.R. Noonan and H.L. Davis. Leed analysis of the reconstructed au(110) surface. *Journal of Vacuum Science and Technology*, 16(2):587 – 9, 1979.

[91] D.S. Martin, R.J. Cole, N.P. Blanchard, G.E. Isted, D.S. Roseburgh, and P. Weightman. Contributions from surface-modified bulk electronic bands to the reflection anisotropy of au(110)-(1×2). *Journal of Physics: Condensed Matter*, 16:4375 – 84, 2004.

[92] B. Sheridan, D. S. Martin, J. R. Power, S. D. Barrett, C. I. Smith, C. A. Lucas, R. J. Nichols, and P. Weightman. Reflection anisotropy spectroscopy: A new probe for the solid-liquid interface. *Phys. Rev. Lett.*, 85:4618–4621, Nov 2000.

[93] R. Del Sole and G. Onida. Surface versus crystal-termination effects in the optical properties of surfaces. *Physical Review B (Condensed Matter)*, 60(8):5523 – 8, 1999.

[94] J. McIntyre and D. Aspnes. Differential reflection spectroscopy of very thin surface films. *Surface Science*, 24:417–434, 1971.

[95] K. Vedam. Spectroscopic ellipsometry: a historical overview. *Thin Solid Films*, 313-314(1-2):1 – 9, 1998.

[96] G. E. Jellison and Jr. Spectroscopic ellipsometry data analysis: measured versus calculated quantities. *Thin Solid Films*, 313-314:33 – 39, 1998.

[97] N.M. Bashara R.M.A. Azzam. *Ellipsometry and polarized light*. North Holland Publishing, 1977.

[98] Y.R. Shen. *The Principles of Nonlinear Optics*. Wiley, 1984.

[99] D. A. Kleinman. Nonlinear dielectric polarization in optical media. *Phys. Rev.*, 126:1977–1979, Jun 1962.

[100] P. Guyot-Sionnest and Y. R. Shen. Bulk contribution in surface second-harmonic generation. *Phys. Rev. B*, 38(12):7985–7989, Oct 1988.

[101] J. E. Sipe, D. J. Moss, and H. M. van Driel. Phenomenological theory of optical second- and third-harmonic generation from cubic centrosymmetric crystals. *Phys. Rev. B*, 35(3):1129–1141, Jan 1987.

[102] Victor Mizrahi and J. E. Sipe. Phenomenological treatment of surface second-harmonic generation. *J. Opt. Soc. Am. B*, 5(3):660–667, Mar 1988.

[103] T. G. Zhang, C. H. Zhang, and G. K. Wong. Determination of molecular orientation in molecular monolayers by second-harmonic generation. *J. Opt. Soc. Am. B*, 7(6):902–907, Jun 1990.

[104] M. C. Downer, B. S. Mendoza, and V. I. Gavrilenko. Optical second harmonic spectroscopy of semiconductor surfaces: advances in microscopic understanding. *Surface and Interface Analysis*, 31(10):966–986, 2001.

[105] J. R. Power, J. D. O'Mahony, S. Chandola, and J. F. McGilp. Resonant optical second harmonic generation at the steps of vicinal si(001). *Phys. Rev. Lett.*, 75:1138–1141, Aug 1995.

[106] J.D. Byers, H.I. Yee, and J.M. Hicks. Second harmonic generation analog of optical rotatory dispersion for the study of chiral monolayers. *Journal of Chemical Physics*, 101(7):6233 – 6241, 1994.

[107] Martti Kauranen, Jeffery J. Maki, Thierry Verbiest, Sven Van Elshocht, and André Persoons. Quantitative determination of electric and magnetic second-order susceptibility tensors of chiral surfaces. *Phys. Rev. B*, 55:R1985–R1988, Jan 1997.

[108] P. Drude. *Lehrbuch der Optik*. Leipzig, S. Hirzel, 1900.

[109] J.J. Maki, M. Kauranen, T. Verbiest, and A. Persoons. Uniqueness of wave-plate measurements in determining the tensor components of second-order surface nonlinearities. *Physical Review B (Condensed Matter)*, 55(8):5021 – 6, 1997.

[110] Jeffery J. Maki, Martti Kauranen, and André Persoons. Surface second-harmonic generation from chiral materials. *Phys. Rev. B*, 51:1425–1434, Jan 1995.

[111] M.C. Schanne-Klein, F. Hache, A. Roy, C. Flytzanis, and C. Payrastre. Off resonance second order optical activity of isotropic layers of chiral molecules: Observation of electric and magnetic contributions. *Journal of Chemical Physics*, 108(22):9436 – 43, 1998.

[112] M. Kauranen, T. Verbiest, J.J. Maki, and A. Persoons. Second harmonic generation from chiral surfaces. *Journal of Chemical Physics*, 101(9):8193 – 9, 1994.

[113] Andreas Biermanns, Ullrich Pietsch, Jörg Grenzer, Antje Hanisch, Stefan Facsko, Geradina Carbone, and Till Hartmut Metzger. X-ray scattering and diffraction from ion beam induced ripples in crystalline silicon. *Journal of Applied Physics*, 104(4):044312, 2008.

[114] Adrian Keller, Stefan Facsko, and Wolfhard Mller. Evolution of ion-induced ripple patterns on sio2 surfaces. *Nuclear Instruments and Methods in Physics Research Section B: Beam Interactions with Materials and Atoms*, 267(4):656 – 659, 2009.

[115] Albano Cossaro, Silvana Terreni, Ornella Cavalleri, Mirko Prato, Dean Cvetko, Alberto Morgante, Luca Floreano, and Maurizio Canepa. Electronic and geometric characterization of the l-cysteine paired-row phase on au(110). *Langmuir*, 22(26):11193 – 11198, 2006.

[116] Electronik-Manufaktur Mahlsdorf, Paul-Wegener-Str. 36, 12623 Berlin, Germany.

[117] Toshihiko Yokoyama, Takeshi Nakagawa, and Yasumasa Takagi. Magnetic circular dichroism for surface and thin film magnetism: Measurement techniques and surface chemical applications. *International Reviews in Physical Chemistry*, 27(3):449–505, 2008.

[118] Th. Herrmann, K. Lüdge, W. Richter, K. G. Georgarakis, P. Poulopoulos, R. Nünthel, J. Lindner, M. Wahl, and N. Esser. Optical anisotropy and magneto-optical properties of ni on preoxidized Cu(110). *Phys. Rev. B*, 73:134408, Apr 2006.

[119] J.F. McGilp, L. Carroll, K. Fleischer, J.P. Cunniffe, and S. Ryan. Magnetic second-harmonic generation from interfaces and nanostructures. *Journal of Magnetism and Magnetic Materials*, 322(912):1488 – 1493, 2010.

[120] K. Schmidegg, L.D. Sun, G.A. Maier, J. Keckes, and P. Zeppenfeld. Characterization of optical anisotropy in oriented poly(ethylene terephthalate) films using reflectance difference spectroscopy. *Polymer*, 47(13):4768 – 4772, 2006.

[121] N.C. Riach G.E Davis, L.E. MacDonald and R.E. Weber. *Handbook of*

Auger electron spectroscopy. Perkin Elmer Corporation, Physical Electronics Division., 1976.

[122] T. Yamaguchi, S. Yoshida, and A. Kinbara. Anomalous optical absorption of aggregated silver films. *Thin Solid Films*, 18(1):63 – 70, 1973.

[123] T. Yamaguchi, S. Yoshida, and A. Kinbara. Optical effect of the substrate on the anomalous absorption of aggregated silver films. *Thin Solid Films*, 21(1):173 – 187, 1974.

[124] Marcos M. Alvarez, Joseph T. Khoury, T. Gregory Schaaff, Marat N. Shafigullin, Igor Vezmar, and Robert L. Whetten. Optical absorption spectra of nanocrystal gold molecules. *The Journal of Physical Chemistry B*, 101(19):3706–3712, 1997.

[125] U. Kreibig and C. v. Fragstein. The limitation of electron mean free path in small silver particles. *Zeitschrift fr Physik A Hadrons and Nuclei*, 224:307–323, 1969. 10.1007/BF01393059.

[126] C. G. Granqvist and O. Hunderi. Optical properties of ultrafine gold particles. *Phys. Rev. B*, 16:3513–3534, Oct 1977.

[127] A. Pinchuk, U. Kreibig, and A. Hilger. Optical properties of metallic nanoparticles: influence of interface effects and interband transitions. *Surface Science*, 557(13):269 – 280, 2004.

[128] C. J. Flaten and E. A. Stern. Optical constants of some silver alloys. *Phys. Rev. B*, 11:638–650, Jan 1975.

[129] G. I. Lykken, A. L. Geiger, K. S. Dy, and E. N. Mitchell. Measurement of the superconducting energy gap and fermi velocity in single-crystal lead films by electron tunneling. *Phys. Rev. B*, 4:1523–1530, Sep 1971.

[130] M. Valamanesh, Y. Borensztein, C. Langlois, and E. Lacaze. Substrate effect on the plasmon resonance of supported flat silver nanoparticles. *The Journal of Physical Chemistry C*, 115(7):2914–2922, 2011.

[131] Alexander Moroz. Depolarization field of spheroidal particles. *J. Opt. Soc. Am. B*, 26(3):517–527, Mar 2009.

[132] M. Meier, A. Wokaun, and P. F. Liao. Enhanced fields on rough surfaces: dipolar interactions among particles of sizes exceeding the rayleigh limit. *J. Opt. Soc. Am. B*, 2(6):931–949, Jun 1985.

[133] Mathias Schubert. Polarization-dependent optical parameters of arbitrarily anisotropic homogeneous layered systems. *Phys. Rev. B*, 53:4265–4274, Feb 1996.

[134] M. Schubert, T.E. Tiwald, and J.A. Woollam. Explicit solutions for the optical properties of arbitrary magneto-optic materials in generalized ellipsometry. *Applied Optics*, 38(1):177 – 87, 1999.

[135] L. Persechini, M. Ranjan, F. Grossmann, S. Facsko, and J. F. McGilp. The linear and nonlinear optical response of native-oxide covered rippled si templates with nanoscale periodicity. *physica status solidi (b)*, 2012.

[136] D. Chaperot M. Navez and C. Sella. Microscopie electronique-etude de

lattique du verre par bombardment ionique. *C. R. Acad. Sci Paris*, 254, 1962.

[137] U. Valbusa, C. Boragno, and F. Buatier De Mongeot. Nanostructuring surfaces by ion sputtering. *Journal of Physics Condensed Matter*, 14(35):8153 – 8175, 2002.

[138] B. Ziberi, F. Frost, T. Hoche, and B. Rauschenbach. Ripple pattern formation on silicon surfaces by low-energy ion-beam erosion: experiment and theory. *Physical Review B (Condensed Matter and Materials Physics)*, 72(23):235310 – 1, 2005.

[139] S. Bhattacharjee, P. Karmakar, A.K. Sinha, and A. Charkrabarti. Ripple topography on thin zno films by grazing and oblique incidence ion sputtering. *Applied Surface Science*, 257(15):6775 – 6778, 2011.

[140] Hua Zhou, Yiping Wang, Lan Zhou, Randall L. Headrick, Ahmet S. Özcan, Yiyi Wang, Gözde Özaydin, Karl F. Ludwig, and D. Peter Siddons. Wavelength tunability of ion-bombardment-induced ripples on sapphire. *Phys. Rev. B*, 75:155416, Apr 2007.

[141] S. Grigorian, U. Pietsch, J. Grenzer, D. P. Datta, T. K. Chini, S. Hazra, and M. K. Sanyal. Microstructural anisotropy at the ion-induced rippled amorphous-crystalline interface of silicon. *Applied Physics Letters*, 89(23):231915, 2006.

[142] Adrian Keller, Rodolfo Cuerno, Stefan Facsko, and Wolfhard Möller. Anisotropic scaling of ripple morphologies on high-fluence sputtered silicon. *Phys. Rev. B*, 79:115437, Mar 2009.

[143] D. Papadimitriou and W. Richter. Highly sensitive strain detection in silicon by reflectance anisotropy spectroscopy. *Phys. Rev. B*, 72:075212, Aug 2005.

[144] T. F. Heinz, M. M. T. Loy, and W. A. Thompson. Study of symmetry and disordering of si(111)-7 x 7 surfaces by optical second harmonic generation. *Journal of Vacuum Science & Technology B: Microelectronics and Nanometer Structures*, 3(5):1467–1470, 1985.

[145] C. H. Bjorkman, Jr. C. E. Shearon, Y. Ma, T. Yasuda, G. Lucovsky, U. Emmerichs, C. Meyer, K. Leo, and H. Kurz. Second-harmonic generation in si–sio[sub 2] heterostructures formed by chemical, thermal, and plasma-assisted oxidation and deposition processes. volume 11, pages 964–970. AVS, 1993.

[146] D. Lim, M. C. Downer, J. G. Ekerdt, N. Arzate, Bernardo S. Mendoza, V. I. Gavrilenko, and R. Q. Wu. Optical second harmonic spectroscopy of boron-reconstructed si(001). *Phys. Rev. Lett.*, 84:3406–3409, Apr 2000.

[147] Mukesh Ranjan, Thomas W. H. Oates, Stefan Facsko, and Wolfhard Mller. Optical properties of silver nanowire arrays with 35 nm periodicity. *Opt. Lett.*, 35(15):2576–2578, Aug 2010.

[148] T.W.H. Oates. Aligned metallic nanoparticles on rippled surfaces: Optical characterization using generalized ellipsometry. *Applied Surface Science*, 258(23):9278 – 9282, 2012.

[149] M.I. Stockman, D.J. Bergman, C. Anceau, S. Brasselet, and J. Zyss. Enhanced second-harmonic generation by metal surfaces

with nanoscale roughness: nanoscale dephasing, depolarization, and correlations. *Physical Review Letters*, 92(5):057402 – 1, 2004. enhanced second-harmonic generation;metal surfaces;nanoscale roughness;nanoscale dephasing;depolarization;correlations;spectral-expansion Green's function theory;topography;polarization;spatial-coherence properties;second-harmonic local fields;rough metal surfaces;spatial distributions;fundamental frequency;spatial decay;metal fill factors;hyper-Rayleigh scattering;nanometer-scale nonlinear-optical illumination;.

[150] L. Persechini and J. F. McGilp. Chiral second-harmonic generation from small organic molecules at surfaces. *physica status solidi (b)*, 2012.

[151] Jeffrey D. Byers and Janice M. Hicks. Electronic spectral effects on chiral surface second harmonic generation. *Chemical Physics Letters*, 231(23):216 – 224, 1994.

[152] Janice M. Hicks, Teresa Petralli-Mallow, and Jeffrey D. Byers. Consequences of chirality in second-order non-linear spectroscopy at surfaces. *Faraday Discuss.*, 99:341–357, 1994.

[153] Xiaoqin Li, J. Willits, S. T. Cundiff, I. M. P. Aarts, A. A E. Stevens, and D. S. Dessau. Circular dichroism in second harmonic generation from oxidized si (001). *Applied Physics Letters*, 89(2):022102, 2006.

[154] E. Ataman, C. Isvoranu, J. Knudsen, K. Schulte, J.N. Andersen, and J. Schnadt. Adsorption of l-cysteine on rutile tio2(110). *Surface Science*, 605(1-2):179 – 86, 2011.

[155] D. S. Martin, G. E. Isted, R. J. Cole, and P. Weightman. Investigating the adsorption of the amino acid l-cysteine onto ag(110). *physica status solidi (c)*, 2(12):4043–4047, 2005.

[156] Qing-Min Xu, Li-Jun Wan, Chen Wang, Chun-Li Bai, Zheng-Yu Wang, and T. Nozawa. New structure of l-cysteine self-assembled monolayer on au(111): studies by *in situ* scanning tunneling microscopy. *Langmuir*, 17(20):6203 – 6, 2001.

[157] Angelika Kuhnle, Trolle R. Linderoth, Michael Schunack, and Flemming Besenbacher. L-cysteine adsorption structures on au(111) investigated by scanning tunneling microscopy under ultrahigh vacuum conditions. *Langmuir*, 22(5):2156 – 2160, 2006.

[158] Grazia Gonella, Silvana Terreni, Dean Cvetko, Albano Cossaro, Lorenzo Mattera, Ornella Cavalleri, Ranieri Rolandi, Alberto Morgante, Luca Floreano, and Maurizio Canepa. Ultrahigh vacuum deposition of l-cysteine on au(110) studied by high-resolution x-ray photoemission: from early stages of adsorption to molecular organization. *The Journal of Physical Chemistry B*, 109:18003–18009, 2005.

[159] M. Canepa, L. Lavagnino, L. Pasquali, R. Moroni, F. Bisio, V. De Renzi, S. Terreni, and L. Mattera. Growth dynamics of l-cysteine sams on single-crystal gold surfaces: A metastable deexcitation spectroscopy study. *Journal of Physics Condensed Matter*, 21(26), 2009.

[160] A. Kuhnle, L.M. Molina, T.R. Linderoth, B. Hammer, and F. Besenbacher. Growth of unidirectional molecular rows of cysteine on au(110)-(12) driven

by adsorbate-induced surface rearrangements. *Physical Review Letters*, 93(8), 2004.

[161] Angelika Khnle. Self-assembly of organic molecules at metal surfaces. *Current Opinion in Colloid & Interface Science*, 14(2):157 – 168, 2009.

[162] K. Stahrenberg, Th. Herrmann, N. Esser, W. Richter, S. V. Hoffmann, and Ph. Hofmann. Optical properties of the au(110) surface. *Phys. Rev. B*, 65:035407, Dec 2001.

[163] J.-K. Hansen, J. Bremer, L. Seime, and O. Hunderi. Local-field effects and electronic anisotropy of the (1×2) reconstructed au(1 1 0) surface. *Physica A: Statistical Mechanics and its Applications*, 298(12):46 – 55, 2001.

[164] Ahmad Ahmadi, Gary Attard, Juan Feliu, and Antonio Rodes. Surface reactivity at "chiral" platinum surfaces. *Langmuir*, 15(7):2420–2424, 1999.

[165] Taihua Li, Hyun Gyu Park, Hee-Seung Lee, and Seong-Ho Choi. Circular dichroism study of chiral biomolecules conjugated with silver nanoparticles. volume 15, pages S660 – S663, 2004.